Synergistic Computational and Microstructural Design of Next-Generation High-Temperature Austenitic Stainless Steels

Final Technical Report

For the Period:
August 1, 2012 to July 31, 2015

Principal Authors' Names
Ibrahim Karaman and Raymundo Arroyave

Report Issue Date: November 04th, 2015

DOE Award Number: DE-FE0008719

Name and Address of the Submitting Institution:
Texas A&M Engineering Experiment Station
1470 William D. Fitch Parkway
College Station, TX 77845-4645

DISCLAIMER

ABSTRACT

The purpose of this project was to: 1) study deformation twinning, its evolution, thermal stability, and the contribution on mechanical response of the new advanced stainless steels, especially at elevated temperatures; 2) study alumina-scale formation on the surface, as an alternative for conventional chromium oxide, that shows better oxidation resistance, through alloy design; and 3) design new generation of high temperature stainless steels that form alumina scale and have thermally stable nano-twins.

The work involved few baseline alloys for investigating the twin formation under tensile loading, thermal stability of these twins, and the role of deformation twins on the mechanical response of the alloys. These baseline alloys included Hadfield Steel (Fe-13Mn-1C), 316, 316L and 316N stainless steels. Another baseline alloy was studied for alumina-scale formation investigations. Hadfield steel showed twinning but undesired second phases formed at higher temperatures. 316N stainless steel did not show signs of deformation twinning. Conventional 316 stainless steel demonstrated extensive deformation twinning at room temperature. Investigations on this alloy, both in single crystalline and polycrystalline forms, showed that deformation twins evolve in a hierarchical manner, consisting of micron–sized bundles of nano-twins. The width of nano-twins stays almost constant as the extent of strain increases, but the width and number of the bundles increase with increasing strain. A systematic thermo-mechanical cycling study showed that the twins were stable at temperatures as high as 900°C, after the dislocations are annealed out. Using such cycles, volume fraction of the thermally stable deformation twins were increased up to 40% in 316 stainless steel.

Using computational thermodynamics and kinetics calculations, we designed two generations of advanced austenitic stainless steels. In the first generation, Alloy 1, which had been proposed as an alumina-forming austenitic stainless steel, is fully austenitic, but possesses carbides that were not dissolvable and could not be controlled. This alloy also did not show deformation twinning. Alloy 2 was designed based on alloy 1, but was not fully austenitic and had significant traces of uncontrollable precipitates as well. Alloy 3, also designed based on alloy 1, was mainly austenitic with evolution of a second phase along the grain boundaries, but also had precipitates that were not controllable.

Based on the knowledge gained from the first generation of the designed steels, two more steels, called PGAA1 and PGAA2, were proposed using genetic algorithms that, based on the modelling, were supposed to exhibit alumina-scale formation. PGAA1, however, did not demonstrate a fully austenitic structure. PGAA2 could achieve a mostly austenitic structure through thermo-mechanical processing, and was then used for oxidation tests. The oxidation tests of PGAA2, with and without nitrogen impurities, along with alloy 1, suggested that PGAA2 can form alumina-scale similar to alloy 1, but N impurity will prevent formation of such a scale, probably through formation of aluminum nitrides.

For the above mentioned genetic algorithm framework of alloy design, separate models were developed for specific design criteria. For prediction of alumina formation in stainless steels, a model was constructed based off of two criteria – effective valence and third element effect. These criteria capture the thermodynamics and kinetics of alumina formation in steels. To test the efficacy and robustness of this model, they were tested against alloys in the literature which had been experimentally verified to exhibit alumina formation and the predictions were in excellent agreement with the experiments. Another meta-model for prediction of twinning in unknown steel compositions was developed by an informatics based machine learning/data mining approach. Stacking Fault Energy data was captured from the literature for a large number of steel compositions and then this data was used to build a classifier to predict deformation mechanisms. Here a training set-test set based analysis was performed to test performance. The above genetic algorithm based optimization framework for alloy design was exhibited to be a successful methodology for accelerated materials discovery in the context of alloy design.

Table of Contents

I. Executive Summary

The purpose of this project was to: 1) study deformation twinning, its evolution, thermal stability, and the contribution on mechanical response of the new advanced stainless steels, especially at elevated temperatures; 2) study alumina-scale formation on the surface, as an alternative for conventional chromium oxide, that shows better oxidation resistance, through alloy design; and 3) design new generation of high temperature stainless steels that form alumina scale and have thermally stable nano-twins.

The work involved few baseline alloys for investigating the twin formation under tensile loading, thermal stability of these twins, and the role of deformation twins on the mechanical response of the alloys. These baseline alloys included Hadfield Steel (Fe-13Mn-1C), 316, 316L and 316N stainless steels (Figure 1). Another baseline alloy was studied for alumina-scale formation investigations. Hadfield steel showed twinning but undesired second phases formed at higher temperatures. 316N stainless steel did not show signs of deformation twinning. Conventional 316 stainless steel demonstrated extensive deformation twinning at room temperature. Investigations on this alloy, both in single crystalline and polycrystalline forms, showed that deformation twins evolve in a hierarchical manner, consisting of micron–sized bundles of nano-twins. The width of nano-twins stays almost constant as the extent of strain increases, but the width and number of the bundles increase with increasing strain. A systematic thermo-mechanical cycling study showed that the twins were stable at temperatures as high as 900°C, after the dislocations are annealed out. Using such cycles, volume fraction of the thermally stable deformation twins were increased up to 40% in 316 stainless steel.

Hadfield Steel	✓	Highly twinned {001}/{111} texture
	×	Evolution of second phase at high temperatures
316N SS	✓	Fully austenite
	×	No twinning
316 SS	✓	Fully austenite
	✓	Twinning
	×	No alumina scale formation

Figure 1- Baseline alloys studied for deformation twinning

Using computational thermodynamics and kinetics calculations, we designed two generations of advanced austenitic stainless steels. In the first generation (Figure 2), Alloy 1, which had been proposed as an alumina-forming austenitic stainless steel, is fully austenitic, but possesses carbides

that were not dissolvable and could not be controlled. This alloy also did not show deformation twinning. Alloy 2 was designed based on alloy 1, but was not fully austenitic and had significant traces of uncontrollable precipitates as well. Alloy 3, also designed based on alloy 1, was mainly austenitic with evolution of a second phase along the grain boundaries, but also had precipitates that were not controllable.

Alloy 1	✓	Fully austenite
	×	Uncontrollable NbC precipitation
	×	No Twinning (by our own exp.)
	✓	Alumina scale formation
Alloy 2	×	Second phase formation
	×	Uncontrollable Ti-rich NbC precipitation
Alloy 3	✓	Austenite with intra-granular second phase
	×	Uncontrollable Ti-Nb carbo-nitrides and AlN precipitation

Figure 2- Customized alloys studied for alumina-scale formation investigations

Based on the knowledge gained from the first generation of the designed steels, two more steels, called PGAA1 and PGAA2, were proposed using genetic algorithms that, based on the modelling, were supposed to exhibit alumina-scale formation. PGAA1, however, did not demonstrate a fully austenitic structure. PGAA2 could achieve a mostly austenitic structure through thermo-mechanical processing, and was then used for oxidation tests. The oxidation tests of PGAA2, with and without nitrogen impurities, along with alloy 1, suggested that PGAA2 can form alumina-scale similar to alloy 1, but N impurity will prevent formation of such a scale, probably through formation of aluminum nitrides.

For the above mentioned genetic algorithm framework of alloy design, separate models were developed for specific design criteria. For prediction of alumina formation in stainless steels, a model was constructed based off of two criteria – effective valence and third element effect. These criteria capture the thermodynamics and kinetics of alumina formation in steels. To test the efficacy and robustness of this model, they were tested against alloys in the literature which had been experimentally verified to exhibit alumina formation and the predictions were in excellent agreement with the experiments. Another meta-model for prediction of twinning in unknown steel compositions was developed by an informatics based machine learning/data mining approach. Stacking Fault Energy data was captured from the literature for a large number of steel compositions and then this data was used to build a classifier to predict deformation mechanisms.

Here a training set-test set based analysis was performed to test performance. The above genetic algorithm based optimization framework for alloy design was exhibited to be a successful methodology for accelerated materials discovery in the context of alloy design.

II. Experimental Methods

All microscopy was performed on samples that were polished mechanically down to 0.06μm colloidal silica. Tensile samples were all flat dog-bone 8 mm x 3mm x 1mm specimen. Samples were cut using wire electron discharge (EDM) machine. Uniaxial tensile tests were performed using an MTS tension set-up. Electron Microscopy was performed using a FEI QUANTA-600 FESEM microscope and a JEOL 1200 EX TEM. The etchant used was a customized etchant consisting of 10 v% HCl, 30 v% HNO_3, and 30v% H_2O. Optical Microscopy was done with a Keyence microscope. Single crystals were fabricated along three different crystallographic orientations in collaboration with Prof. Chumlyakov from Siberian Physical Technical Institute, Russia. Single crystals are grown using the Bridgman technique in He atmosphere.

We characterized the microstructural and mechanical properties of single crystalline Hadfield steels along the [111] orientation (i.e. Fe-13Mn-1.1C in wt.%). The purpose of the study was to understand high temperature stability of deformation twinning, which has been stated in the proposal as part of the scientific merit of the project. Further microstructural investigation has been performed on these deformed samples using EBSD at room temperature. The samples were electro-polished using 10% perchloric acid before the examination. Samples were then heat treated at 500°C and 600°C for 1 hour followed by water quenching.

The chemical compositions of the polycrystalline baseline materials have been determined. The compositions are summarized in Table 1. Alloy 1 was first proposed by Yamamoto et al. from Oak Ridge National Lab which showed promising high temperature creep and corrosion resistance and is an ideal baseline composition. We first performed a detailed microstructural and mechanical characterization on this composition for two reasons. Firstly, the characterized mechanical performance was utilized as the baseline behavior for the future comparison. Secondly, no report had been published on the twining ability of this composition up to that date. Since our proposed microstructure design approach requires ultrafine twinning at high temperature pinned by the nano-precipitates, it was essential to know whether deformation twinning could be obtained for this material. Moreover, even if the material (Alloy 1) did not show deformation twinning, the obtained mechanical performance (strength, ductility, and creep) was to be utilized to compare with those of our designed alloy in the future. Alloy 2 and 3 were designed to increase the probability of obtaining deformation twining. The replacement of Ni by Mn was expected to decrease the stacking fault energy of the alloy. Nitrogen contained 316 stainless steels have been reported to improve the twinning ability and thus, nitrogen was added to both alloy 2 and 3. Cr and Al are effective to resist corrosion. The addition of Nb, Ti, Mo, and V is to form nano-size carbides (e.g. NbC, TiC, MoC and VC). The difference between alloy 2 and 3 is the Ni content. Since Ni is austenite stabilizer, the two different Ni contents is designed to guarantee that fully austenitic microstructure could be obtained.

Based on thermodynamic calculations presented in the previous reports and Genetic Algorithm based alloy design presented above, as well as the previous experimental results, four alloy compositions were chosen as the next generation alumina forming austenitic stainless steels (Table 2). PGAA1 is an alloy which, based on the thermodynamic calculations, is very close to the "alumina-forming" threshold. This alloy is going to validate the accuracy of this alumina forming threshold. PGAA2 is an alloy which has been provided by generic algorithm to be a fully austenitic alumina forming steel. PGAA2-2 has a slightly more aluminum content than PGAA2 does, in order to study its effect on alumina-forming and its structure. Alloy4 is selected purely based on experience, and has a composition between 316 stainless steel (which shows deformation twins and no alumina), and our previously reported Alloy1 (which forms alumina but no deformation twinning). Chemical compositions of these alloys are presented in Table 2. The alloys were were cast as ingots with an outer diameter of 1 inch and a length of 6 inches. Next we will try to characterize the new alloys and process them accordingly. In order to homogenize the bars of these materials we attempted to use Equal Channel Angular Extrusion (ECAE) at high temperatures. The extrusion die has a square cross-section, 1inch x 1inch. So the samples were milled to create two sets of parallel surfaces, each less than 0.95 inches apart, and were covered in liquid glass which acts as lubricant for extrusions at high temperatures. The die was heated to 300°C and kept at this temperature during extrusion.

Table 1- Proposed chemical compositions of the baseline polycrystalline materials.

in wt%	**Fe**	**Ni**	**Cr**	**Mn**	**Nb**	**Si**	**Al**	**Ti**	**Mo**	**V**	**C**	**N**	**B**
Alloy 1	Ba.	20	14	2	0.86	0.15	2.5		2.5		0.08		0.01
Alloy 2	Ba.	12	14	10	1	0.2	2.5	0.3	2.5	0.5	0.08	0.01	
Alloy 3	Ba.	17	14	10	1	0.2	2.5	0.3	2.5	0.5	0.08	0.01	

Table 2- Nominal chemical compositions of selected next-generation Alumina forming Austenitic Stainless Steels

wt.%	**C**	**Mn**	**Ni**	**Mo**	**Al**	**Cr**	**Si**	**Fe**
PGAA1	0.073	3.9	11	2.03	3	19.8	0.38	bal.
PGAA2	0.088	9	17.15	2.24	3.11	15.3	0.19	bal.
Alloy 4	0.05	10	10	2.5	3	16	0.5	bal.
PGAA2-2	0.088	9	17.15	2.24	4.11	15.3	0.19	bal.

III. Results and Discussion

1. Computational Efforts

The computational efforts on this project can be summarized under following important heads.

a) Simulation and Prediction of Alumina Formation

a-1) Effective valence

The oxidation rate constant is significant to determine the passivating behavior of stainless steel. From the following chemical reaction:

$$\left(\frac{2x}{y}\right)M + O_2 \rightarrow \left(\frac{2}{y}\right)M_xO_y$$

The parabolic oxidation constant can be estimated as:

$$k_t = Val^{eff} \cdot \Delta G_f$$

where, Val^{eff} stands the total effective valence of the oxide; ΔG_f represents the required driving force for forming the oxide. In this work, Val^{eff} can be calculated according to the chemical composition:

$$Val^{eff} = \sum_{n=i}(z_i - z_f)C_i$$

z_i and z_f are the effective valence of the ions of element i and oxide. C_i is the atomic fraction of the element i.

ΔG_f can be calculated by:

$$\Delta G_f = \Delta G_0 + RTln\left(\frac{a_{M_xO_y}^{2/y}}{a_M^{2/y} \cdot P_{O_2}}\right)$$

ΔG_0 is the standard free energy of the formation; R stands the gas constant; T is the temperature (K). $a_{M_xO_y}$ and a_M are the activities of oxidized element which is commonly taken as 1 and the element M. P_{O_2} stands the partial pressure of oxygen which is about 0.2. In this work, 0.1 wt% of Al is added to replace Fe in 316 LN to examine the formation of Al_2O_3. The activity of Al is calculated using Thermo-Calc with TCFE6 V6.2 database.

The predicted oxidation constant is presented as Figure 3. It can be understood that the oxidation is faster with higher k_t. This condition is also necessary for the formation of a stable passivating oxide layer. This result was used as the reference for material selection in the following research, especially in optimization process.

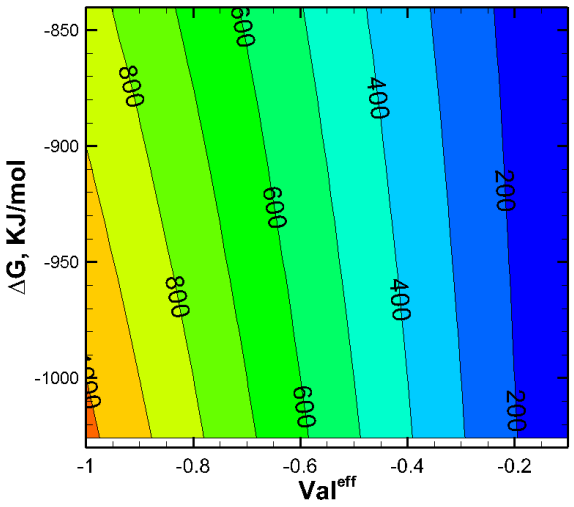

Figure 3- The predicted oxidation constant (k_t) of Al2O3 as function of $[\![Val]\!]^{eff}$ *and* $[\![\Delta G]\!]^{f}$.

Based on above alumina formation trends could be seen through the use of a contour graph such as the one seen in Figure 4, where stable alumina tends to have a higher likelihood of formation, the higher the k value is, or, in other words, the lower the free energy and effective valence are.

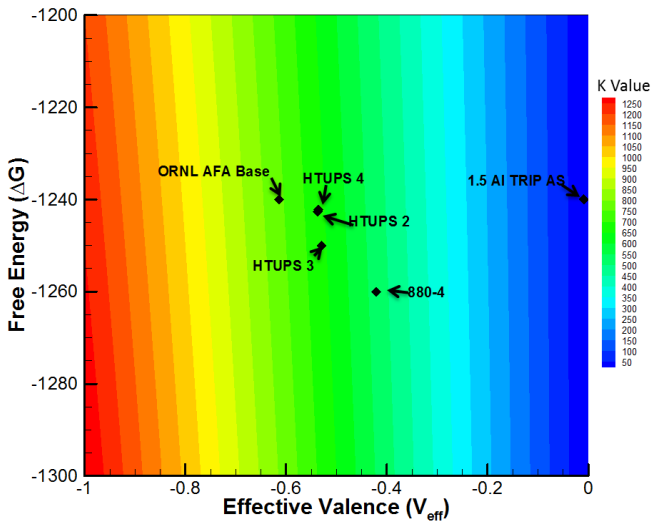

Figure 4- Free energy with respect to effective valence for each alloy at 1000K

Using the trend seen in Figure 4, it then becomes necessary to understand the role that each individual element plays within the contour map. To observe and understand individual element trends for an alloy, our original baseline alloy (Alloy 1, Fe-20Ni-14Cr-2Mn-0.86Nb-0.15Si-2.5Al-2.5Mo) had each element changed at a time. The change for each element was determined by 10% of its weight percent. It should be noted that the axis of the contour map has been changed to

magnify the changes for each element. In Figure 5, it can be seen that the elements that play the most important role in increasing or decreasing the k value are chromium and nickel.

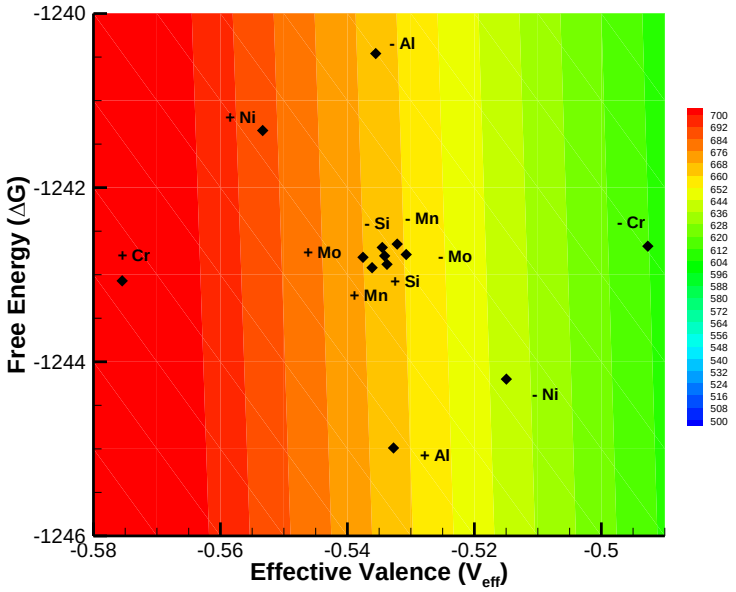

Figure 5- Effect of each Element in Alloy 1 on the Free Energy and Effective Valence

a-2) Third Element Effect

Another phenomenon that should be taken into account when determining the oxidation trend of alumina scales is the third element effect. The third element effect essentially emphasizes the amount of an additional element needed in the composition to ensure a stable growth of the primary oxidation element; in this particular case, chromium is the third element while aluminum is the primary oxidation element. Figure 6 shows a graphical example of the equation necessary to predict the third element trend. In Figure 7, multiple alloys and kinetic parameters are placed into the model to observe which types of trends are to be expected for different environments and compositions. Using the third element equation and graphical model it should be possible to determine the trend for internal and external oxidation of the different alloys

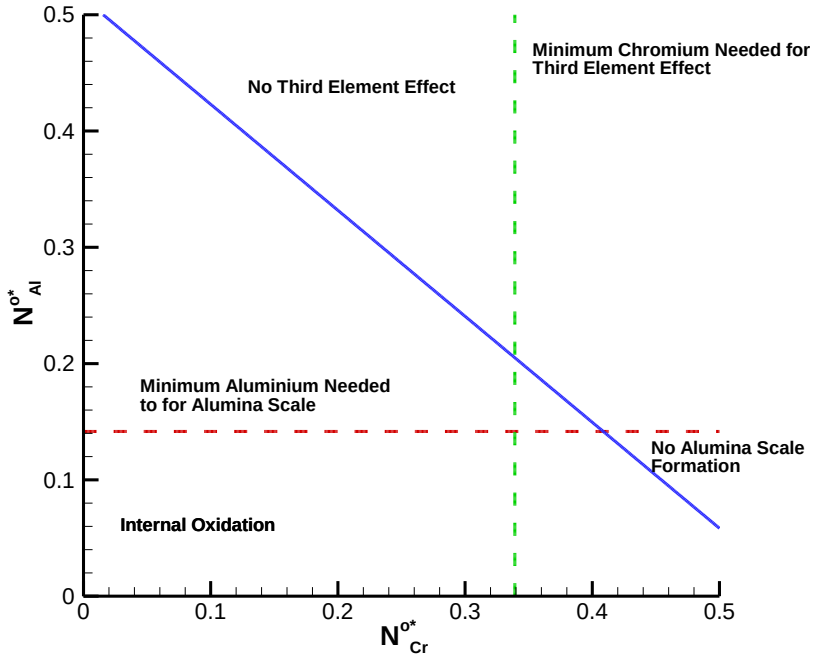

Figure 6- Third element effect explanation

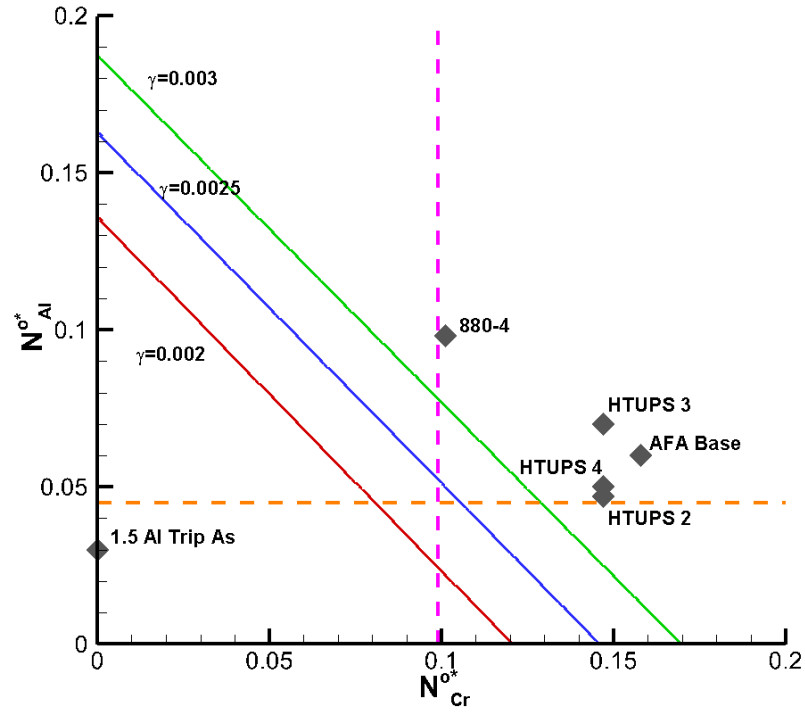

Figure 7- Third element effect with alloys and multiple kinetic parameters

b) Testing of Alumina Formation Criteria of Experimental Alloys

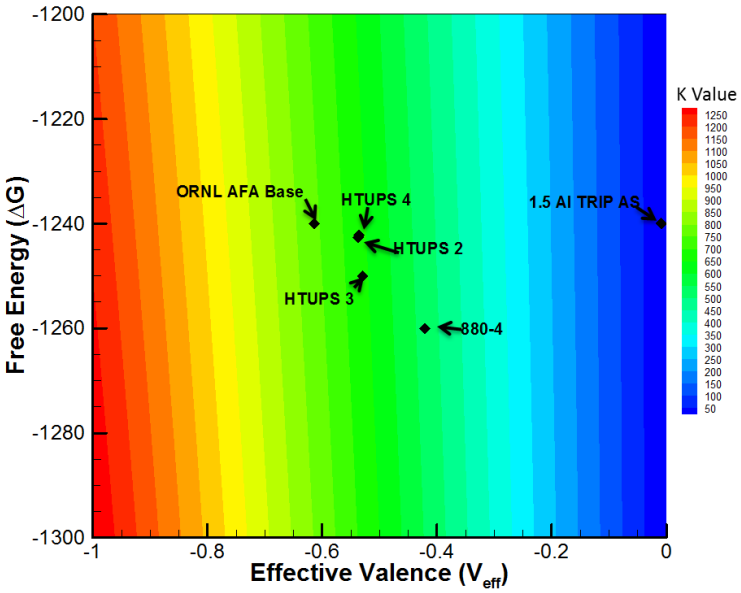

Figure 8- Free Energy with respect to Effective Valence for Each Alloy at 1000K

A major push on the present collaboration is the development of consistent, physics-based criteria to predict the ability of an arbitrary alloy composition to form stable alumina protective layer. Above we discussed the use of criteria based on the thermodynamic driving force for the formation of alumina as well as the expected kinetic constant for alumina growth when exposed to oxidizing atmospheres. In Figure 8, we can see that the metric selected for the analysis of the existing alumina-forming alloys investigated in the literature seems to be effective in screening compositions that are likely to form alumina layers and thus offer superior resistance to oxidizing atmospheres that are predominant in power generation environments.

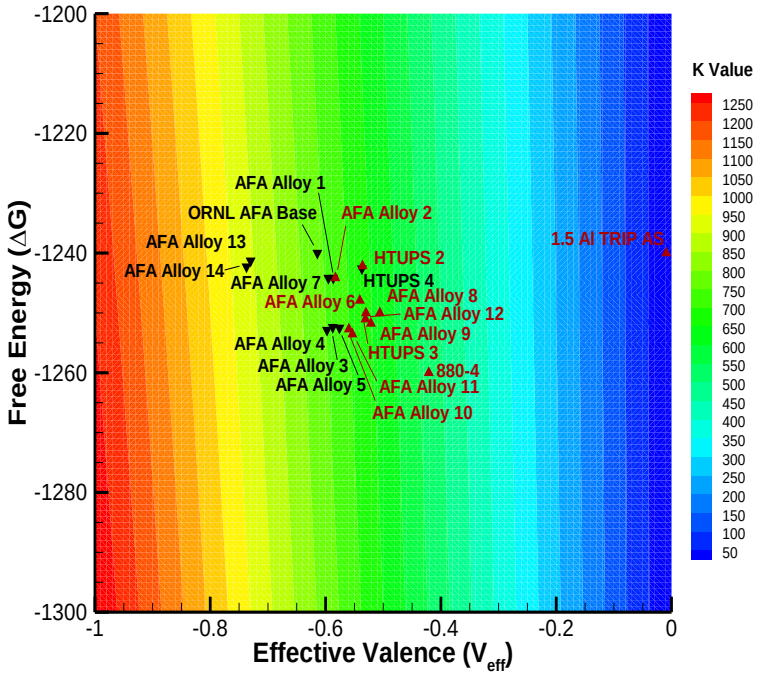

Figure 9- Effective Valence Contour Graph

To further our investigation on stable alumina prediction through the relationship between the thermodynamic and kinetic properties of alumina formation, additional experimental alloys were used to verify the initially developed criteria. With the non-alumina forming alloys color coded in red and stable alumina forming alloys in black, the results seen in Figure 9 clearly shows a visible trend of good alumina formation when the right combination between the driving force for alumina formation and the availability of elements to form oxides (represented in terms of thermodynamic driving force and effective balance) are combined in order to calculate an effective kinetic factor, K. From our investigations, it seems that alumina formation is correlated with values for this K parameter in excess of 750 as we can see a clear demarcation between alumina-forming and non-alumina forming compositions at around this value.

Previously we also discussed the importance of the so-called third-element effect. This phenomenon is associated with the synergistic interactions between more than one oxide forming alloying element whereby the initial formation of an oxide layer impedes the diffusion of oxygen into the material---preventing internal oxidation---while facilitating the diffusion of a second oxide former (in this case Al) that can then form a stable passive layer against further oxidation. The so-

called third element effect can be summarized in Figure 10. In this plot, the x axis corresponds to the effective Cr composition of the alloy while the y axis corresponds to the aluminum content. The horizontal and vertical dashed lines corresponds to the minimum amount of Al and Cr, respectively, necessary to have a positive thermodynamic driving force for the formation of a stable alumina or chromia layer. Anything below these limits leads to internal oxidation, depicted in the diagram in red.

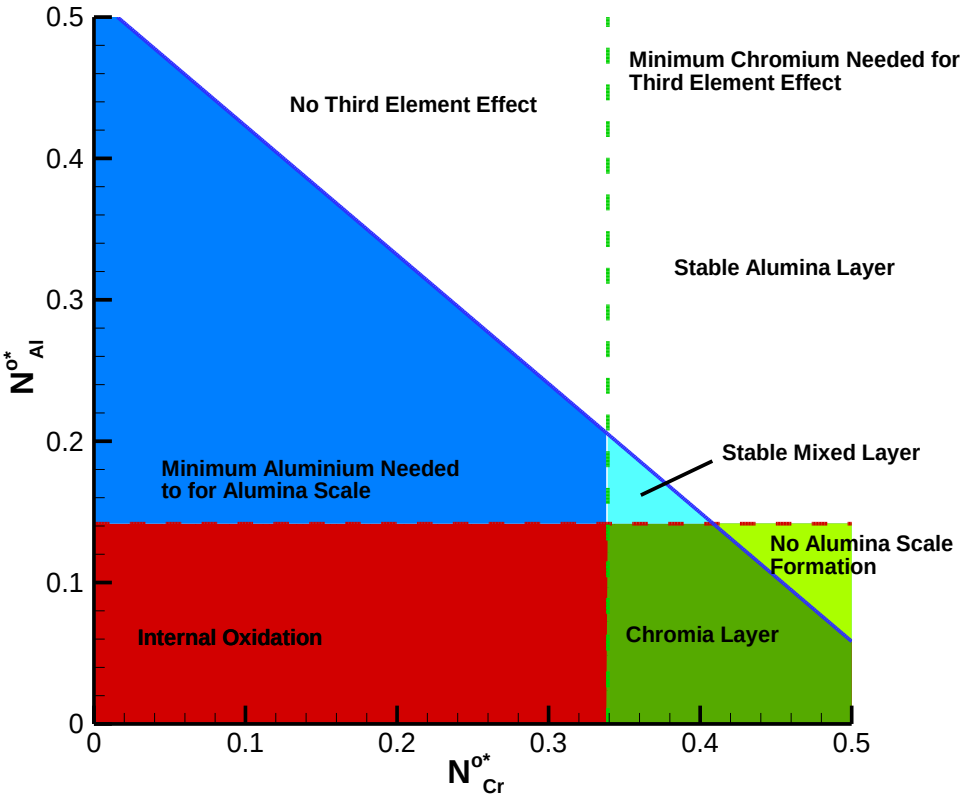

Figure 10- Schematic on how to reveal Third Element Effect on alumina formation through thermodynamics and kinetics calculations

The dark blue and green regions correspond to compositions where one would expect to see either alumina or chromia layers, respectively. The line non-orthogonal to the x and y axes correspond to the kinetic limit necessary to form a stable oxide layer impervious to internal oxidation and any composition simultaneously to the right of this line and the minimum Cr necessary to form a stable chromia layer leads to stable alumina layer. Given the non-linear interactions between alloy composition and thermodynamic and kinetic properties, there is no universal diagram for all alloys and the diagram has to be calculated for every single alloy. The position of each alloy within this diagram can suggest the expected morphology of the oxide layer and at the same time can suggest possible alloy strategies to tune the composition in order to facilitate the formation of stable passivating alumina layers. In the third element figures below, the third element graphs show the same type of trend as the effective valence contour model as seen in Figure 9.

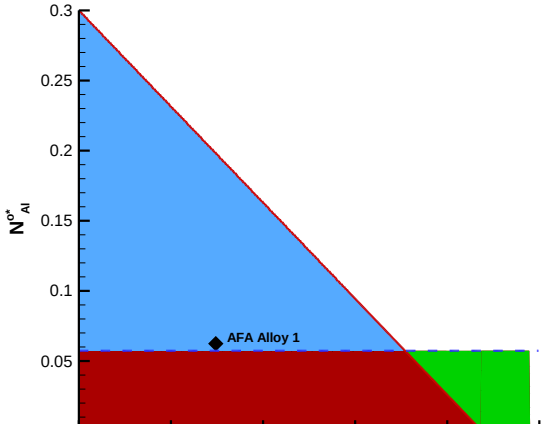

Figure 11- Third Element Effect of AFA Alloy 1

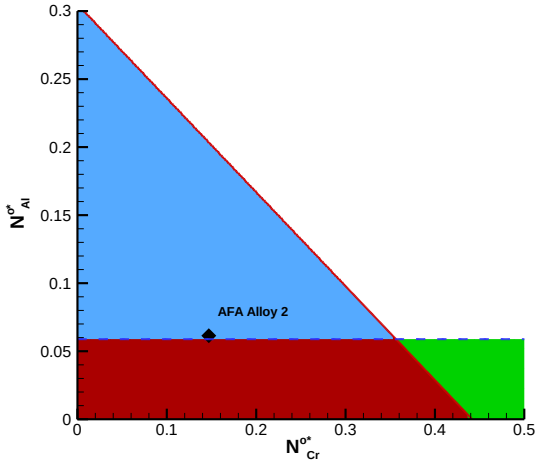

Figure 12- Third Element Effect of AFA Alloy 2

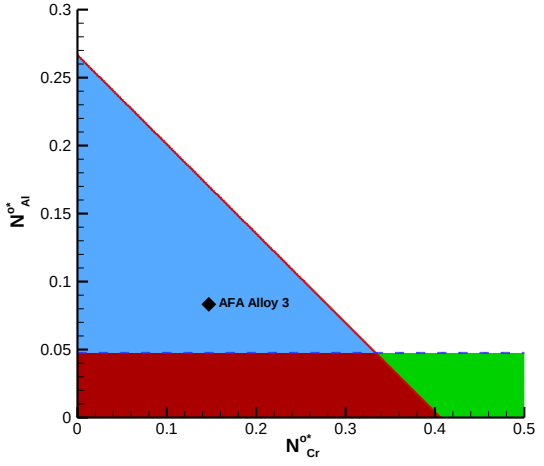

Figure 13- Third Element Effect of AFA Alloy 3

c) Discovery Process for AFSS through Genetic Algorithm (GA)

The first step in the GA programming is to generate a random population of alloys within a given composition range. Each individual alloy within the population is analyzed with a number of go/no-go criteria. For any particular individual alloy to be considered, the composition in question

needs to be suitable for the given environment; in other words, survival of the fittest. After filtering through the population, the surviving individuals are then randomly selected for reproduction of offspring, whether through cross-over or mutations, which are then utilized to repopulate the alloy population list. The creation of the random population is, as mentioned previously, done within a set range of variables which are the elements contained in the alloy composition. The domain of this search is derived from the requirements in Table3.

Table 3- Domain in GA Search for Element Optimization

Domain for Alloying Elements	Min	Max
Volume Fraction of Austenite	90%	100%
Martensite Start Temperature	~	$10^{O}C$
K Value (Effective Valence * Free Energy)	750	~
Aluminum	As low as possible	~
Chromium	As low as possible	~

The first assessment criterion is the volume fraction maximization of retained austenite. The thermodynamic properties for this alloy are calculated through Thermocalc. To pass the requirement for survival, the alloy must contain at least 99% austenite within the matrix. This leads to the next criterion which involves the stability of the austenite within the matrix. The stability of austenite is evaluated through the martensite start temperature, T_{Ms}, as well as the examination for sigma phase. With the stability of the alloy established, the next objective is the formation of the alumina oxide layer. This criterion is set up as a Boolean pass/fail due to the double-edged benefits of alumina formation. For instance, if the conditions for a stable alumina oxide layer are unfavorable, the structural properties of the material become compromised due to possible formation of undesirables such as aluminum nitride or internal alumina oxide. The development of alumina formation assessment is completed by cross-checking the information given between the effective valence and third element model described in detail in the earlier reports. As a further precaution, a small factor of safety is implemented within the alumina formation models; the K value requested of the effective valence model is set to 750 and the required minimum aluminum composition, N_{Al}, is increased by 0.005.

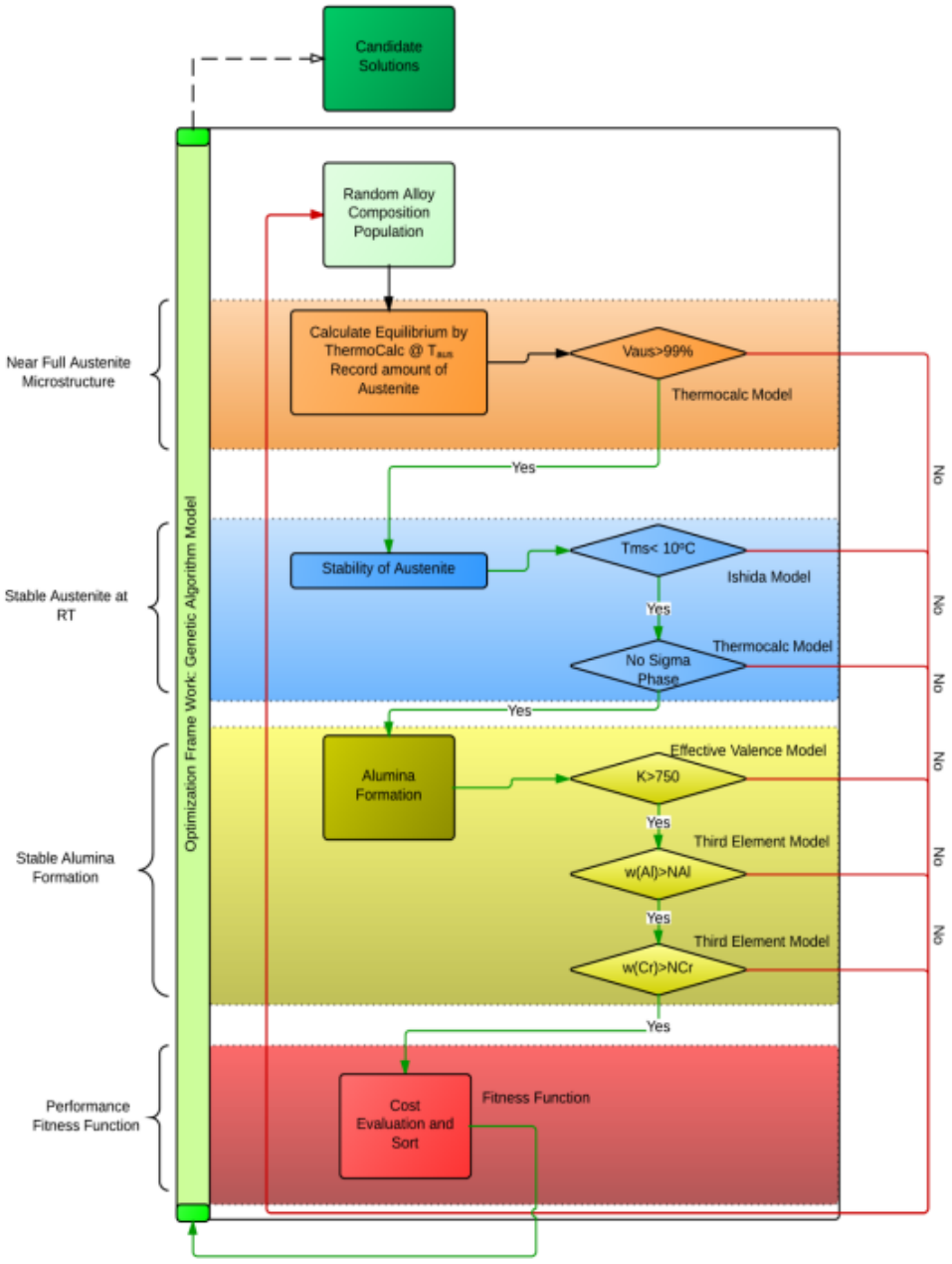

Figure 14- Genetic Algorithm alloy design path

Once a random composition acquiesces to all of the go/no-go criteria, it is given a score through a user-defined function value. The function value consists of the K value, T_{Ms}, and alloy composition cost. Using the user defined function value, the alloys that pass the set criteria is recorded into a list of candidate solutions, containing the necessary alumina formation and alloy stability information needed for making an informed alloy design decision. Figure 14 is a process map of the fitness criteria each individual alloy in the GA goes through – the alloy design path. This path can be altered to include other criteria like stacking fault energies, volume fraction of desirable phases and their stability which is the next step in the project. As the constraints for alloy composition search are extremely strict, it is observed that the alloy generated through GA contain

rather similar values for each element. Despite such similarities between some alloys there are no repeated alloys within the generated alloy list by GA. Although all of the alloy compositions are extremely similar to each other, the GA generated alloys can fall into two distinct groups, high and low manganese content coupled with low and high nickel content, respectively. We selected one of each type to give our first set of next generation alloys listed in Table 4.

Table 4- First set of predicted next-generation Alumina forming Austenitic Stainless Steels

Alloy	Fe	C	Mn	Ni	Mo	Al	Cr	Si
PGAA1	Bal.	0.073	3.893	11.000	2.026	2.994	19.820	0.382
PGAA2	Bal.	0.088	8.993	17.140	2.242	3.112	15.300	0.194

d) Machine Learning Approach to SFE Prediction in Multi-component SS

Stacking-fault energies (SFEs) of multi-component and highly alloyed stainless steels is a widely researched topic historically as well as in recent literature. For our project, it is one of the most critical materials design parameters since it controls the twinnability in stainless steel. Various experimental techniques, such as the measurement of extended dislocation nodes using TEM, measurement of partial dislocation separation using weak bean dark field TEM and X-Ray line profile analysis using X-ray diffraction are among the major methodologies used to determine SFE in addition to other sporadically used measures. Simultaneously many computational techniques like atomistic simulations and CALPHAD have been used to model SFEs as a function of composition in multi-component steels. While there are large variations in reported experimental values for even similar alloys due to the sensitive nature of experiments and also inherent assumptions applied in calculation of SFE from observed parameters, computational models have not been able to handle highly multi-component alloys due to computational limitations. This leads to absence of a go-to equation/model for calculation of SFEs. Models are typically limited to ternary systems and even then, predictions match poorly with experimental observations due to the large spread in available data. Irrespective of the methodology applied in search of this elusive value, researchers agree on highly non-linear behavior of SFE as a function of composition of various alloying elements. Also the behavior is non-monotonic and is highly dependent on various combinations arising from selection of different elements. Hence some attempts at linear regression to compute SFEs in specific compositional bounds from a few observations have also been unsuccessful to completely describe this value.

Today we live in a world filled with data. Researchers in every domain of engineering and technology are leveraging this data to find complex hidden patterns in nature and the man-made world, exploiting the readily available data and the exponential increase in computing power as well as state-of-the art data mining techniques. Machine learning/Statistical Learning/Data mining and various other interchangeably used terms, all aim at one thing – finding patterns where our physical understanding of the complex search space is woefully shallow. Machine Learning is a good technique to use when, 1) an underlying pattern exists, 2) we are unable to pin it down

mathematically, and 3) we have data on it. In our case of SFEs of stainless steels, we surely believe and know that there is some pattern dependent on factors like composition, temperature and other material properties and not a random value. As discussed above, we have yet been unable to formulate a mathematical description of the SFE's dependence on aforementioned properties which is not restricted to specific workspace and also agrees with the observed values. Also as mentioned earlier, there is abundant literature on finding SFEs and hence we have significant data.

So our three basic requirements which make machine learning a lucrative option and technique to try are being satisfied by the problem statement at hand. We hence went forward with this idea of trying to extract a pattern of SFEs in multi-component stainless steels. This methodology is thought to be a more efficient approach to use in the design of multi-component stainless steels, instead of trying to calculate the exact value of SFEs using either DFT or CALPHAD techniques.

d-1) Data Curation

In most machine learning applications, data is pretty easily available in bulk. We however do not have a well develop database for SFEs in steels. On the other hand, we have considerable data available in the literature, there is no one-stop repository which we can access to get the SFE data in a usable format. Hence we are using the Materials Data Curation System (MDCS) being developed by the National Institute of Standards and Technology (NIST) under the Materials Genome Initiative (MGI). The first version of MDCS includes:

- a web-based interface to curate, search, and retrieve materials data
- Support for federated search
- REST-based API for remote access
- Integration with scientific workflows

Data curation are efforts towards storing materials data in a semantically consistent fashion. To this end we have developed schemas to capture meta-data in the literature which can relate various material features-processing-properties to the value that we are interested in. It also makes the whole process methodological and aims at a higher motive of making a repository which can be further used by the materials community even after the results of this project are achieved.

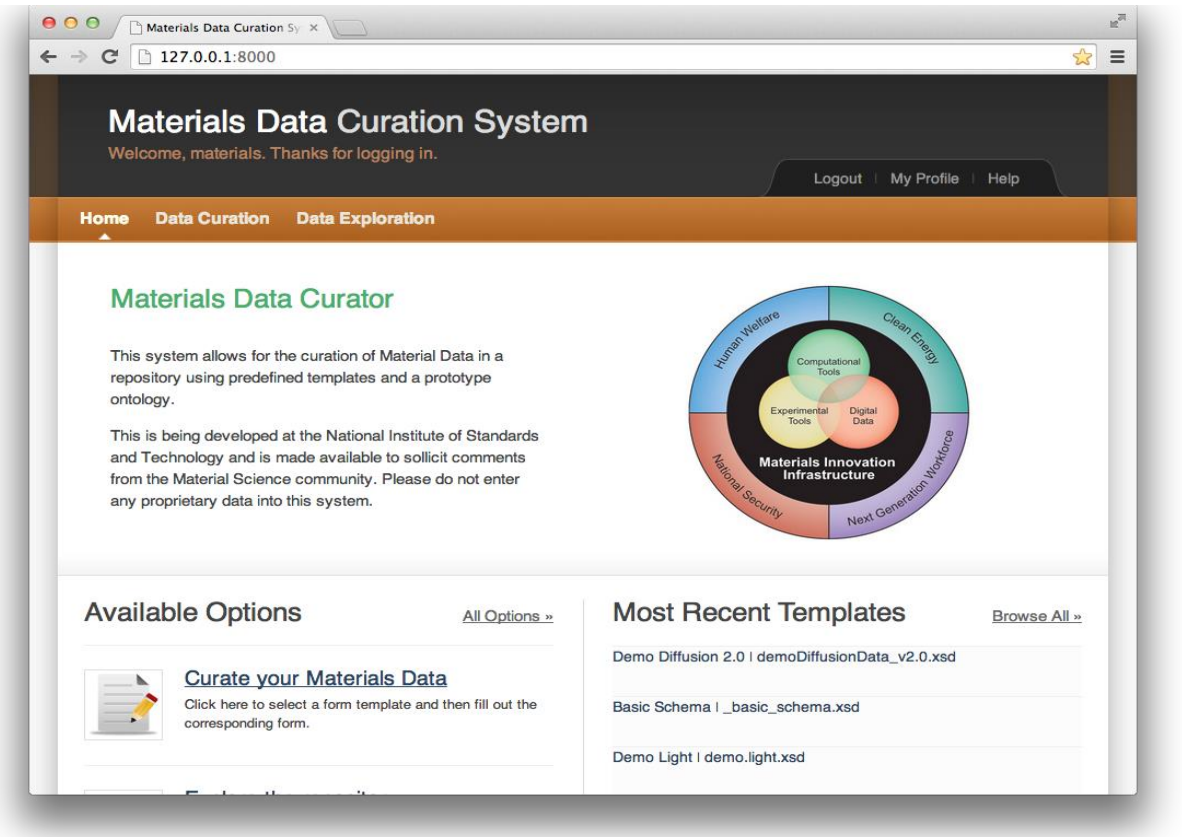

Figure 15- A snapshot of the Materials Data Curation System interface

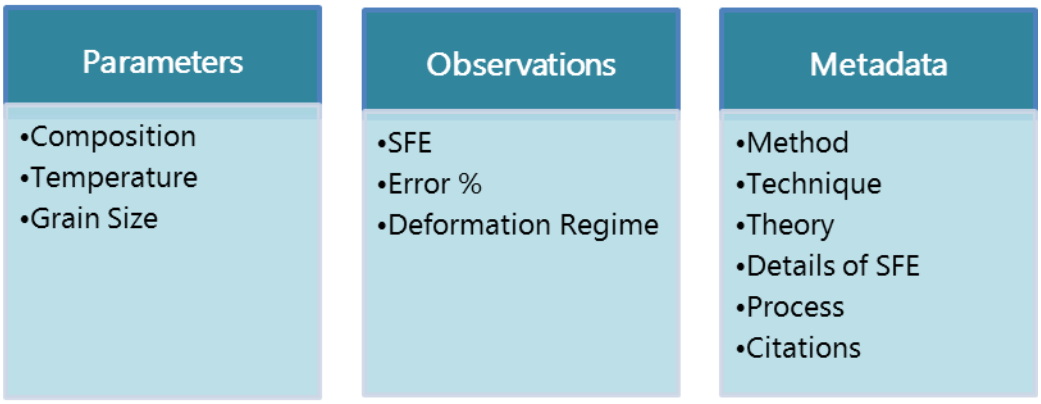

Figure 16- Details of data being captured in repository

d-2) Machine Learning approach using Artificial Neural Networks

Artificial Neural Networks are state-of-the-art highly popular and very powerful machine learning technique. They are highly efficient in capturing non-linear relations among various input parameters and can evolve incredibly complex parameters while learning which cannot be very straightforward to a human mind.

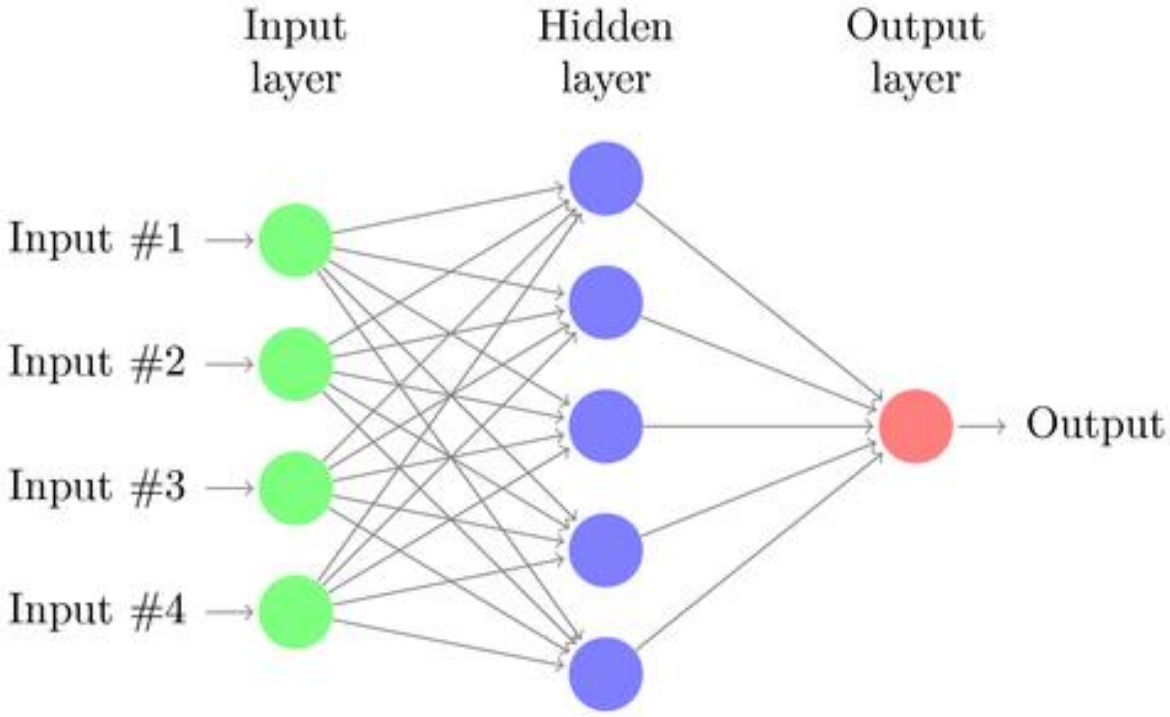

Figure 17- Representation of a basic Neural Network with 1 hidden layer

Above is a schematic of a basic artificial neural network. It can accept a large number of inputs as parameters and can also have multiple values as output. The number of hidden layers and number of nodes in hidden layers are variables which we change depending on complexity of search space. Using a logistic function, a neural network can be trained to be a very effective classifier.

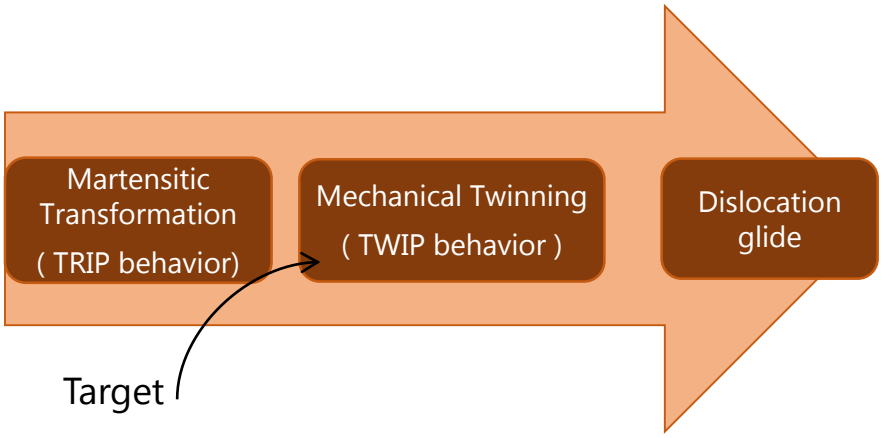

Figure 18- Schematic showing change of deformation regime with change in SFE

In the literature, SFEs in stainless steels can be classified in 3 ranges: low, medium and high. Low SFEs promote epsilon martensite formation during deformation, medium SFEs promote deformation via twinning while high STE steels deform by dislocation glide. Since our aim is to design alloy which will primarily deform by twinning, if we can train a neural network that

effectively classifies steels in these three buckets, our aim will be achieved. It is a practical model where we do not want to predict the exact value of stacking fault energy but predict consequence of a particular range of values. It also helps in absorbing the high uncertainty associated with SFE measurement in the literature.

We have currently built a classifier using the data that we have collected and stored in the MDCS over the past few months. We intend to make it very robust by gathering extensive data and also using the most current techniques available in machine learning to make a model that generalizes well to new data points.

d-3) Results using the Artificial Neural Network classification model

Below is a snapshot of results using the classifier we built. The smaller filled points are the training data for the classifier with the horizontal lines depicting the error bars in the data. The colour signifies their label among the three classes. The larger points are the test data where filled points are the ones which the classifier identified correctly while unfilled points are the one that classifier mislabeled. On careful investigation, one sees that the points that classifier misclassified are the ones very close to the boundary of separation between classes.

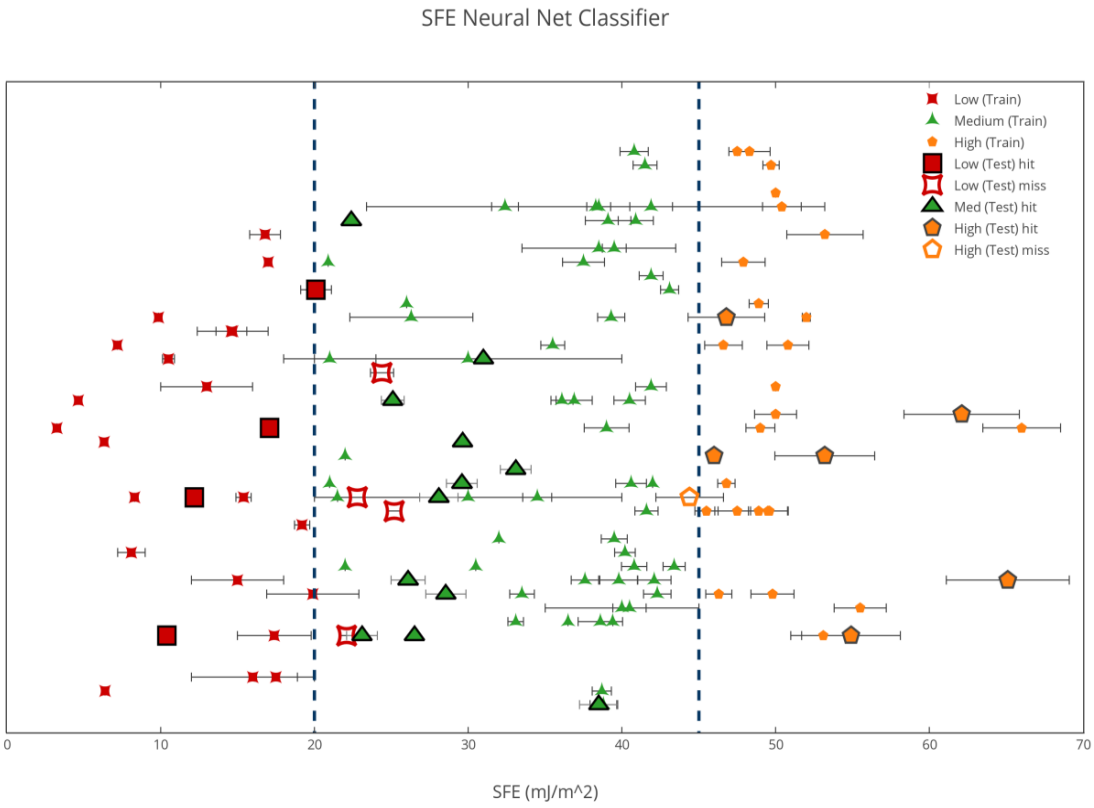

Figure 19- Results of the Neural Net Classifier on SFE

We are building a one stop repository for SFE data of Austenitic Stainless Steels and also in process to release the classifier to the community which will be crucial to accelerating alloy design in steels.

2. Hadfield Steel

Deformation twinning has been successfully induced after 5%, 10%, and 20% tensile straining at room temperature on three identical single crystalline samples oriented along the [111] direction. This orientation is selected in particular because from our past experience, we knew that this orientation undergoes deformation twinning. Before deformation, the samples were polished till a mirror like finishing. The polished surfaces were directly characterized under Optical Microscopy after deformation. Figure 2020shows the gage section of the sample after various strain levels. After 5% strain (Figure 2020-a), some surface relief/twining regions start to appear at the left side of the gage section (shown as the needle like feature). The volume fraction of these regions increases with the strain level. After 20% strain, these surface relief/twining regions cover the entire surface.

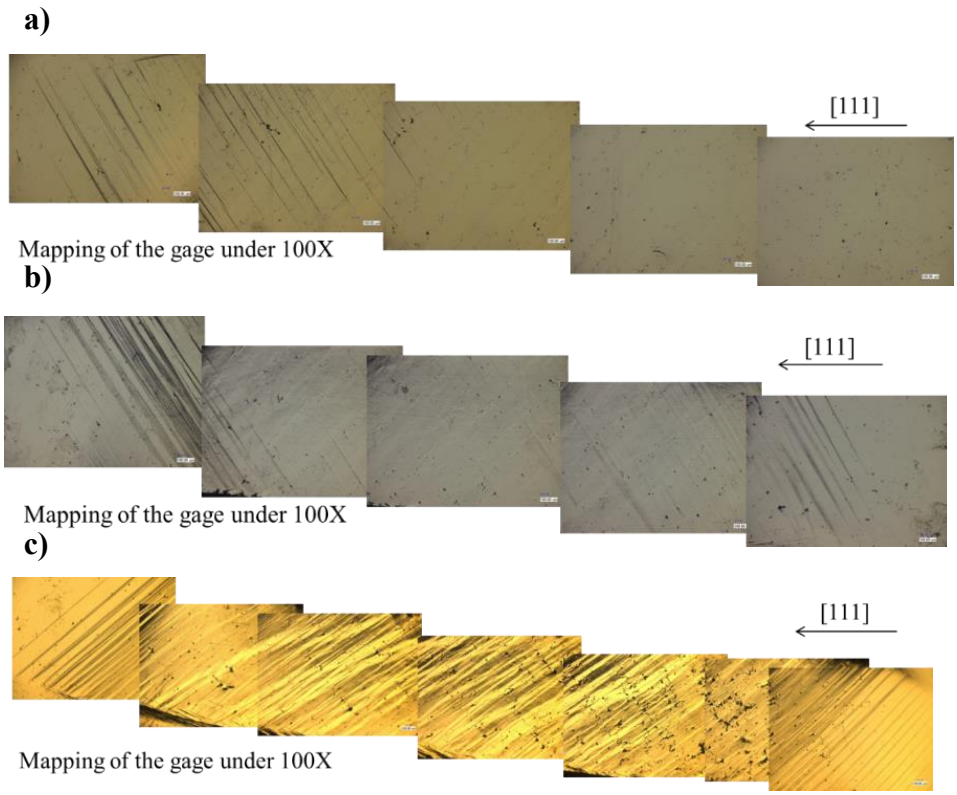

Figure 20- Optical images of the Fe-13Mn-1.1C (in wt.%) single crystals oriented along the [111] direction after 5% (a), 10% (b), and 20% (c) tensile strains. Samples were polished before testing. Needle like features indicate deformation twinning or surface relief.

It was concluded that the surface relief/twinning regions observed under optical microscopy indeed included deformation twinning. Figure 214 shows the inverse pole figure of the material after 20% strain. The strong texture (indicated by the two poles) in each inverse pole figure is the evidence for the appearance of deformation twining.

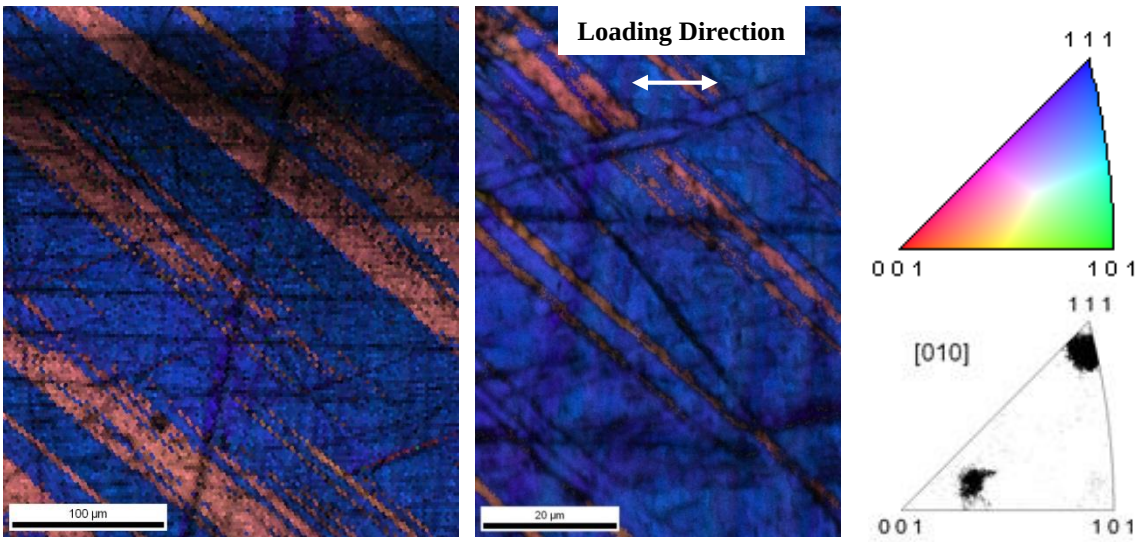

Figure 21- EBSD image and the inverse pole figure of the Fe-13Mn-1.1C (in wt.%) single crystals oriented along the [111] direction after 20% tensile strain.

To characterize the high temperature stability of the deformation twinning in the material, the deformed samples (after 20% tensile strain) were annealed either at 500°C or 600 °C for 1hr. The sample was then electro-polished and characterized under EBSD. Figure 22 shows the inverse pole figure of the sample after annealing. The strong texture (Figure 2121) is now replaced by a relatively weak one, as indicated by the multiple strong poles in the inverse pole figure. This means that after annealing at 500°C the sample is partially recrystallized. The stability of deformation twinning is not excellent in this material at the temperature if no precipitates exist to pin the twin boundary.

600°C 1 hr annealing has also led to a partial recrystallization in the [111] oriented single crystals after 20% strain, similar to the results observed after 500°C 1 hr annealing, indicating that some of the twins are stable up to 600°C. The EBSD analysis of the 600°C annealed sample (Figure 23) revealed that alpha phase (ferrite, shown in green) evolves as a second phase in the microstructure. From the few EBSD patterns, it seems like there are no obvious nucleation sites for the second phase. The red area in the figure is the gamma phase (austenite). To better understand these observations, the phase diagram of the alloy (Fe-13Mn-1.1C in wt%) was predicted as shown in Figure 4. Using the composition of 17Cr-12Ni-2.5Mo-2Mn-1Si-0.08C in Thermocalc, the volume fraction of the phases are calculated as be seen below.

At 600°C (i.e 873K), ferrite, austenite and cementite coexist in the microstructure, which explains the experimental observations. Moreover, newly formed ferrite phase doesn't appear to have any preferred orientation, while the deformation twinning still remained as indicated by the inverse pole figures for each phase (Figure 24). Recalling that the goal for the investigation of the single crystalline materials with high twin volume fraction is to find out the evolution of deformation twinning (e.g. the thermal stability, its relation with recrystallization) at high temperatures, the appearance of this second phase (ferrite) is undesirable. Thus, Fe-13Mn-1.1C (in wt.%) alloy (Hadfield steel) seems unsuitable for the present goals.

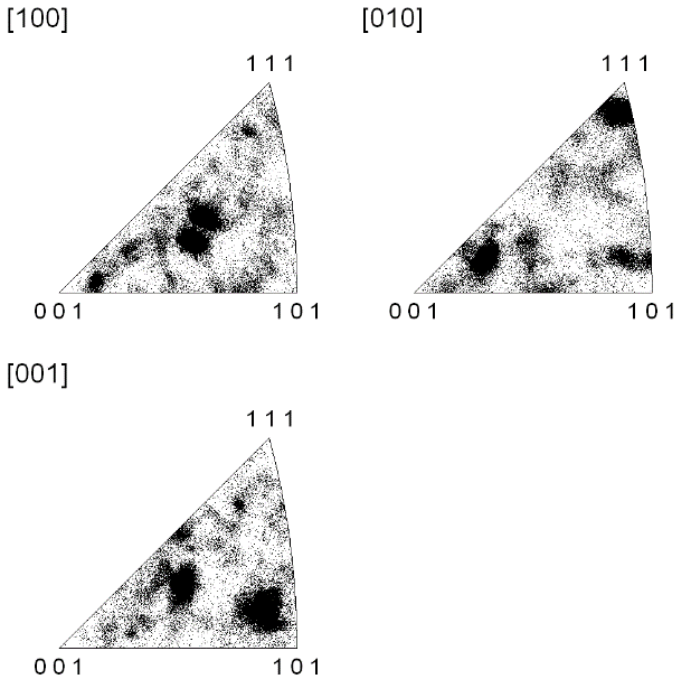

Figure 22- Inverse pole figures of the Fe-13Mn-1.1C (in wt.%) single crystals oriented along the [111] direction after 20% tensile strain and 500°C 1hr annealing.

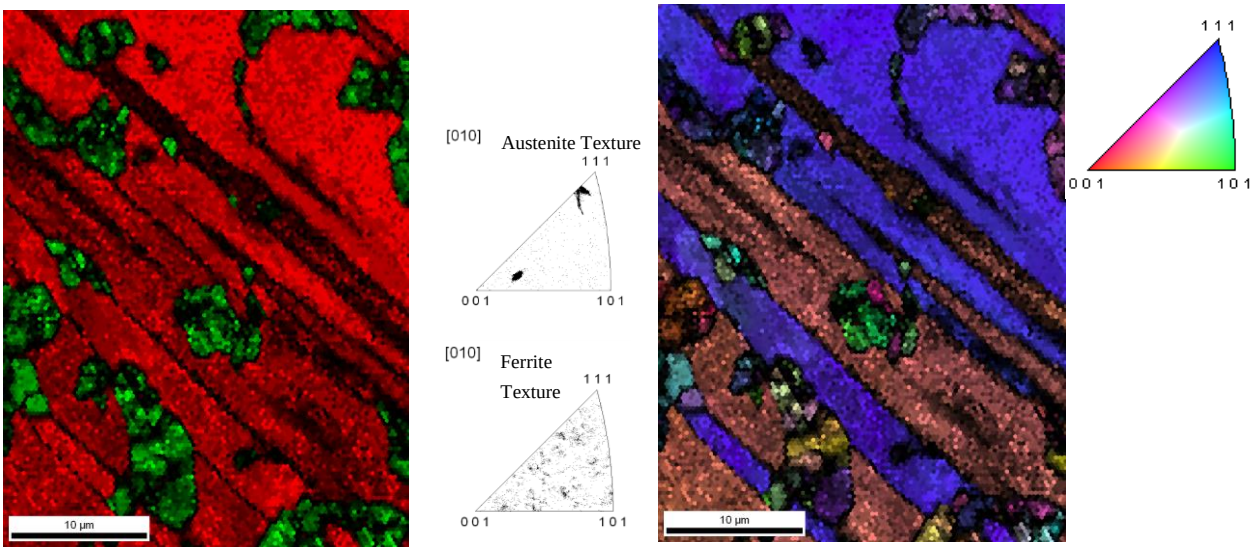

Figure 23- EBSD of Fe-13Mn-1.1C (in wt.%) single crystals oriented along the [111] orientation after 20% tensile strain and annealing at 600°C for 1 hour. Left) showing two phases: green - alpha (ferrite) phase, red - gamma (austenite) phase. Right) The EBSD image of Fe-13Mn-1.1C (in wt.%) single crystals oriented along the [111] orientation after 20% tensile strain and annealing at 600°C for 1 hour. The inverse pole figures on the middle are for austenite and recrystallized ferrite.

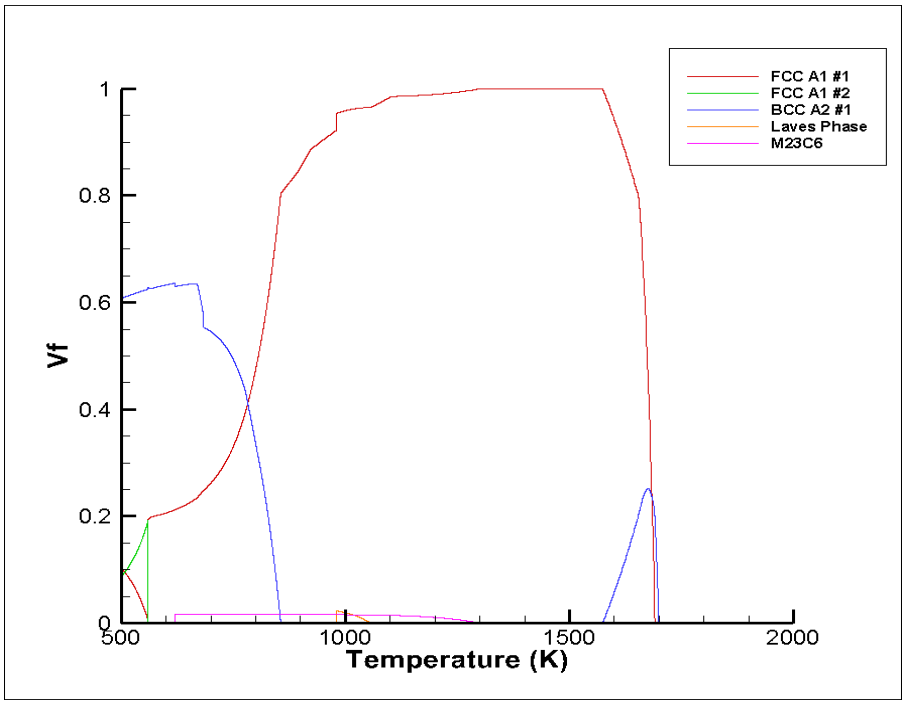

Figure 24- Volume fraction of the phases present in the 316 stainless steel as a function of temperature

3. Baseline Austenitic Stainless Steel

a) 316N Stainless Steel

Figure 25 shows the axial tension test result of 316N single crystals with [111] orientation at room temperature and -80°C. It can be seen that the stress-strain behavior follows the same trend in both temperatures, with the only significant difference in the yield strength values. Given that plastic region of both curves are similar, it appears that the same mechanism has the major role for deformation at both temperatures. Figure 26 shows the Optical Microscopy (OM) and Scanning Electron Microscopy (SEM) image of the surface of the 316N [111] single crystal with 10% tension deformation at room temperature. In Figure 26-a, straight parallel features are visible on the surface after 10% deformation. Figure 26-b shows that these features aren't completely straight, and they are densely packed. Figure 27 shows OM (a) and SEM (b) image of the surface of the 316N [111] single crystal with 10% tension deformation at -80°C. The OM image (Figure 9-a) suggests that these features occur more frequently on the surface as compared to the sample deformed at room temperature.

Figure 28 28-a shows the Inverse Pole Figure (IPF) results obtained from EBSD of 316N [111] single crystals deformed 10% at room temperature. The IPF analyses indicate that the deformation mechanisms at the studied regions must have been slip and not twinning, because the crystal orientation is close to {111} (slightly skewed from this pole due to slip), and no {112} (which would be a result of twinning in this system) orientation is detected. The same results were obtained from EBSD analyses of the 316N [111] single crystal with 10% deformation in -80°C (Figure 28-b). It can be seen in this image the inverse pole figures have skewed less than those of the room temperature. This can be inferred that less slip has occurred in the sample deformed at -80°C.

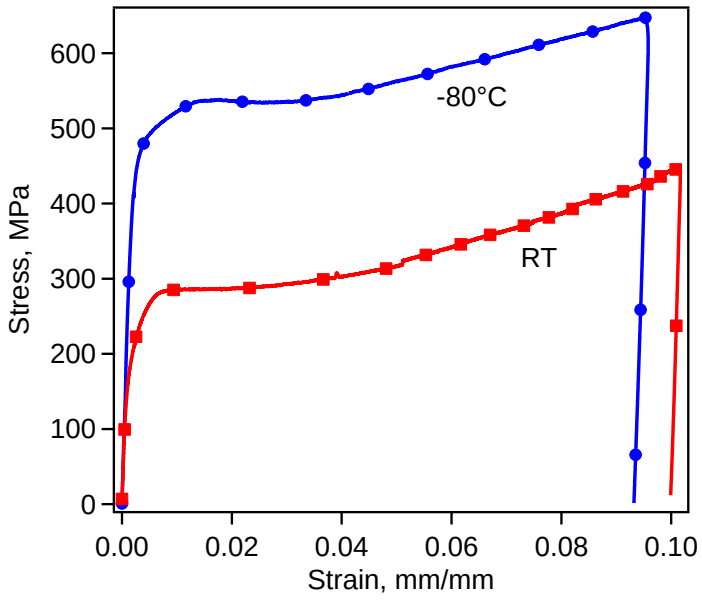

Figure 25- True stress vs. strain response of 316N [111] single crystals at room temperature and -80°C up to 10% elongation

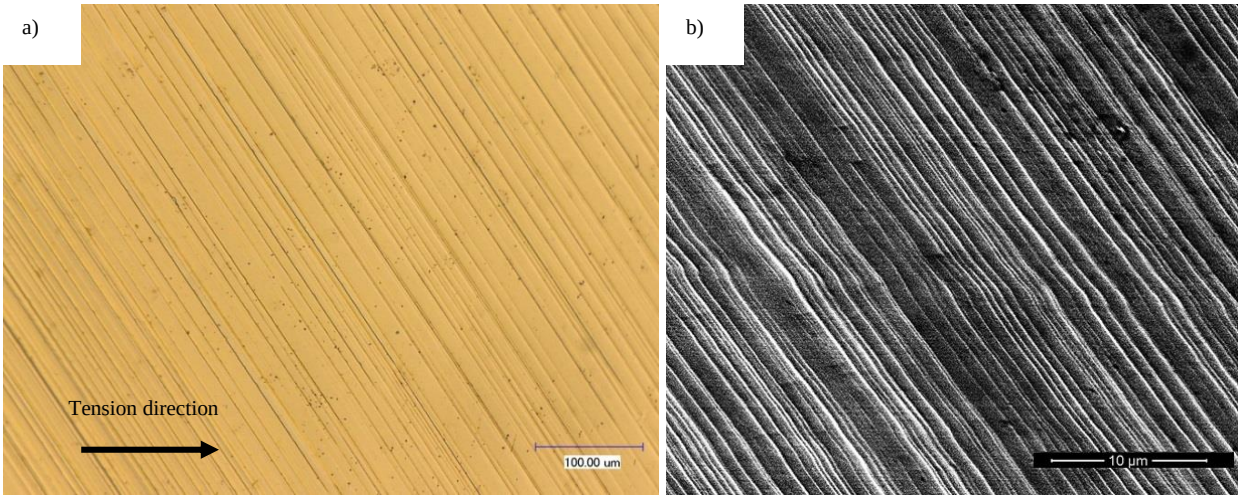

Figure 26- a) OM and b) SEM image of 316N [111] single crystals after 10% axial tension at room temperature

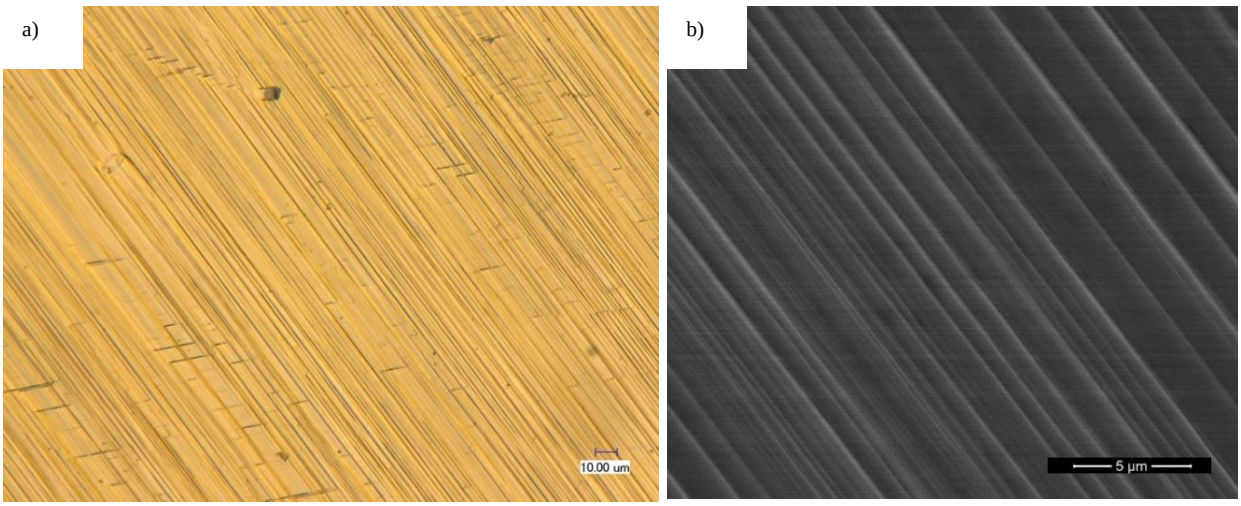

Figure 27- a) OM and b) SEM image of 316N [111] single crystals after 10% axial tension in -80°C

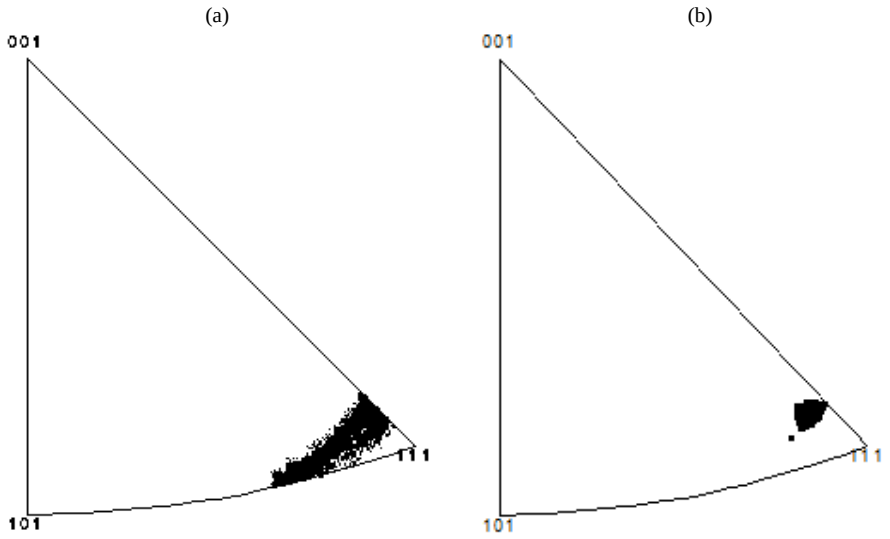

Figure 28- Inverse Pole Figures (IPF) of 316N [111] single crystals deformed to 10% strain at a) room temperature and b) -80°C, measure using EBSD

With these unexpected results, 316N [111] single crystal sample deformed to 10% strain at -80°C were studied using Transmission Electron Microscopy (TEM) next. The acquired images, shown in Figure 29, show little sign of twinning and support the EBSD finding that the major deformation mechanism has, in fact, been dislocation slip. However, very small bands are visible in some regions (middle of Figure 29-b) that can be nano-scale twinning. Finding and determining these nano-sized bands using other techniques such as EBSD is impossible. Further TEM work and HRTEM studies are needed to identify these features. Dislocations, on the other hand, can easily be seen in the bright field TEM image (Figure 29-a and b). The selected area diffraction (SAD) pattern in Figure 29-c also shows no sign of additional peaks related to twinning, which again can be attributed to the small size of the twin bands.

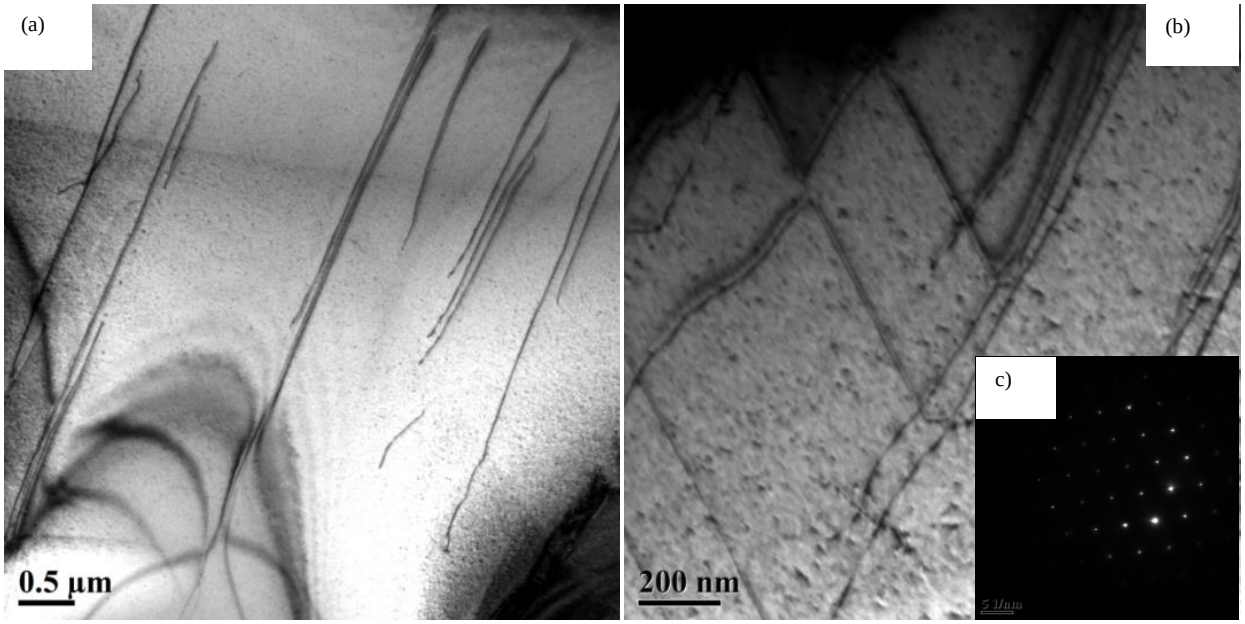

Figure 29- TEM bright field images ((a) and (b)) and corresponding SAD pattern ((c)) of 316N [111] single crystals deformed to 10% strain at -80°C

Assuming that 10% deformation have not sufficed for producing twinning large and frequent enough to be detected, 316N [111] single crystals were deformed for 20% at -80°C (Figure 30-a) using uniaxial tension. OM of the surface revealed surface features more closely packed and denser than those after 10% strain (Figure 30-b), which is obviously a consequence of the larger deformation. Next, deformed samples were studied using EBSD, and all the obtained IPF analysis indicates a pole near {112} (Figure 30-c). This result show that either all the scanned area has been within a twin band or the un-deformed single crystal had an orientation other than [111]. To double check the original orientation of the single crystal, another undeformed sample from the same 316N [111] single crystal batch was used for EBSD analysis. Figure 30-d shows the results, and as it can be seen, the original orientation is actually not [111], but [112] which after deformation by slip, shifts towards the obtained IPF in Figure 30-c. These results show that the amount of nitrogen does not affect or negatively affects the twin-ability of 316L stainless steel at this given nitrogen concentration.

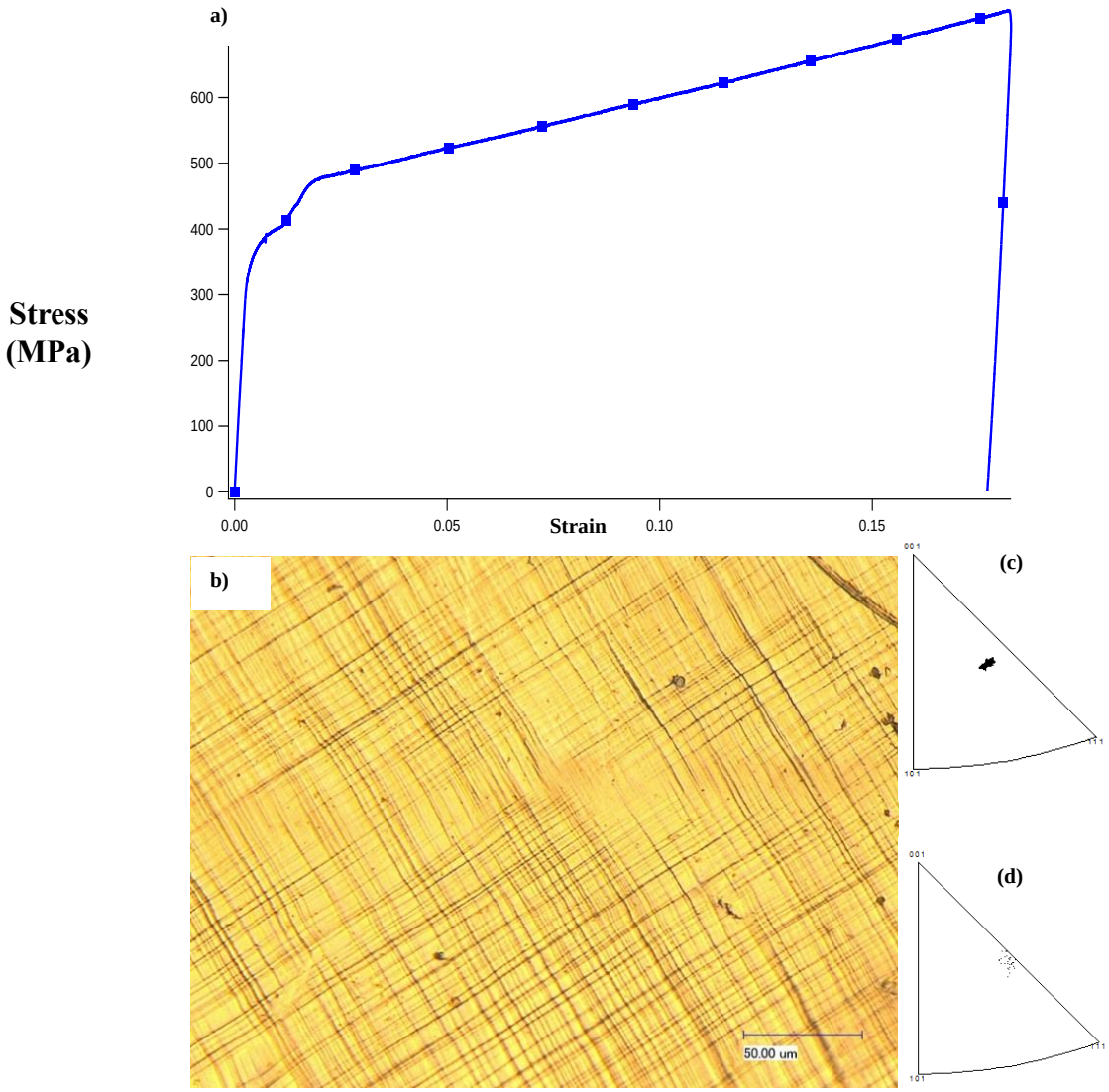

Figure 30- 316N [111] single crystals a) deformed to 20% strain at -80°C, b) OM and c) IPF of this sample, and d) IPF of an undeformed 316N [111] single crystal sample from same batch

Two additional samples of 316N [111] single crystals were deformed uniaxially at room temperature and -80°C, and their hardness was measured using Vickers microhardness with 300gf load both before and after tension test on several locations on the deformed region of the samples. The results of these measurements are provided in Figure 31. These results indicate a significant, and expected, increase in hardness due to the plastic deformation. Then the 316N [111] single crystal sample deformed to 10% strain at -80°C were cut into 3 similar pieces where each was individually heat treated for 1 hour at 400°C, 500°C, and 600°C, respectively, in order to evaluate the recrystallization temperature. The hardness drops back to its original value at a temperature between 400 and 500°C, implying that the recrystallization temperature is somewhere in this range, thus, making this range interesting for further investigation.

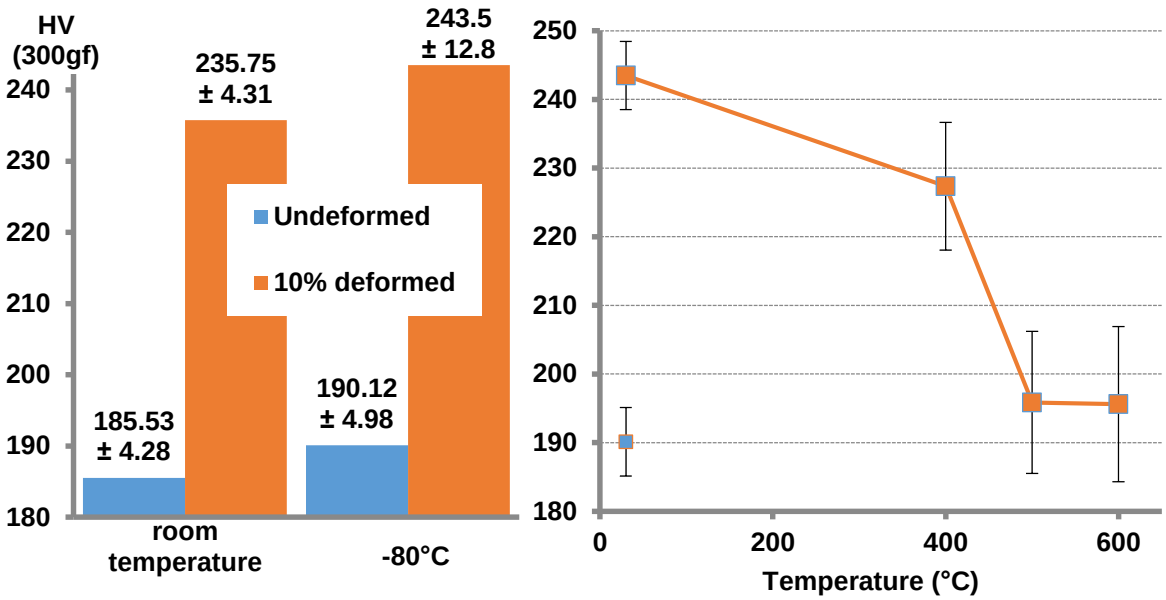

Figure 31- left) 316N [111] single crystals hardness before and after 10% deformation at room temperature and -80°C, right) microhardneass of 316N [111] single crystal sample pre-deformed to 10% at -80°C then heat treated for 1 hour at 400, 500, and 600°C

a) 316 Stainless Steel

Given that the 316N single crystals had questionable orientations, and also to test our hypothesis with another austenitic stainless steel, conventional 316 [111] single crystals were used for thermo-mechanical testing and EBSD analysis. 316 [111] single crystals were cut into dog bone-shaped specimens and were heat treated for 12 hours at 1080°C, then at 1100°C for 1 hour and consequently water quenched, in order to homogenize the microstructure. One sample was then used in uniaxial tension test for 20% deformation at room temperature (Figure 32). EBSD results of this sample are shown in Figure 33. The results show that a twinning texture of {111}/{112} exists, and the band of the twins vary from less than 1μm to larger than 40μm.

The 20% deformed 316 [111] single crystal samples was studied using TEM. Figure 34 shows two TEM images of this sample. In Figure 34-a, a 10nm wide band can be detected, and Figure 34-b shows the diffraction, indicating that this is twinning. Also Figure 34-c shows another set of bands, around 100nm wide, with the corresponding diffraction pattern in Figure 34 34-d, it is suggested that these bands may be stacking faults. These TEM and EBSD results are promising and investigation will continue on optimizing the twin size and its interaction with precipitates, as well as other mechanical properties at room temperature and high temperature.

The dog bone-shaped 316 [111] single crystals, that had been heat treated for 12 hours at 1080°C then at 1100°C for 1 hour and consequently water quenched, were deformed for 20% in uniaxial tension test at room temperature. The optical microscopy images of these samples (Figure 35) show significant parallel surface features that are potentially an indication for twinning.

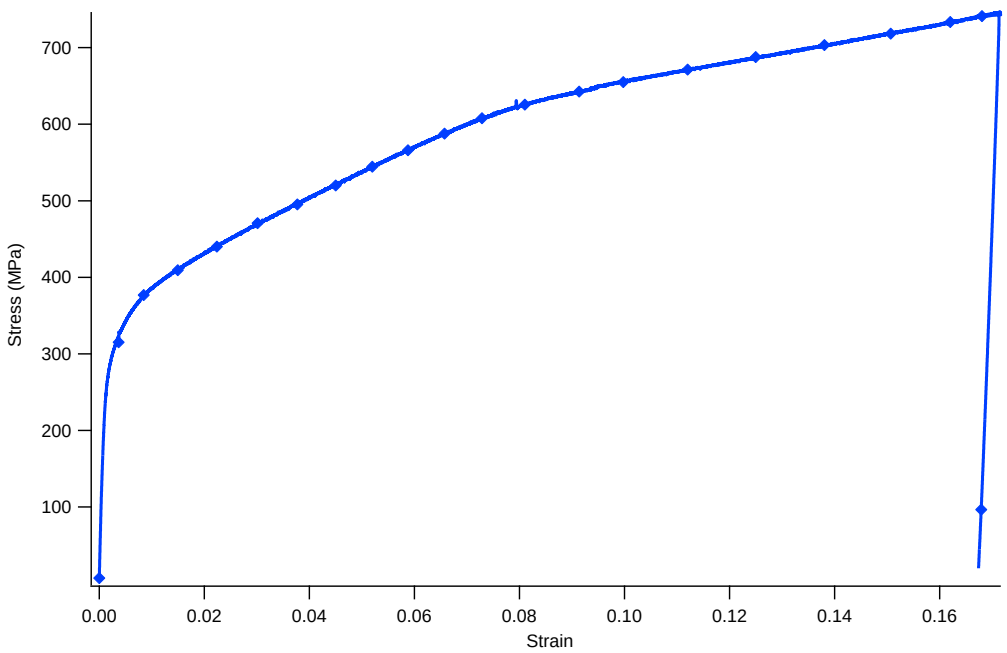

Figure 32- Strain-Stress behavior of 316 [111] crystal sample uniaxial tension test at room temperature

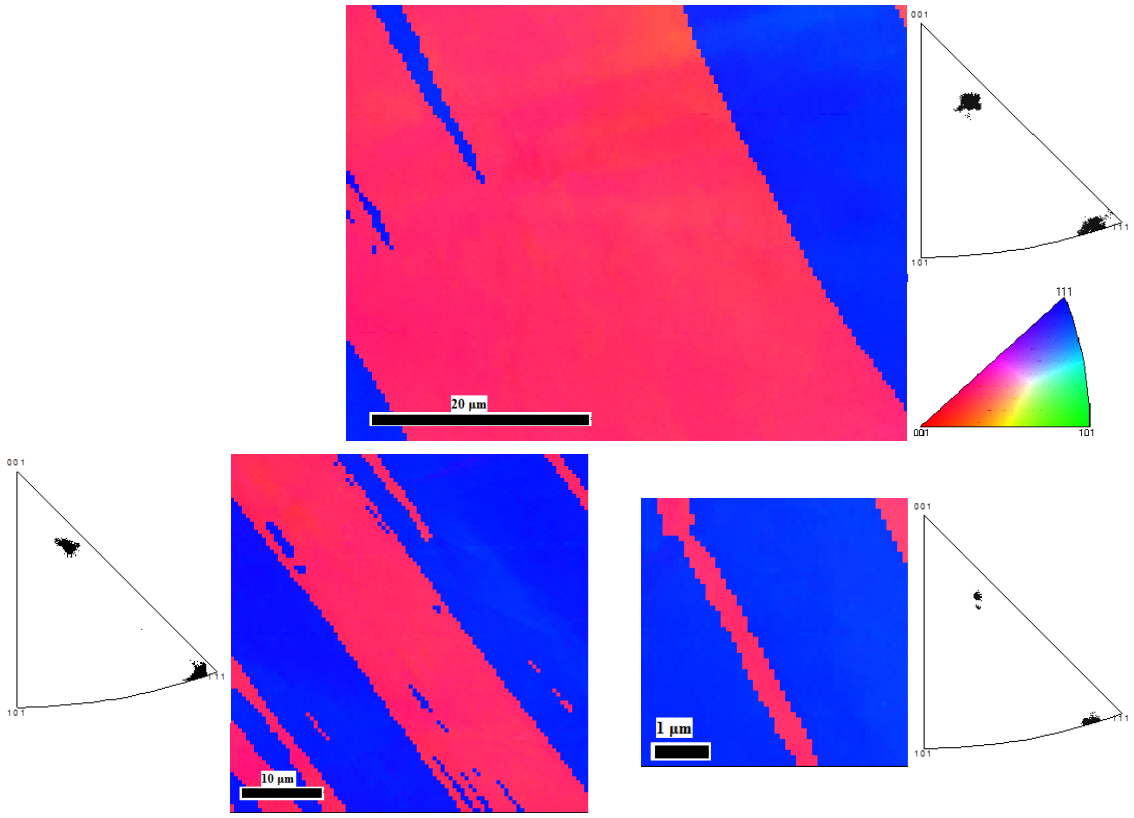

Figure 33- EBSD analysis of 316 [111] single crystals deformed to 20% at room temperature

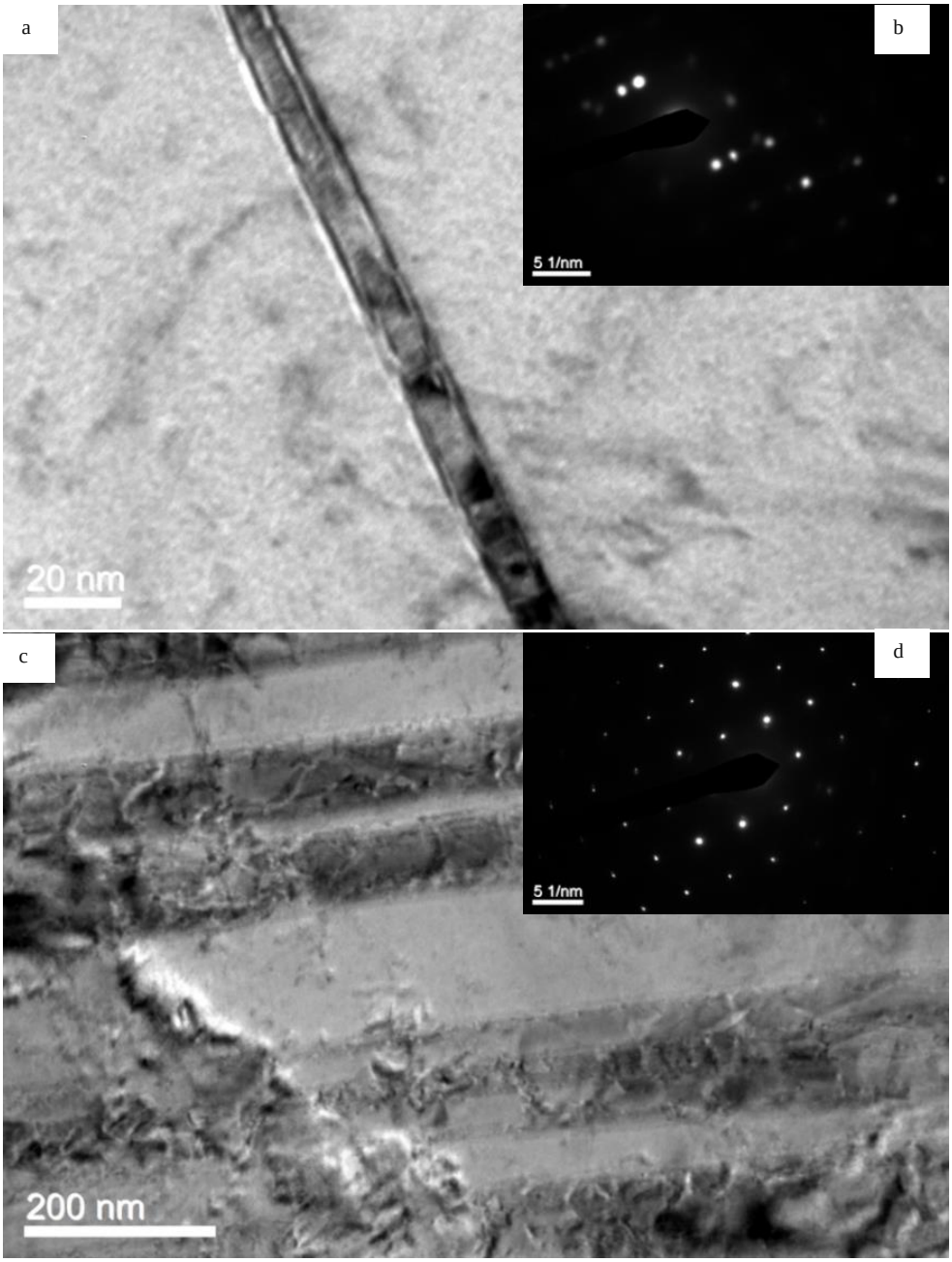

Figure 34- TEM images of 20% deformed 316 [111] single crystal samples

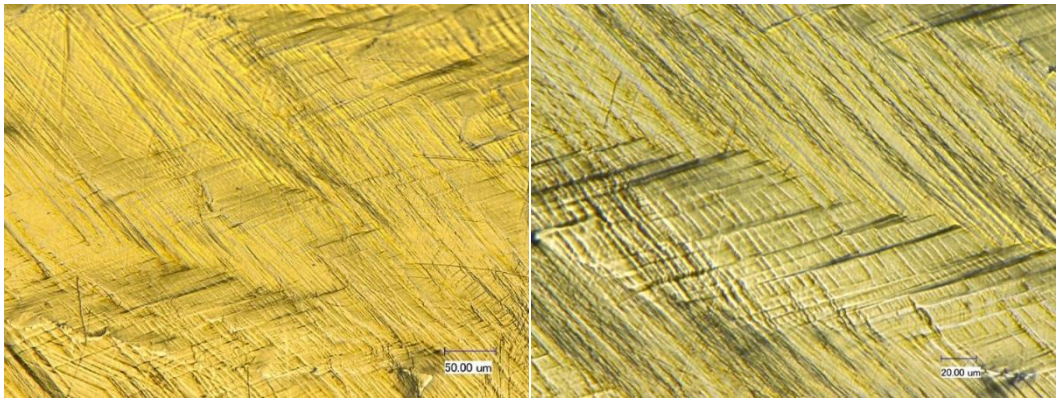

Figure 35- OM images of stainless steel 316 [111] single crystal deformed 20% at room temperature

These samples, after being polished, showed presence of a second phase (Figure 36-a), which after being investigated using Backscattered and Secondary Electron Microscopy and Energy Dispersive Spectroscopy, appeared to be rich in Chromium and Iron (Figure 36-c to e). The quantitative results of this analysis are presented in Table 5. By comparing the elements percentages of the precipitate with those of the surrounding (Table 6), it can be seen that Fe and Cr have an almost 2:1 atomic percentage ratio in the precipitate, and also that the precipitate is richer in Mo than the matrix. Based on the Fe-Cr-Ni and the composition, the precipitate appears to be χ-phase. To make sure, the mass percentages of elements in χ-phase were theoretically calculated using Thermocalc (TCFE 6 Database). The calculated results (Figure 37) show good match with the observed values for the precipitates, supporting the suggestion that the precipitate is χ-phase. The importance of this phenomena is that this phase, which may show up after long exposure to high temperatures, is considered a weak phase and may cause failure in the system during application, and therefore, must be avoided.

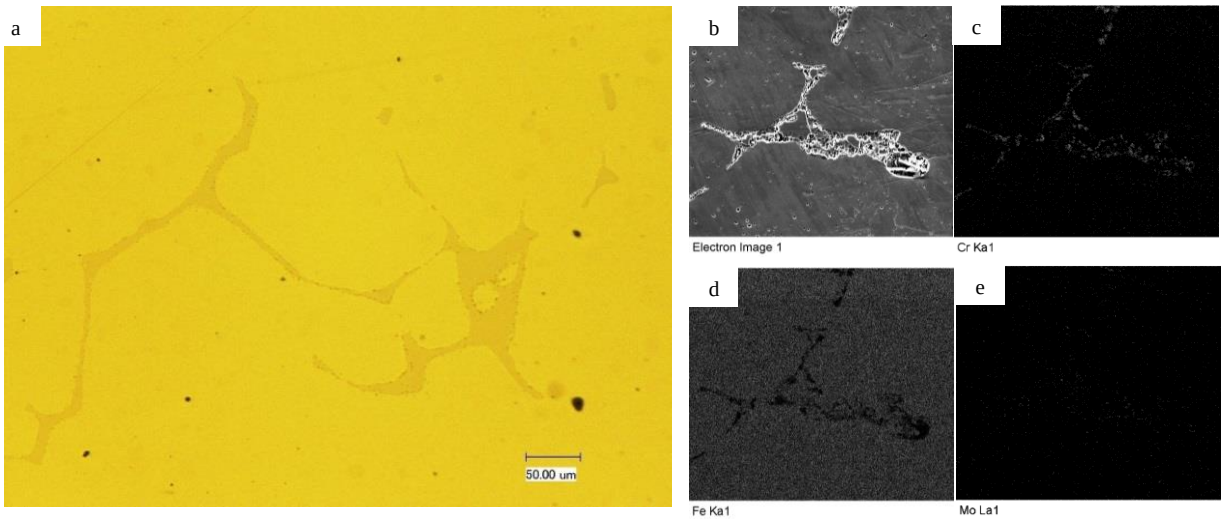

Figure 36- OM images of polished surface 316 [111] single crystal deformed 20% at room temperature, b) SEM image of the precipitate, c) elemental mapping of Cr, d) elemental mapping of Fe, e) elemental mapping of Mo

Table 5-Composition of the precipitate shown in Figure 36-b

Element	Weight%	Atomic%
C	2.18	9.12
O	1.14	3.57
Si	0.55	0.99
Cr	26.01	25.11
Mn	1.59	1.46
Fe	58.44	52.53
Ni	5.92	5.06
Mo	4.16	2.18

Table 6-Composition of the matrix around the precipitate shown in Figure 36-b

Element	Weight%	Atomic%
C	1.94	8.00
O	2.06	6.38
Si	0.72	1.28
Cr	18.05	17.18
Mn	1.72	1.55
Fe	63.57	56.34
Ni	9.51	8.02
Mo	2.42	1.25

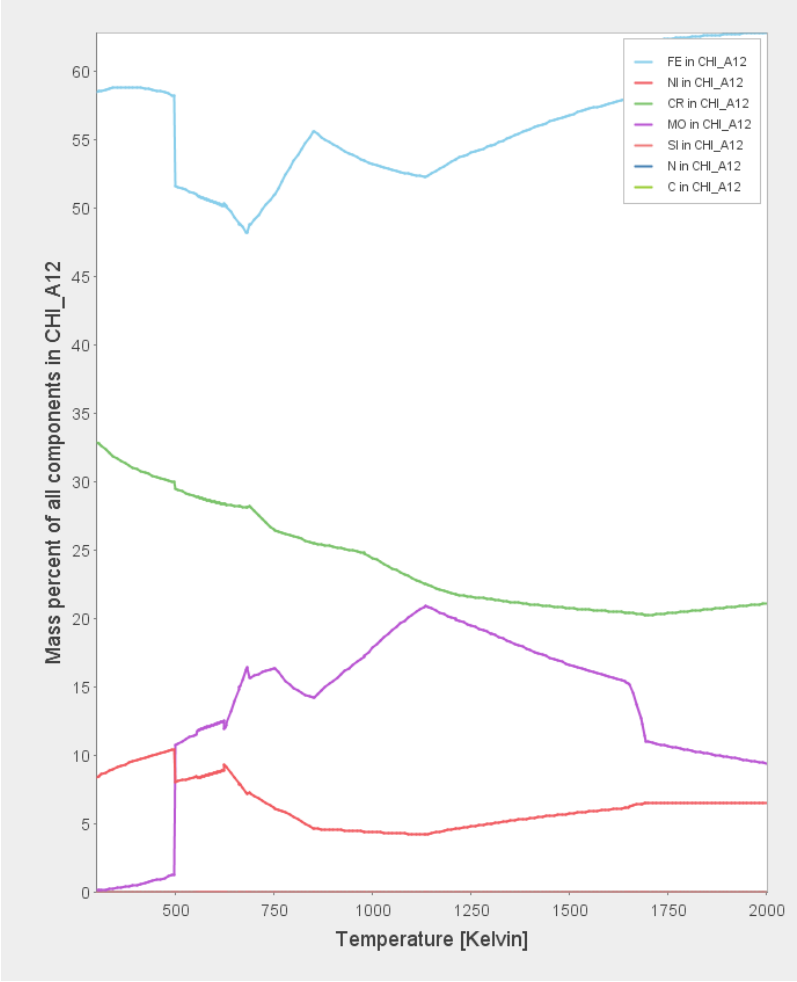

Figure 37- Calculated mass percentage of alloying elements of stainless steel 316 in χ-phase

The samples were then studied using EBSD for crystalline orientation, and the resultant map (Figure 38) shows twin bands across the samples which, in some regions, are almost 20µm wide. The inverse pole figure confirms that a twinning texture of {111}/{112} exists. Furthermore, samples were studied using TEM as well, and the bright field image (Figure 39) shows a twin band

almost 2µm wide. The diffraction patterns of the upper boundary (Figure 39-b) and the lower boundary (Figure 39-c) confirm the twinning nature of the feature.

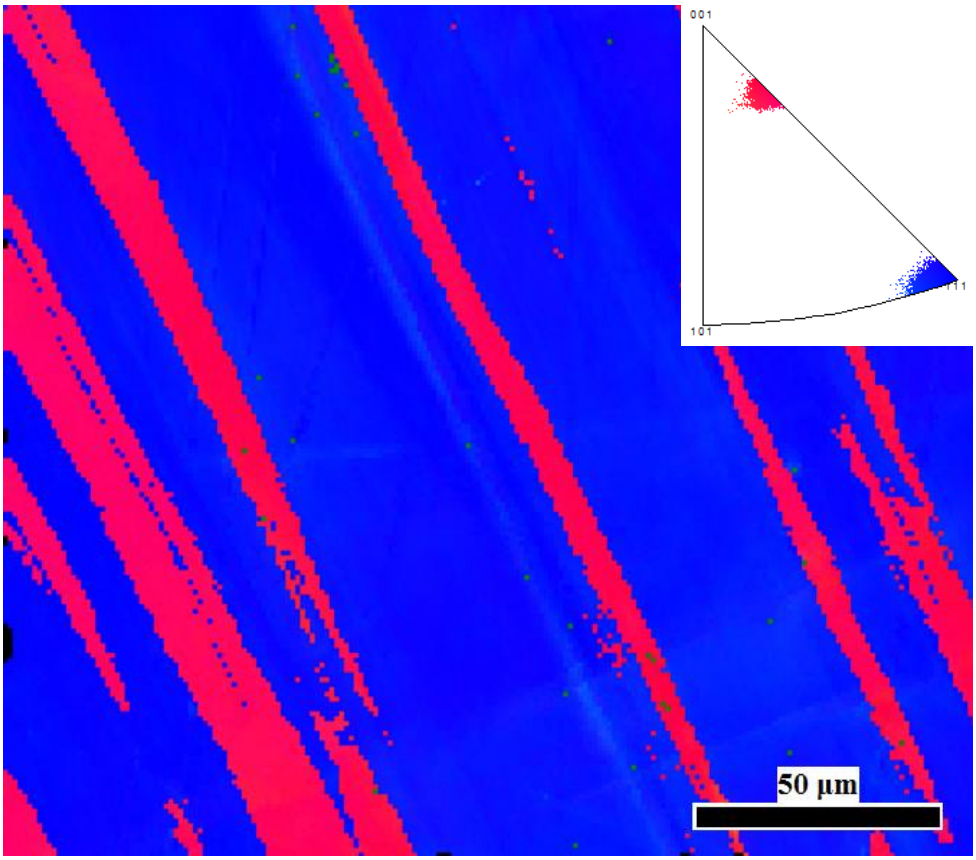

Figure 38- EBSD map of 316 [111] single crystal deformed 20% at room

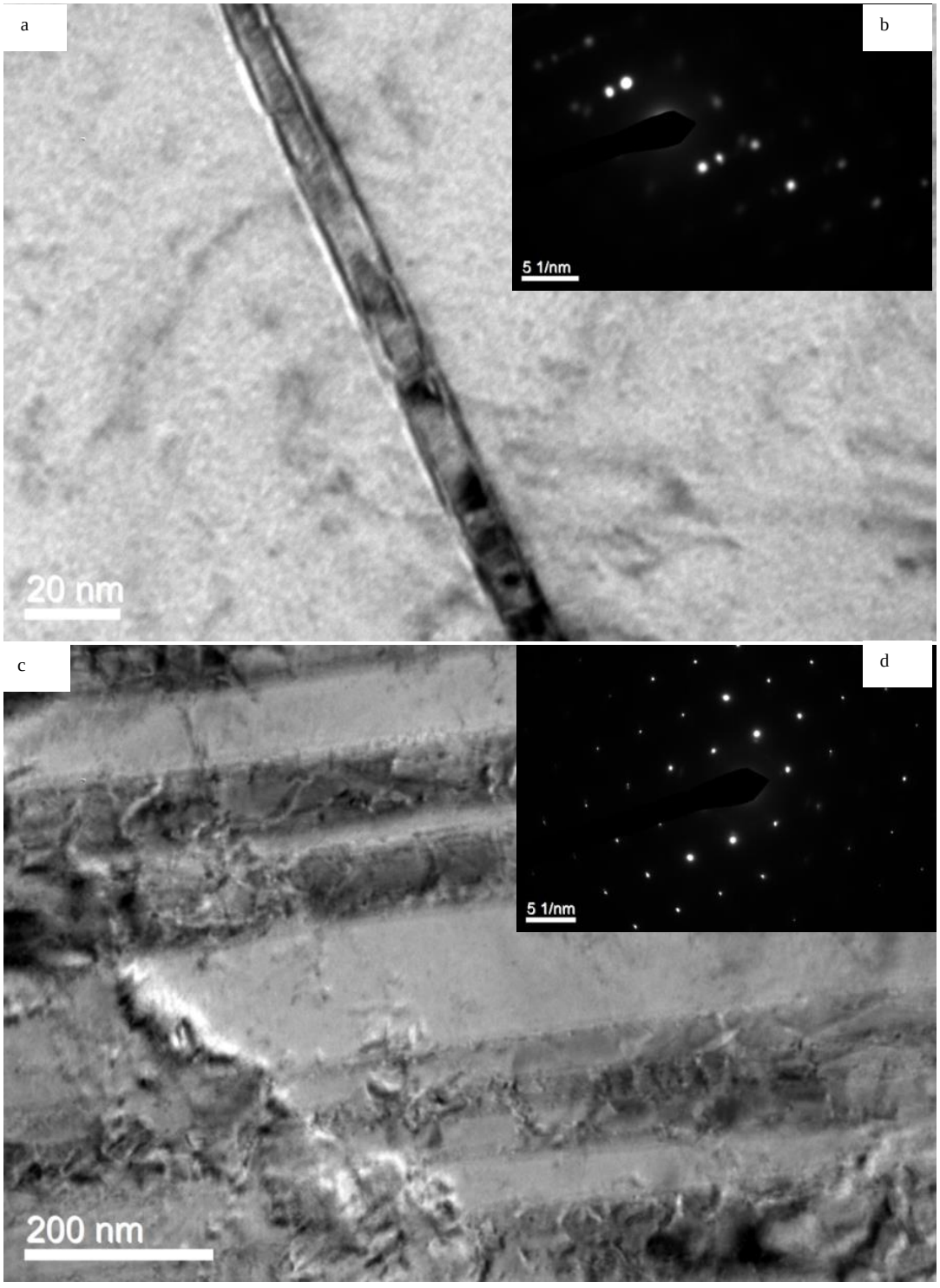

Figure 39- TEM images of 20% deformed 316 [111] single crystal samples

Another TEM bright field image is provided in Figure 40, and as it can be seen, it shows that these twin bands, or at least some of them, are made of multiple, nano-sized twin bands. The fringe form of these nano-twin bands suggests that they are incoherent twin boundaries, which may be further confirmed with the EBSD results; regarding the shape of the boundaries and their orientation.

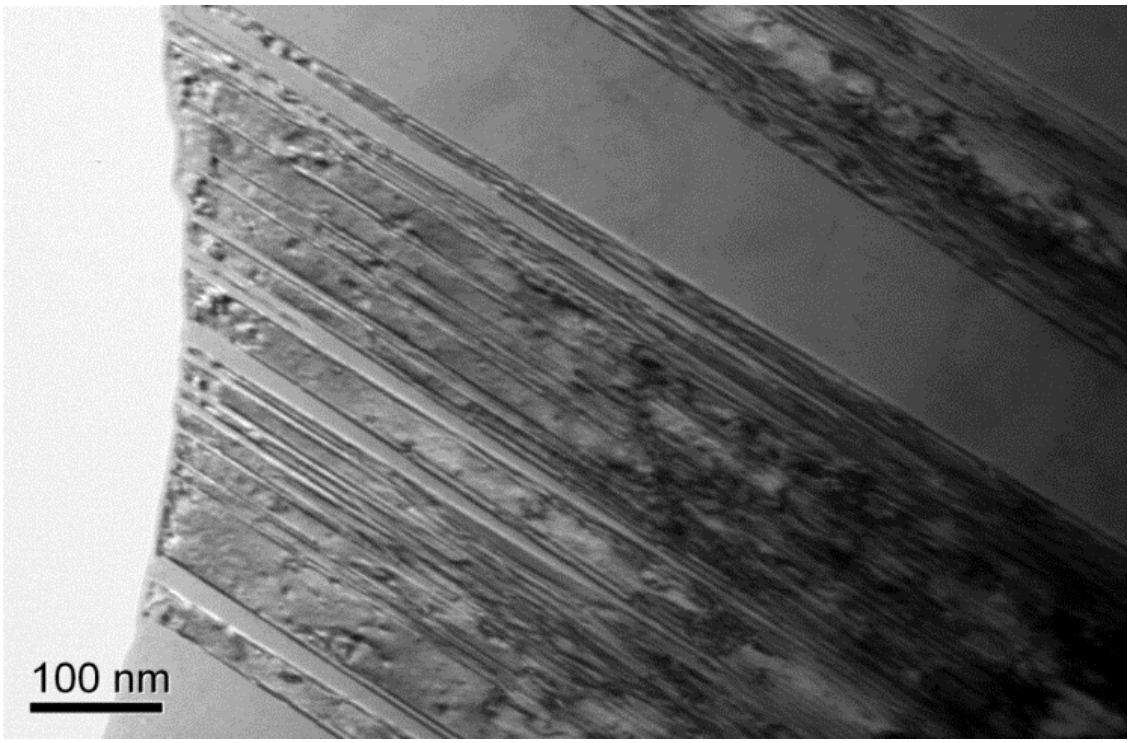

Figure 40- bright field TEM image of 316 [111] single crystal deformed 20% at room

Single crystalline bone-shaped sample were also prepared from the same stainless steel 316, only with [110] orientations. Optical microscopy of the surface (**Error! Not a valid bookmark self-reference.**-a) revealed the presence of a precipitated phase, as was the case for [111] single crystals. Heat treating the samples at 1200°C for 1 hour didn't eliminate the precipitate; however, it had the effect of slightly shrinking the precipitates (**Error! Not a valid bookmark self-reference.**-b), suggesting that the precipitate may possibly be dissolved at higher temperatures or longer times.

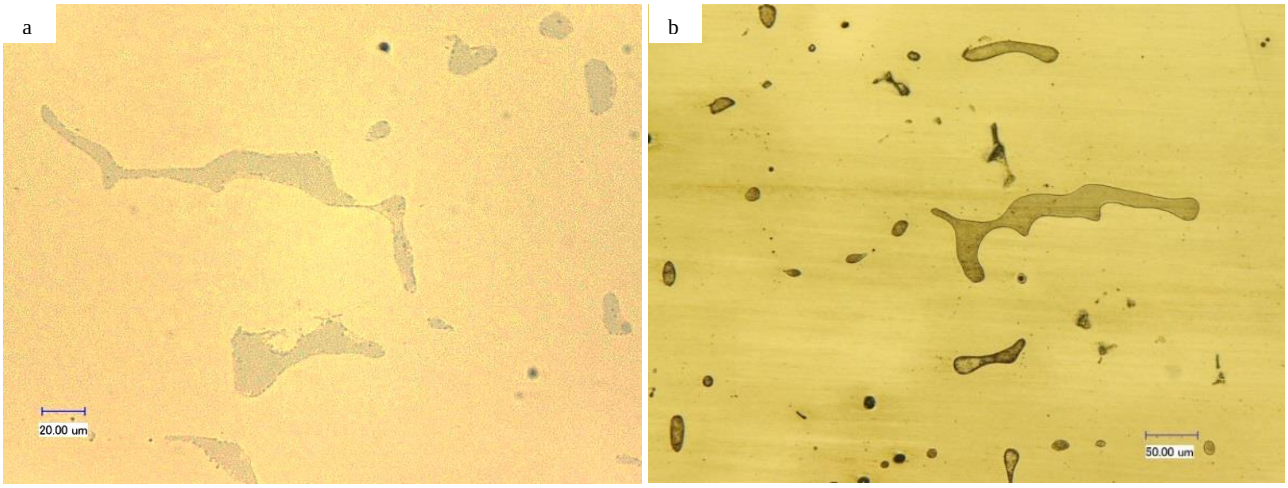

Figure 41- OM images of 316 [110] single crystal a) as received and b) after heat treating at 1200°C for 1 hour and subsequent water quenching

316 [110] single crystalline samples were then deformed 10% using uniaxial tension test at room temperature and -80°C (Figure 42). As expected, decreasing the temperature increased the yield stress of the material. Moreover, surface features that appear on the surface after the tensile test are far more densely packed and more parallel (Figure 43) than those of 316 [111] single crystal deformed 20% at room temperature.

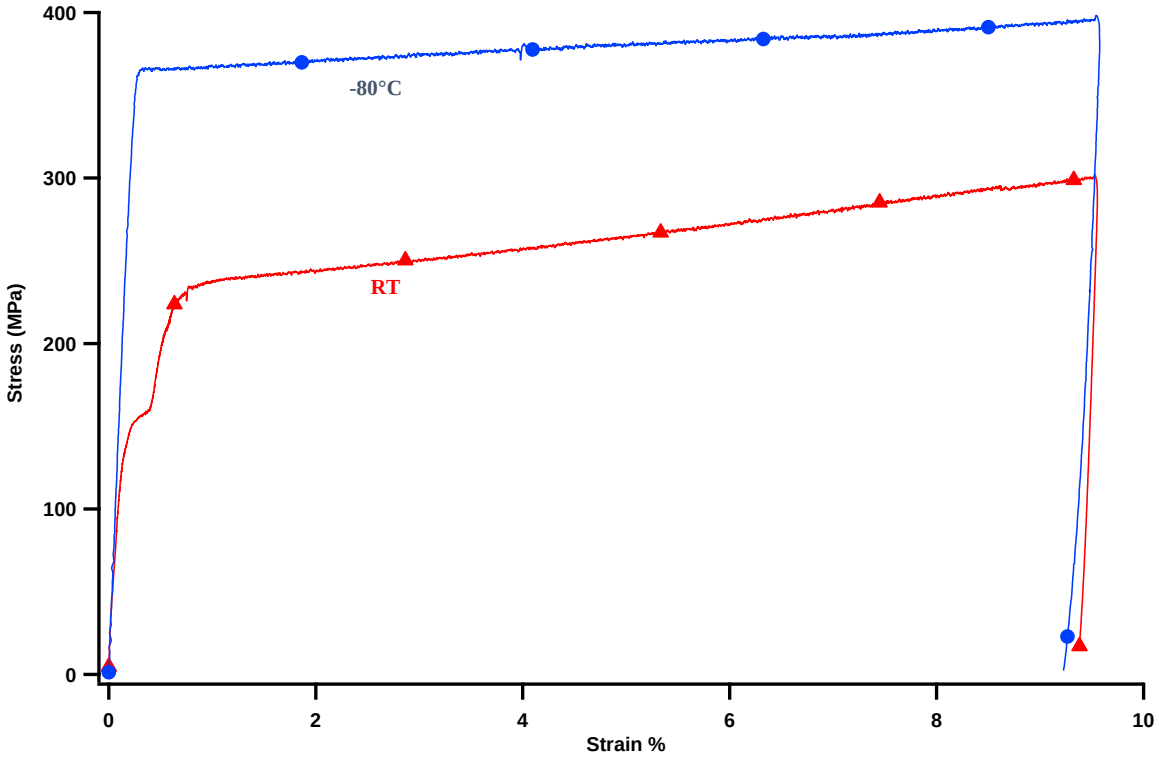

Figure 42- Stress vs. strain curve of 316 [110] single crystalline samples deformed 10% at room temperature and -80°C

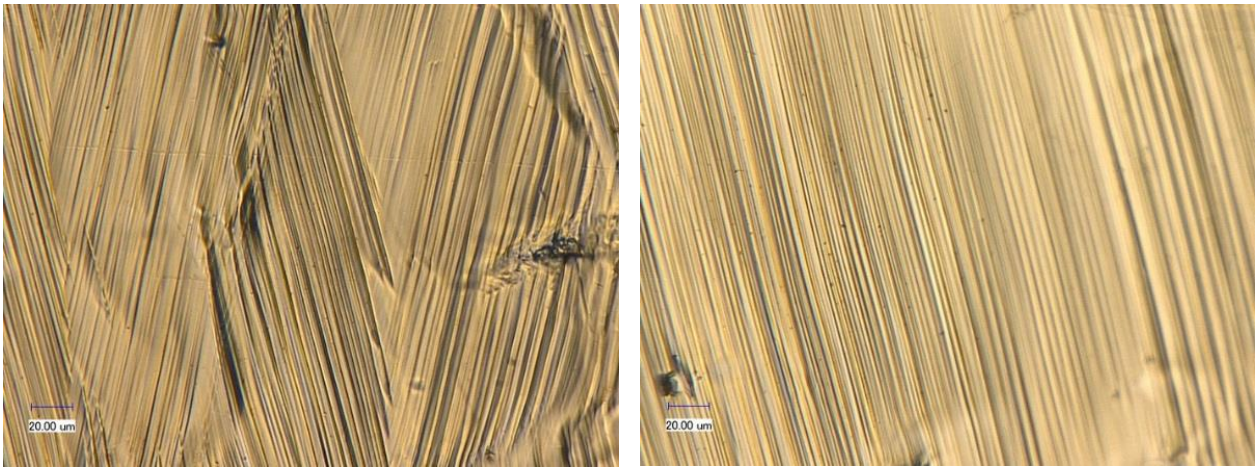

Figure 43- OM images of 316 [110] single crystalline samples deformed 10% at -80°C

Given the ease of access and lower cost of conventional, poly crystalline 316 SS, samples out of a polycrystalline bar of 316 SS were prepared and studied. A number of samples were then used for uniaxial tension test, with different displacement rates, up to a strain of 10% at room temperature. As it can be seen from the curves (Figure 44), the work hardening exponent is independent of the displacement rate, suggesting that the major deformation mechanism at work is twinning, because twinning is insensitive to the displacement rate. Figure 45 shows the optical microscopy image of the sample surface after the tensile test. Parallel lines of surface features can be seen, with different orientations in each grain, due to the plastic deformation.

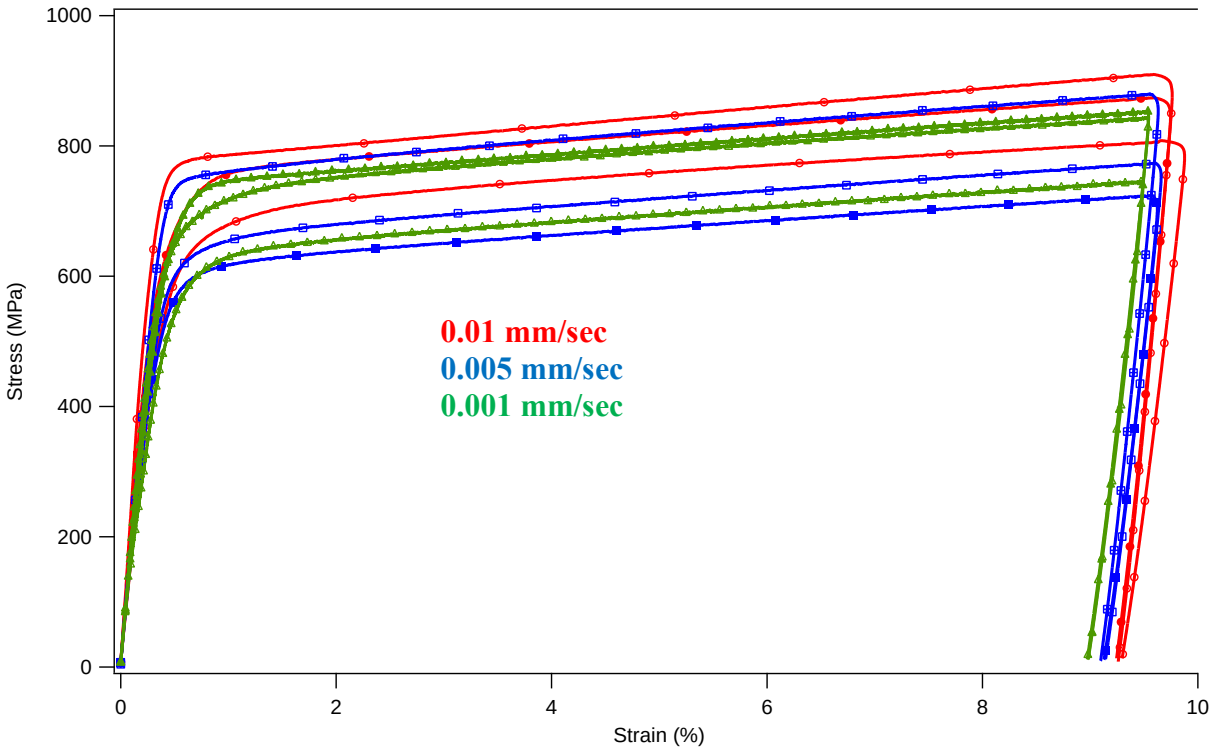

Figure 44- Stress vs. strain curves of stainless steel 316 polycrystalline samples under uniaxial tension test at room temperature with different displacement rates

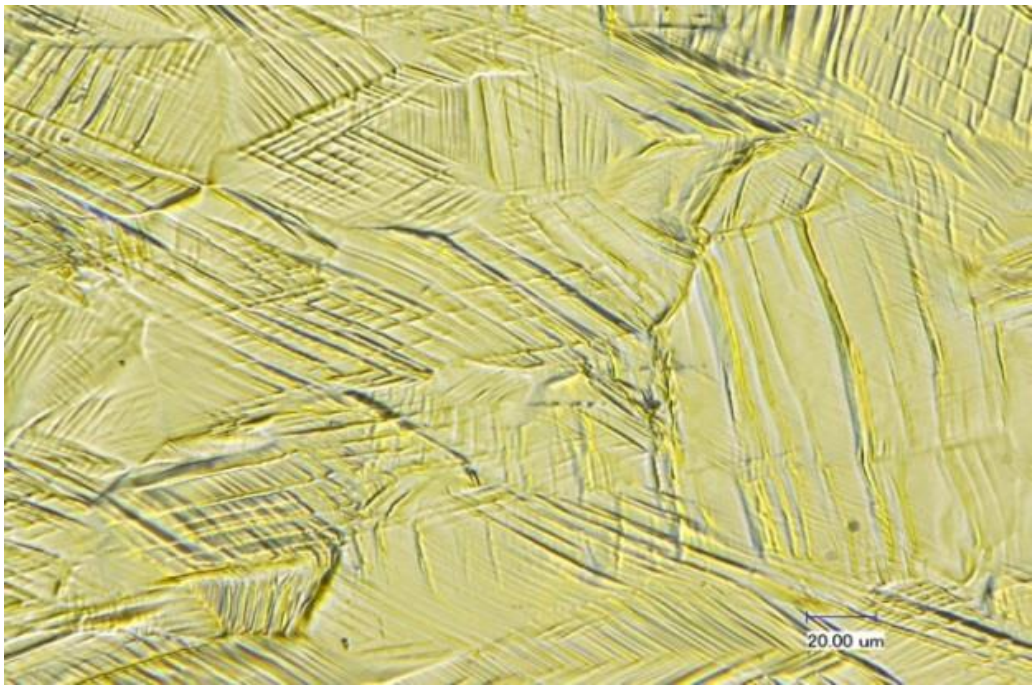

Figure 45- OM of the sample after 10% elongation at room temperature with displacement rate 0.01 mm/sec

Samples were then polished and prepared for Electron Backscatter Diffraction analysis, and the orientation map obtained is shown in Figure 46. However, it can be seen that very little, if any, deformation twinning can be detected. The reason is that, unlike the case of the single crystals, most of the grains are oriented in a way which is not favorable for deformation twinning to happen.

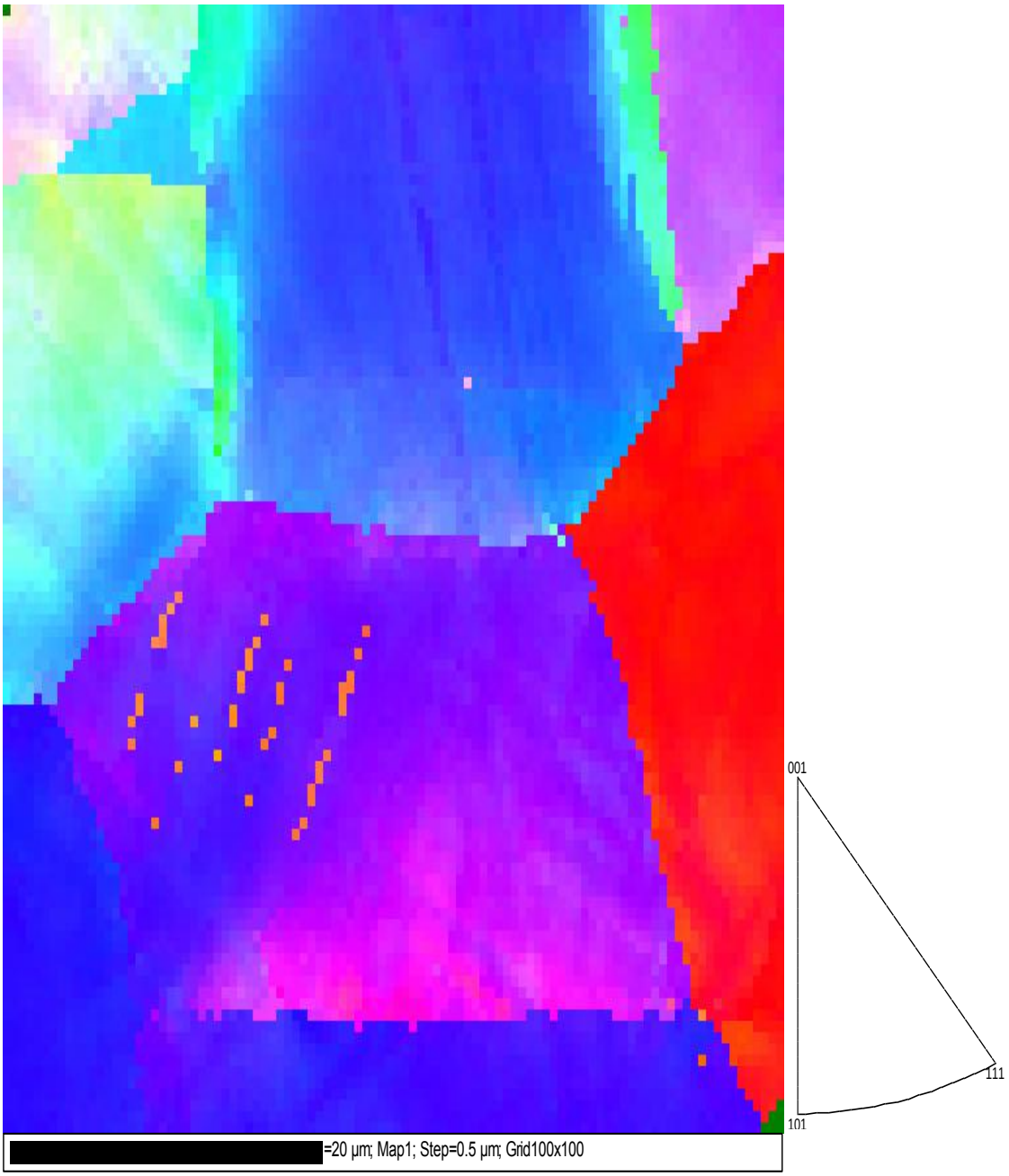

Figure 46- EBSD map of stainless steel 316 polycrystalline sample after tension test to 10% elongation at room temperature with displacement rate of 0.01 mm/sec

Upon a closer look using EBSD (i.e. smaller step sizes), it is revealed (Figure 47-a) that in the grains that have orientations close to [111], features that appear to be deformation twining exist. The orientation of these features, as shown in Figure 47-b, is close to that of the deformation twinning already reported for the single crystals. The misorientation angle (Figure 47-c) confirms that this 1.5 µm feature is in fact a twinning, with an angle of 60˚ with respect to the original grain. The size of this detected twinning suggests that there might be twin bands too small to be detected in Figure 46.

To practice, verify, and improve this technique, stainless steel 316 polycrystalline samples were deformed 10% at room temperature and then marked using Electric Discharge Machining (EDM) cutting to create a notch. The EBSD map is presented in Figure 48. Twin bands, almost 1.5µm wide, are observed and confirmed with measuring the misorientation angle (Figure 48-b).

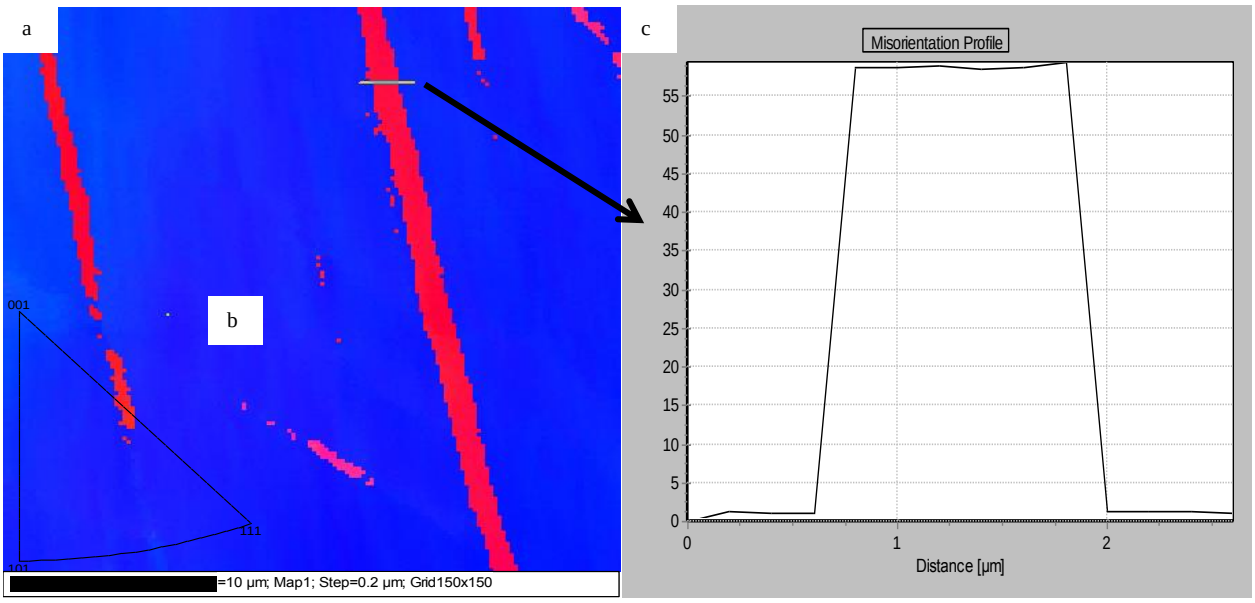

Figure 47- a) EBSD map with smaller step size of stainless steel 316 polycrystalline sample after tension test to 10% elongation at room temperature with displacement rate of 0.01 mm/sec, b) EBSD legend, c) Misorientation profile of the specified band

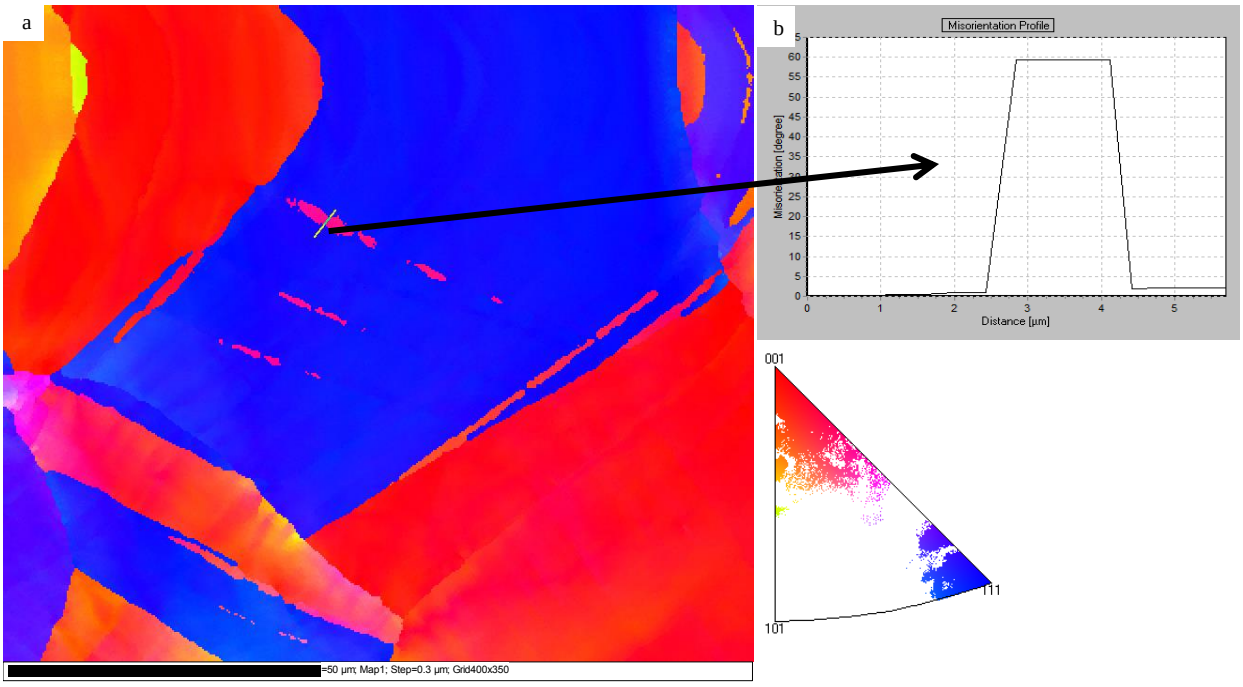

Figure 48- a) EBSD map next to marker of stainless steel 316 polycrystalline sample after tension test to 10% elongation at room temperature with displacement rate of 0.01 mm/sec, b) Misorientation profile of the specified band

Based on the microhardness tests previously performed on the deformed stainless steel 316N samples before and after heat treating for different temperatures (Figure 49), a temperature range of 250˚C to 650˚C with 50˚C intervals is suggested. In order to challenge the capability of this technique of marking the samples using EDM for EBSD after heat treatment, the sample described in previous paragraph was heat treated at 750˚C for 1 hour and then water quenched. The obtained EBSD map (Figure 50) indicates massive recrystallization and growth such that only the grain from the bottom right corner is recognizable from the pre-heat treatment EBSD map, and the rest of the map is mostly consisted of another large grain. This data shows that the 750˚C heat treatment has been too high, as expected, but the technique is valid even in a temperature higher than the required range.

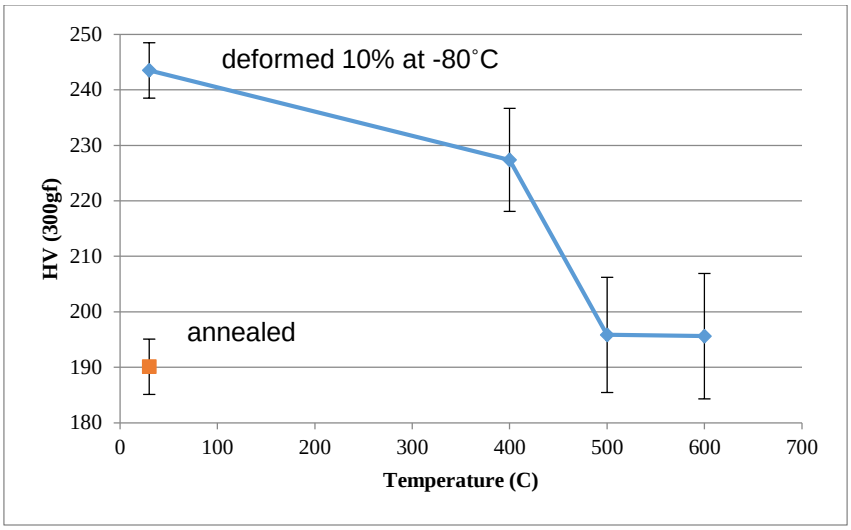

Figure 49- Microhardness profile of stainless steel 316N as a function of heat treating temperature

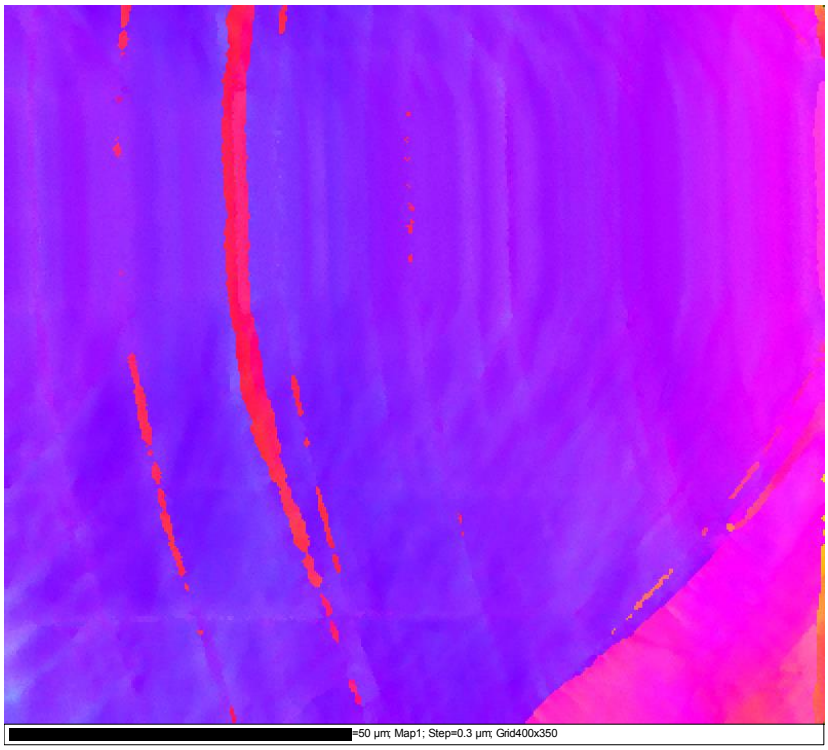

Figure 50- EBSD map next to marker of stainless steel 316 polycrystalline sample after tension test to 10% elongation at room temperature with displacement rate of 0.01 mm/sec, heat treated at 750˚C for 1 hour then water quenched

In order to acquire a better understanding of the twin stability at higher temperatures, the stress-strain responses of the samples were studied up to failure. Three set of samples were prepared for further study with tensile elongations of 10%, 20%, and till-failure (Figure 51). Samples deformed to 20% strain were studied using Transmission Electron Microscopy (TEM). The TEM Bright Field (BF) images (Figure 52-a) show two twin bands. The Selected Area Diffraction Patterns

(SADP) obtained from this region Figure 52-b and c) confirm that these observed features are indeed deformation twins. From the Dark Field (DF) images, shown in Figure 52-d and e, twin bands can be clearly seen. Most of the deformation twins are in the nanoscale. These images suggest that the twin bands, formerly observed using Electron Backscattering Diffraction (EBSD) microscopy to be a couple of micrometers, are in fact made up from a "bundle" of much smaller twins (nano-twins). Furthermore, from these images, twins form in different twinning planes. Usually, a twin bundle on a given twin plane stops as soon as it meets another twin bundle from another system. This phenomena, combined with the fact that the twins are a bundle of smaller twins, may lead to improved mechanical properties. Another observable fact from Figure 52-a is the presence of dislocations around the twins in the matrix, as well as within each bundle among the smaller twins.

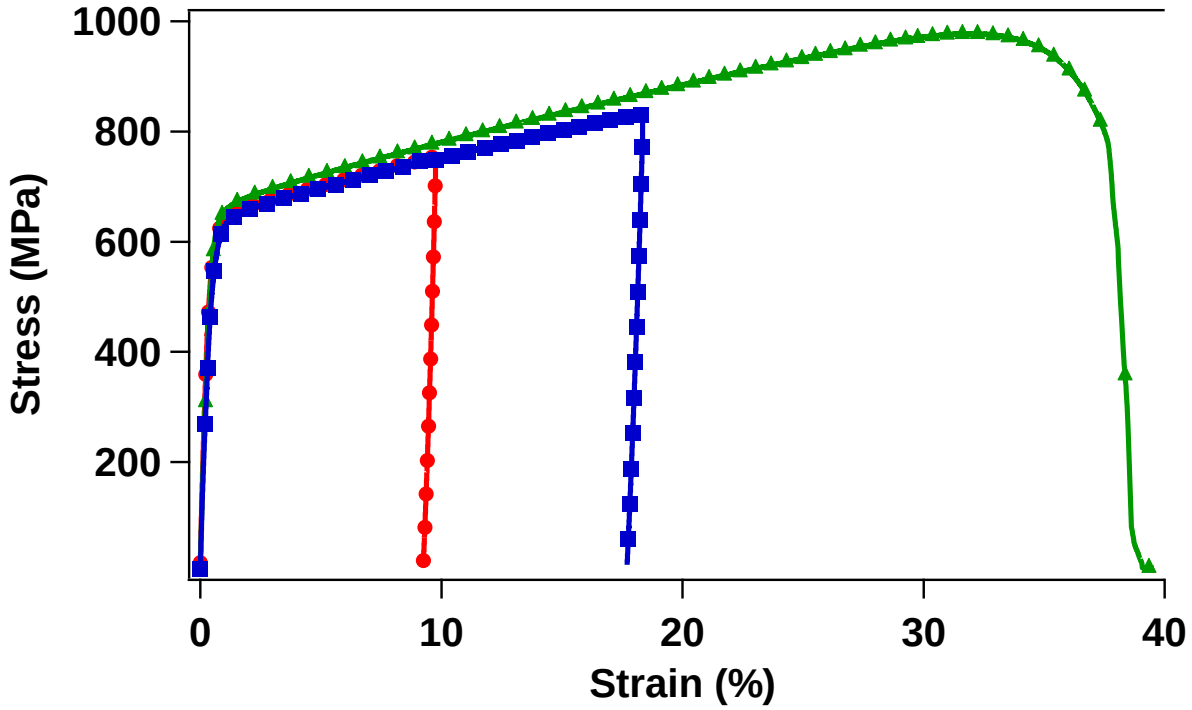

Figure 51- Stress-strain behavior of 316 stainless steel with elongations of 10%, 20%, and till-failure in uniaxial tension test at room temperature

Next, samples were heated in-situ inside TEM. The TEM images (Figure 53 to Figure 61) suggest that upon heating the samples, deformation twins are very stable up to 1000˚C. In elevated temperatures, however, material loss is observed due to electron bombardment of the sample.

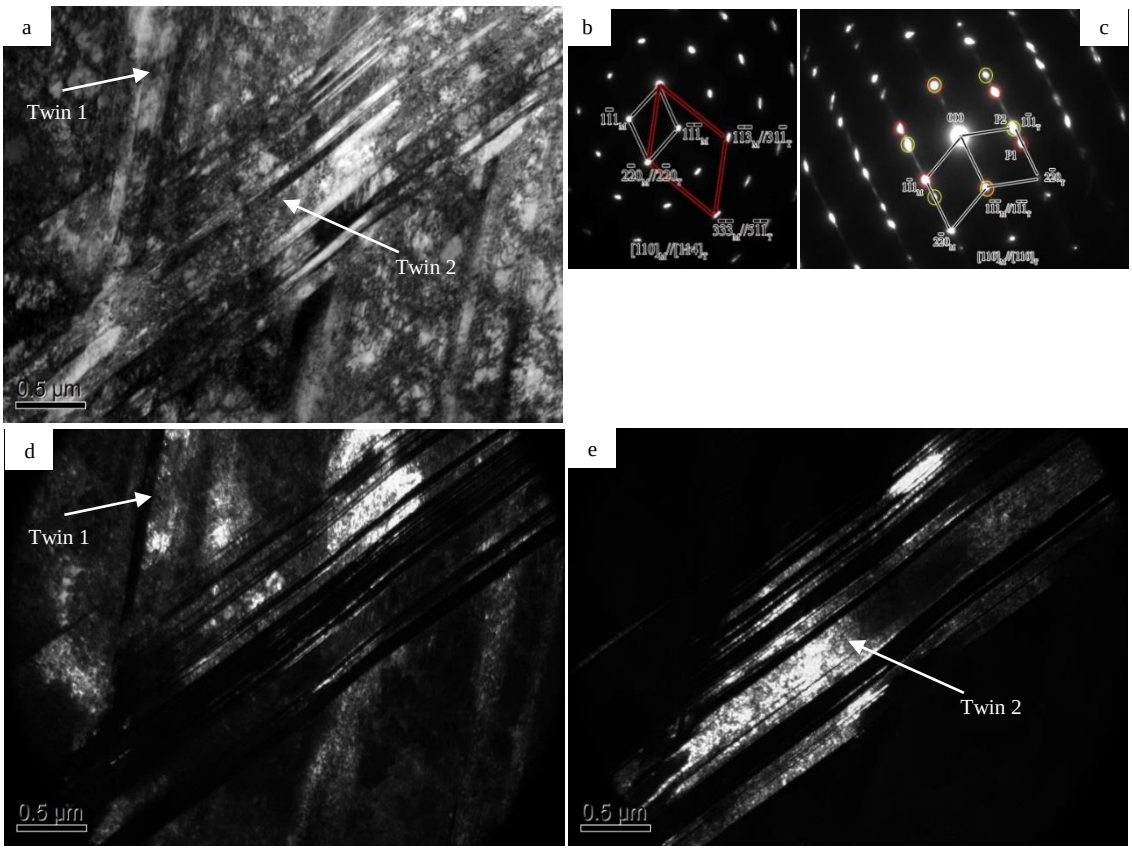

Figure 52- TEM images of 316 stainless steel deformed to 20% strain in a tensile test at room temperature, a) BF image of two twin bands formed from bundles, b) SADP of twin 1 and the matrix, c) SADP of twin 2 and the matrix, d) DF image of matrix, e) DF image of twin 2

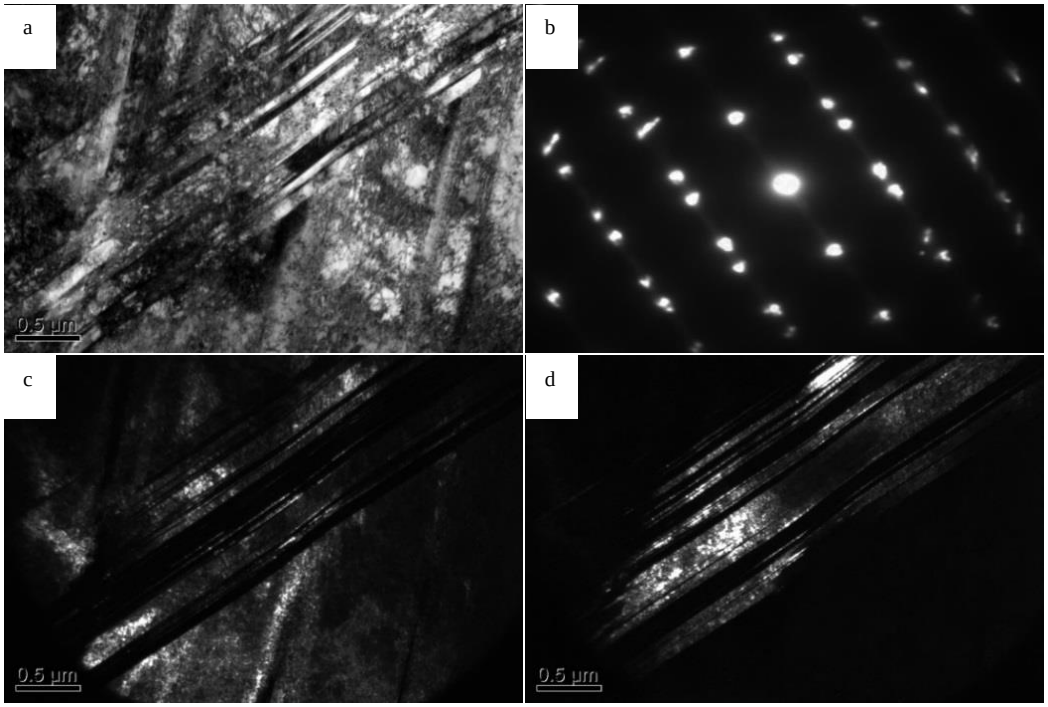

Figure 53- TEM images of 316 stainless steel deformed to 20% strain in a tensile test at room temperature then heated to 220˚C, a) BF image of twin bands, b) SADP of twin and matrix, c) DF image of matrix, d) DF image of twin

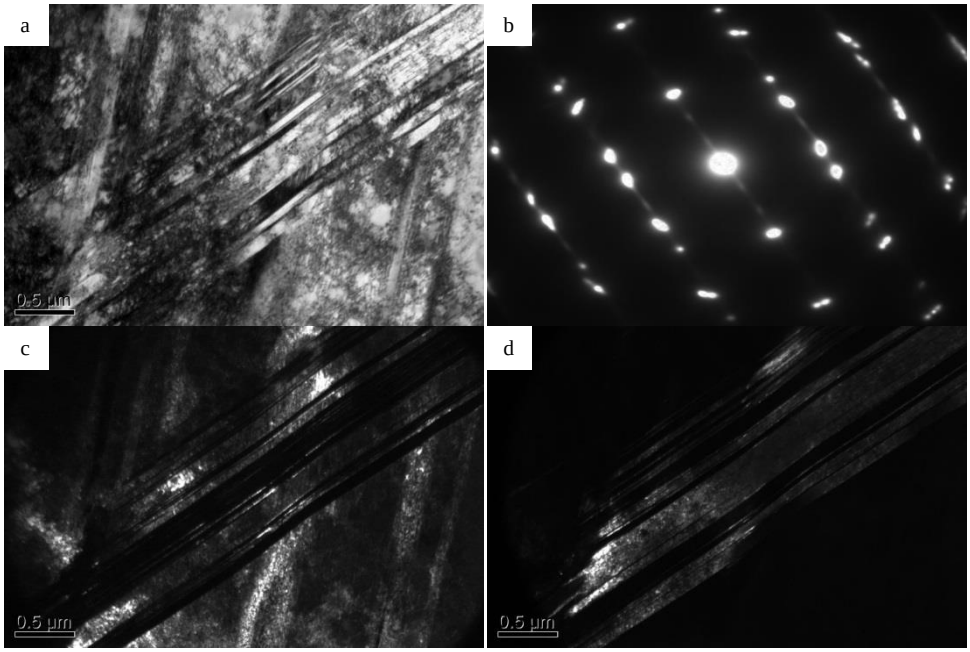

Figure 54- TEM images of 316 stainless steel deformed to 20% strain in a tensile test at room temperature then heated to 310˚C, a) BF image of twin bands, b) SADP of twin and matrix, c) DF image of matrix, d) DF image of twin

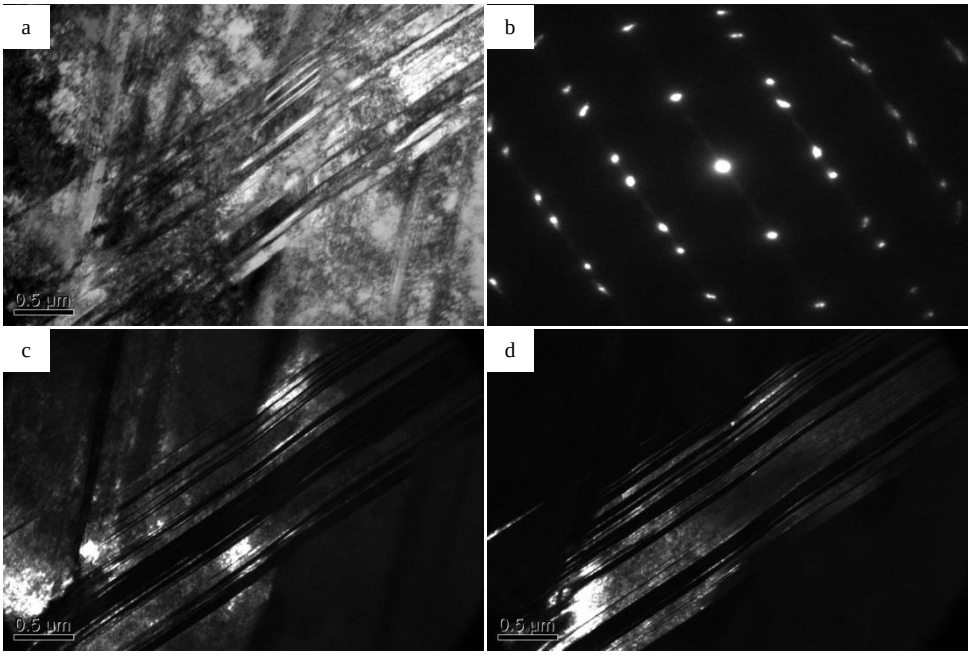

Figure 55- TEM images of 316 stainless steel deformed to 20% strain in a tensile test at room temperature then heated to 415˚C, a) BF image of twin bands, b) SADP of twin and matrix, c) DF image of matrix, d) DF image of twin

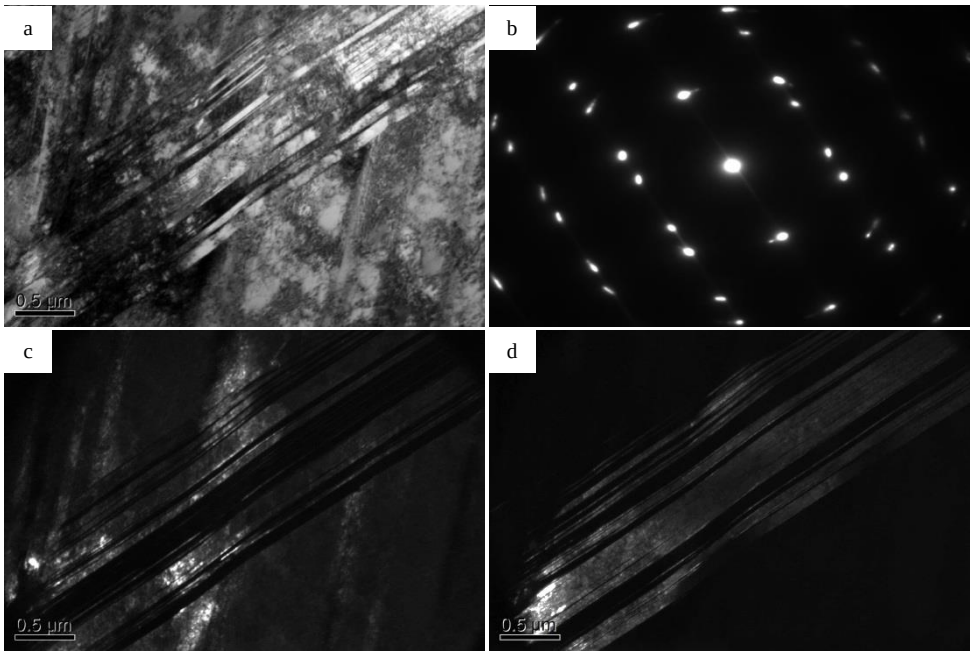

Figure 56- TEM images of 316 stainless steel deformed to 20% strain in a tensile test at room temperature then heated to 520˚C, a) BF image of twin bands, b) SADP of twin and matrix, c) DF image of matrix, d) DF image of twin

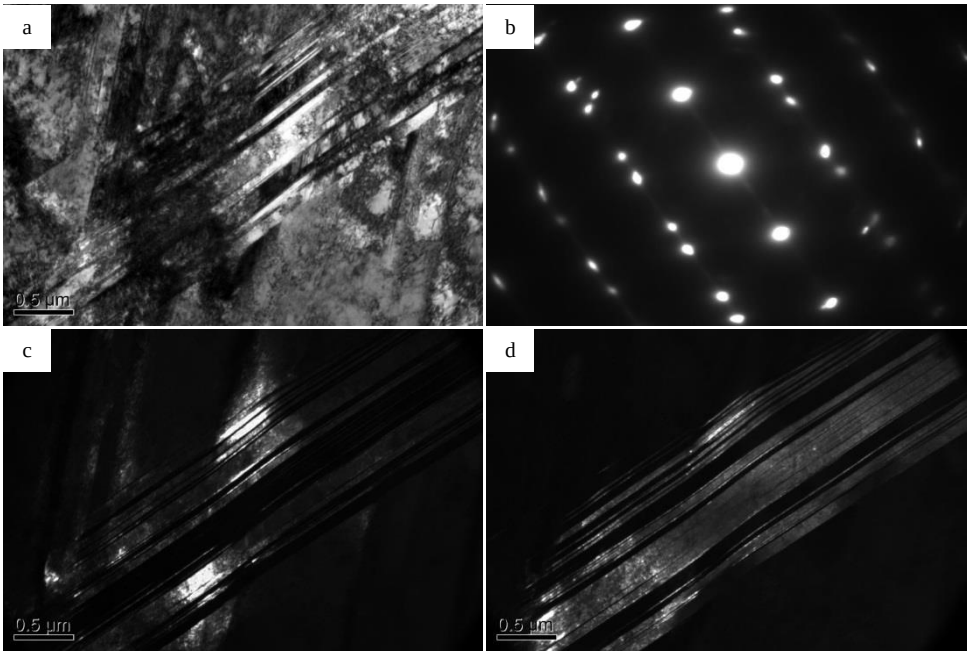

Figure 57- TEM images of 316 stainless steel deformed to 20% strain in a tensile test at room temperature then heated to 600˚C, a) BF image of twin bands, b) SADP of twin and matrix, c) DF image of matrix, d) DF image of twin

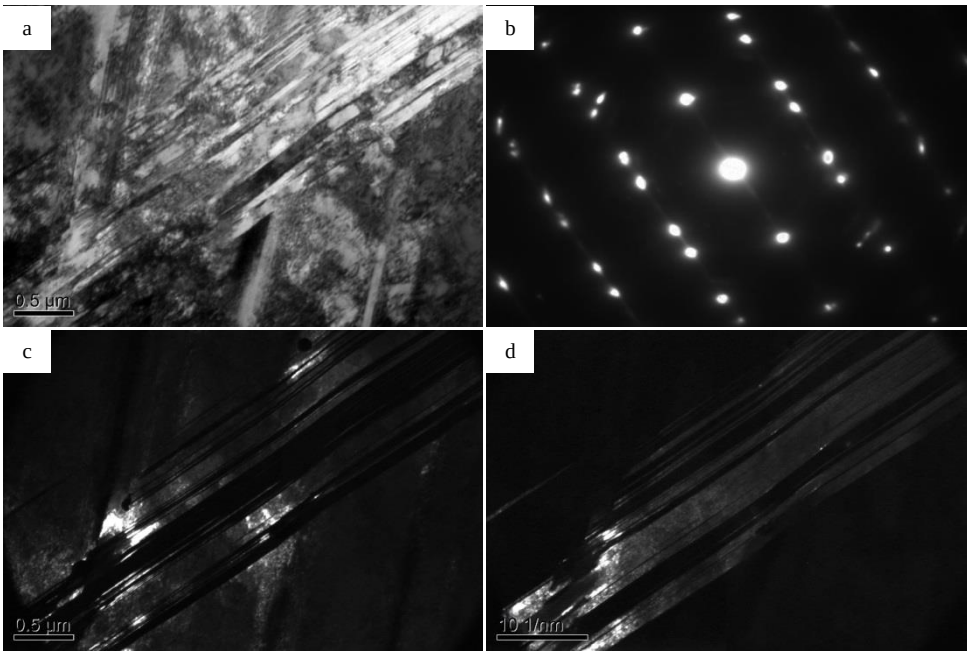

Figure 58- TEM images of 316 stainless steel deformed to 20% strain in a tensile test at room temperature then heated to 700˚C, a) BF image of twin bands, b) SADP of twin and matrix, c) DF image of matrix, d) DF image of twin

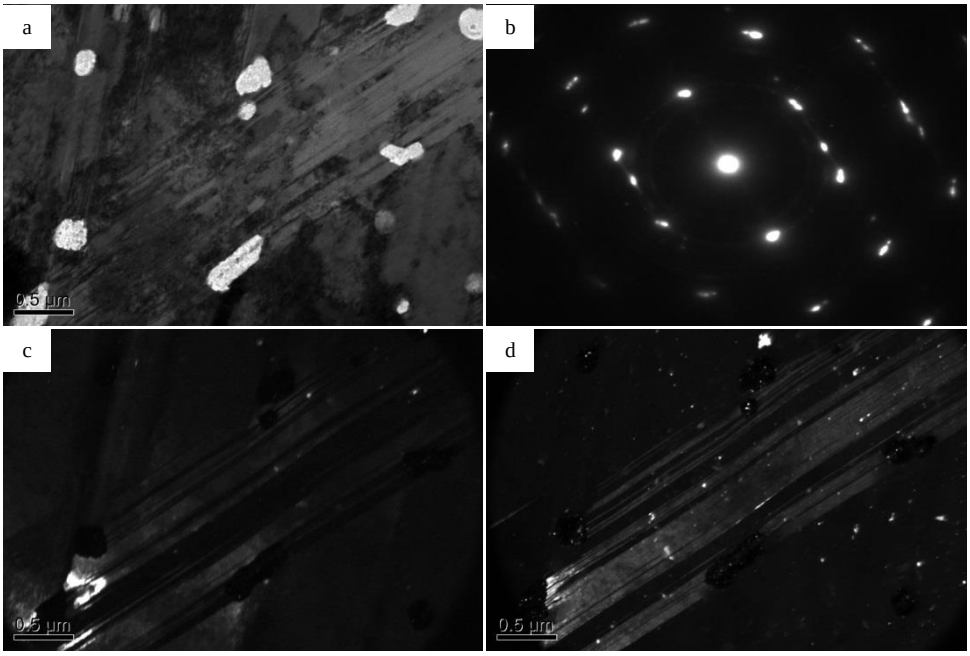

Figure 59- TEM images of 316 stainless steel deformed to 20% strain in a tensile test at room temperature then heated to 800˚C, a) BF image of twin bands, b) SADP of twin and matrix, c) DF image of matrix, d) DF image of twin

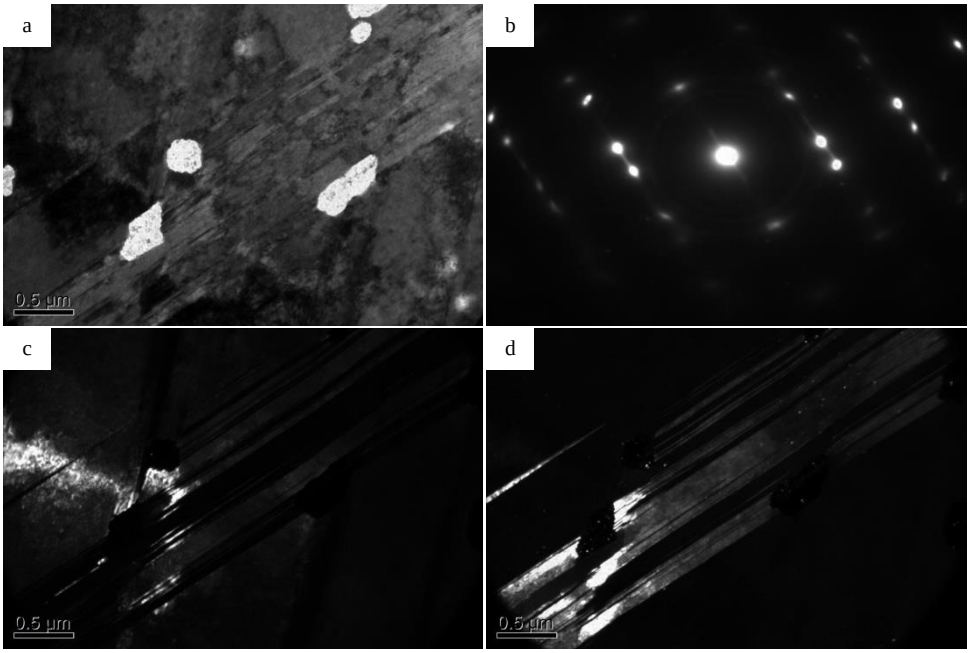

Figure 60- TEM images of 316 stainless steel deformed to 20% strain in a tensile test at room temperature then heated to 900˚C, a) BF image of twin bands, b) SADP of twin and matrix, c) DF image of matrix, d) DF image of twin

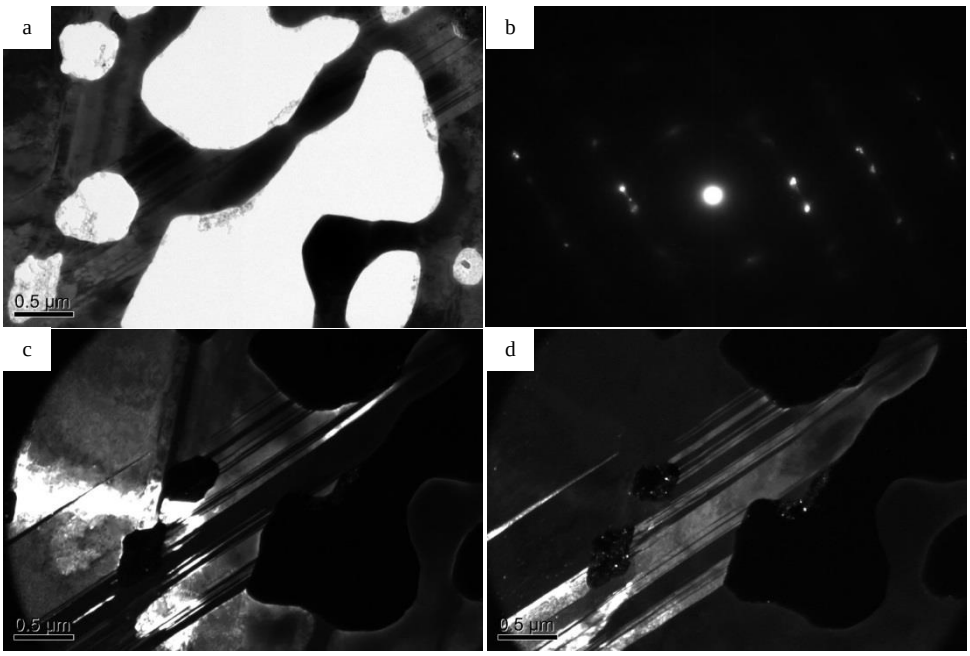

Figure 61- TEM images of 316 stainless steel deformed to 20% strain in a tensile test at room temperature then heated to 1000˚C, a) BF image of twin bands, b) SADP of twin and matrix, c) DF image of matrix, d) DF image of twin

In order to avoid, or at least minimize, the damage from electron bombardment, another sample of stainless steel 316 deformed to 20% strain uniaxially at room temperature was prepared for TEM and was then directly heated in-situ to 1000˚C. The acquired BF image (Figure 62) shows less material loss due to electron bombardment, however, deformation twins still exist in the structure, indicating their superior thermal stability.

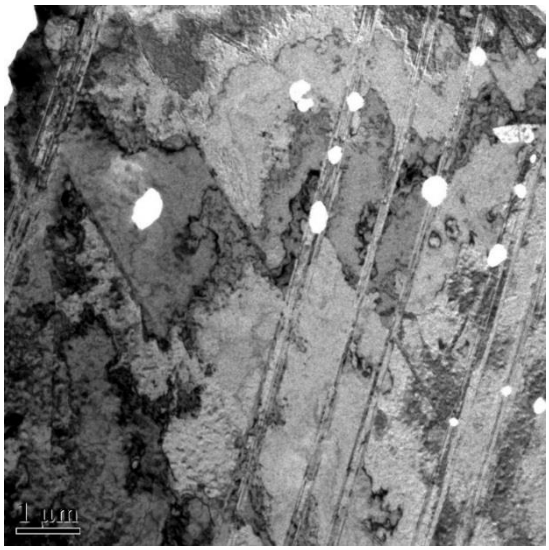

Figure 62- TEM BF images of 316 stainless steel deformed to 20% strain in a tensile test at room temperature then heated to 1000˚C

To better evaluate the baseline starting materials behavior, the "as-received" samples were investigated. The stainless steel 316 sample, in its as-received condition, was prepared for Optical Microscopy (OM). The OM images (*Figure* 63-top) show an average grain size of about 67μm. The other observable features are band-like structures in some of the grains, suspected to be twin bands. In order to confirm this, the samples were prepared for TEM. The microstructures are shown in *Figure* 63-bottom. These images show there are indeed lots of dislocations and some deformation twins in the as-received material, which is consistent with the OM results.

Since the as-received condition isn't desirable due to uncontrolled existence of deformation twins, a set of heat treatments were done on the as-received sample with the goal of complete recovery of the deformation microstructure. First, samples were individually sealed in quartz tubes in vacuum condition and heat treated at 800, 900, 1000 and 1200˚C for 1 hour and then rapidly water-quenched. A subsequent harness measurement yield the Vickers's hardness values to be 214.6 ± 4.9, 188.2 ± 5.8, 151.5 ± 4.6 and 138.0 ± 2.0, respectively. The hardness of the as-received sample had already been measured to be 256±3. Then, OM samples were prepared as previously mentioned, and OM images were acquired. The OM images (Figure 64) show that heat treating the sample at 1000 and 1200˚C can almost completely get rid of the features that show up after etching. However, a grain size measurement (Figure 65) reveals that heat treating at 1200 ˚C may cause an undesirable grain growth.

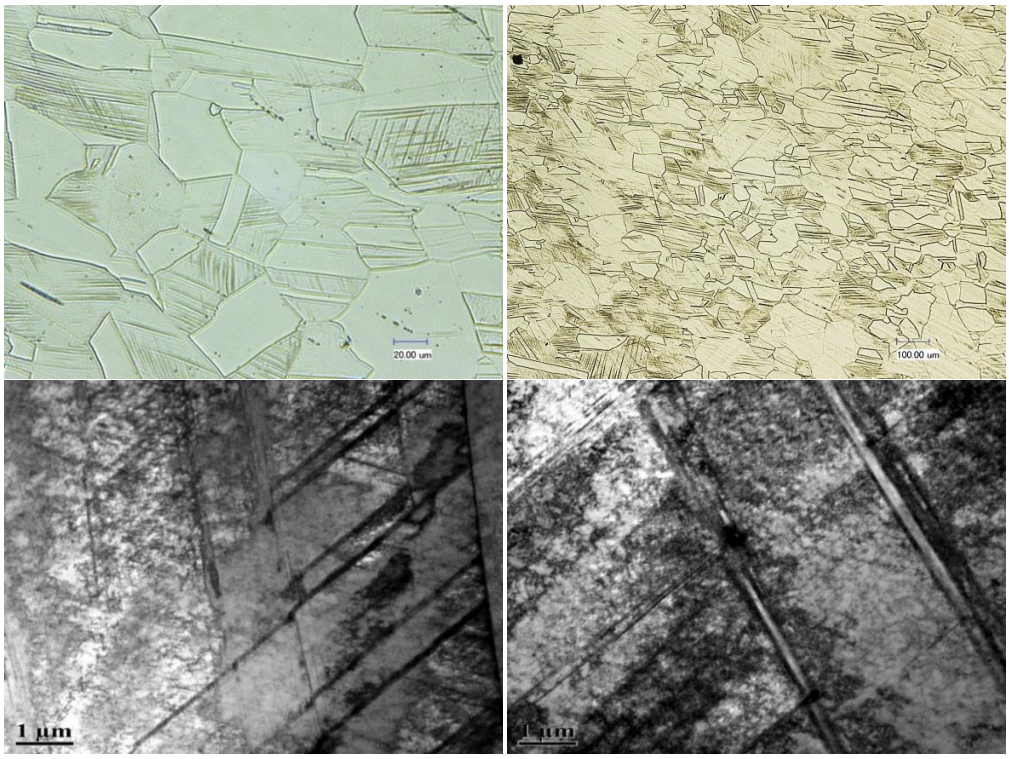

Figure 63- 316 Stainless steel in as-received condition, top) OM, bottom) TEM

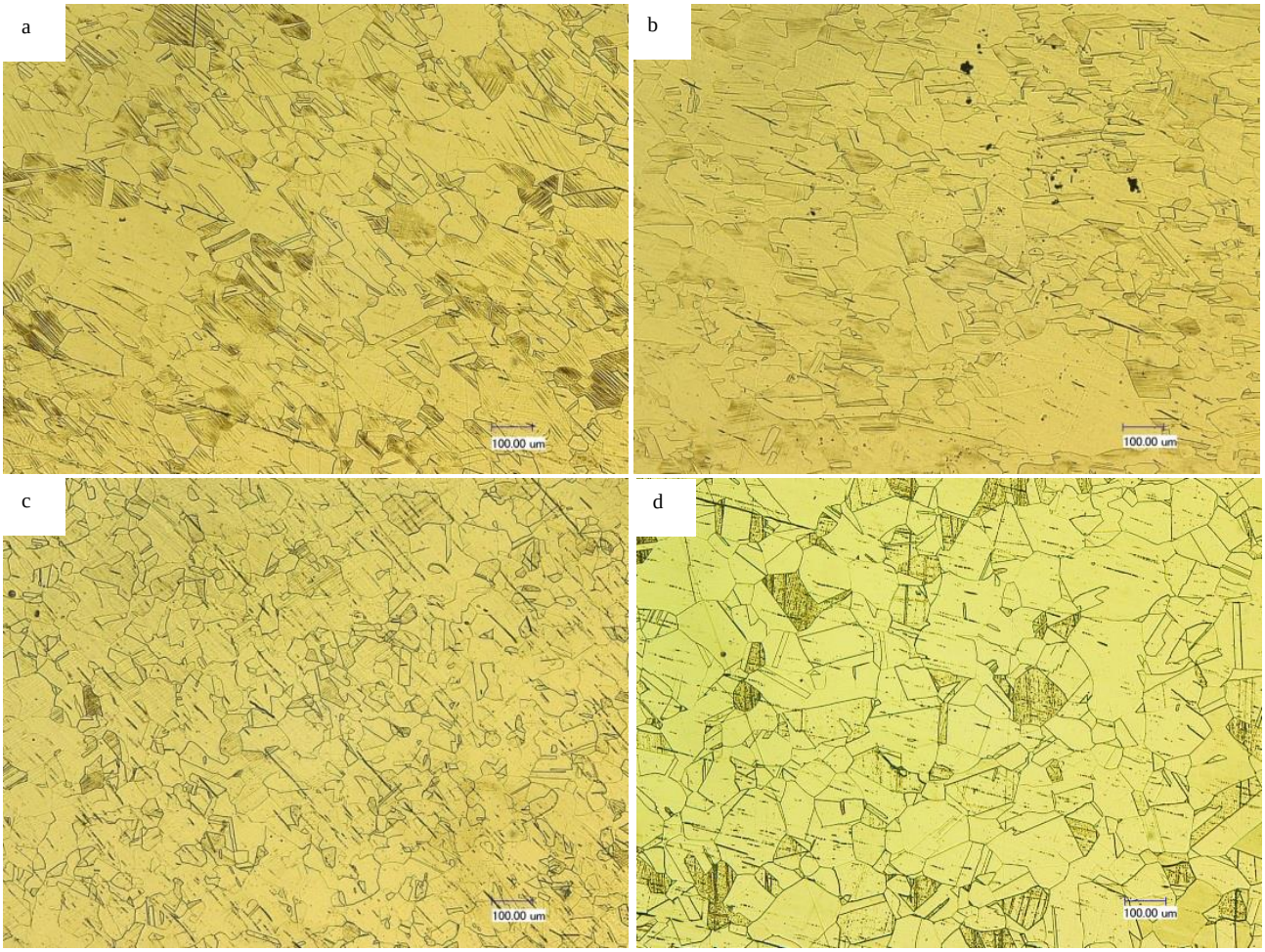

Figure 64- OM images of 316 stainless steel as-received samples heat treated at a) 800, b) 900, c) 1000, and d) 1200˚C for 1 hour and then water quenched

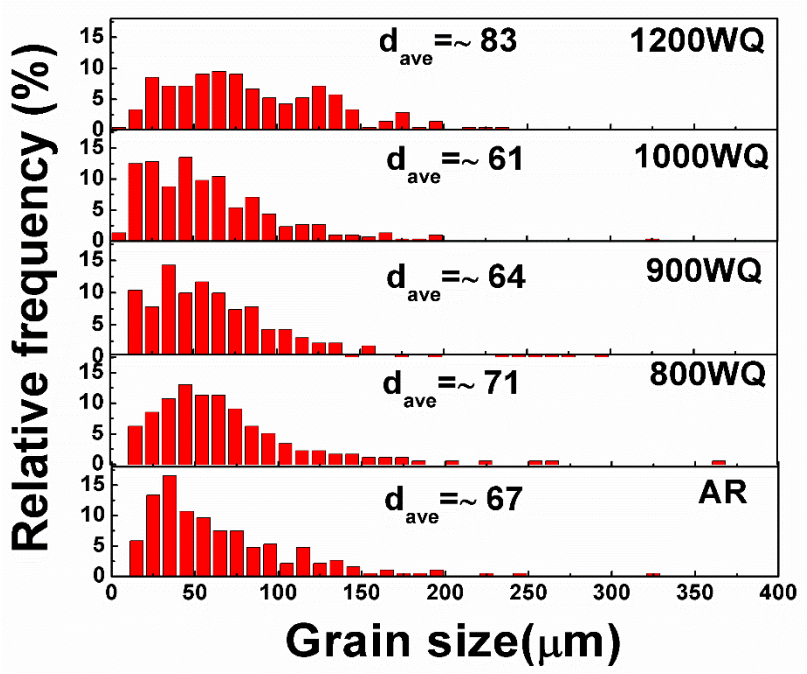

Figure 65- Grain size measurement of 316 stainless steel samples heat treated at different temperatures for 1 hour

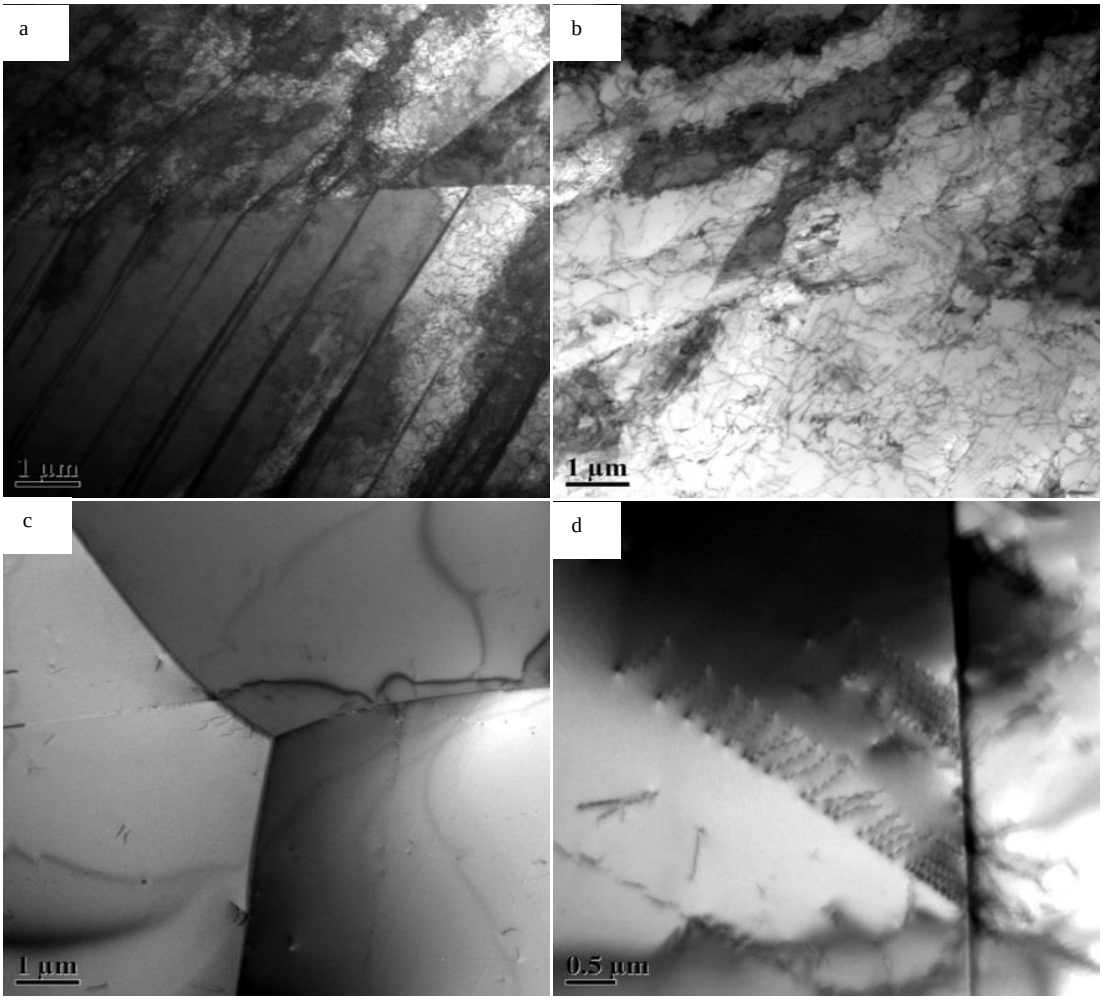

Figure 66- TEM BF images of stainless steel 316 as-received samples heat treated at a) 800, b) 900, c) 1000, and d) 1200˚C for 1 hour and then water quenched

A more detailed study was performed using TEM, and the BF images (Figure 66) reveal that twins still exist after 800˚C annealing which can explain why the hardness of 800˚C annealed samples are as high as 214.6 ± 4.9. Twins are somewhat eliminated in 900˚C annealed materials, but dislocations are still here. Furthermore, it can be seen that twins and dislocations are totally recovered after 1000 ˚C and 1200 ˚C annealing, showing that heat treating at 1000˚C can recover the materials microstructure. As a result, all samples were annealed at 1000˚C, and investigation continued on the samples annealed at this temperature. Figure 67 shows the stress-strain behavior of the annealed steel in comparison with the as-received condition. The significant elongation-to-failure indicates a significant degree of recovery in the material. The annealed 316 stainless steel samples that were elongated uniaxially till-failure, were studied using TEM, in two different regions (Figure 68-a): region 1 (closer to the necking area), and region 2 (farther from the necking area). The findings are in agreement with the previous results from the as-received samples, indicating that the twin bundles from different twin system don't cross each other. The presence

of a high density of dislocations in between the twin bundles in the structure, also, indicates the capability of this material to show improved mechanical properties by exploiting its deformation twinning mechanism. Next, 316 stainless steel samples annealed at 1000˚C were uniaxially tensile tested to 10% strain at room temperature. The BF TEM images are presented in Figure 69. Based on this image, many dislocations formed after 10% elongation deformation, but only a small volume fraction of twins was formed. It can be concluded that 10% deformation is not enough to activate extensive twinning behavior.

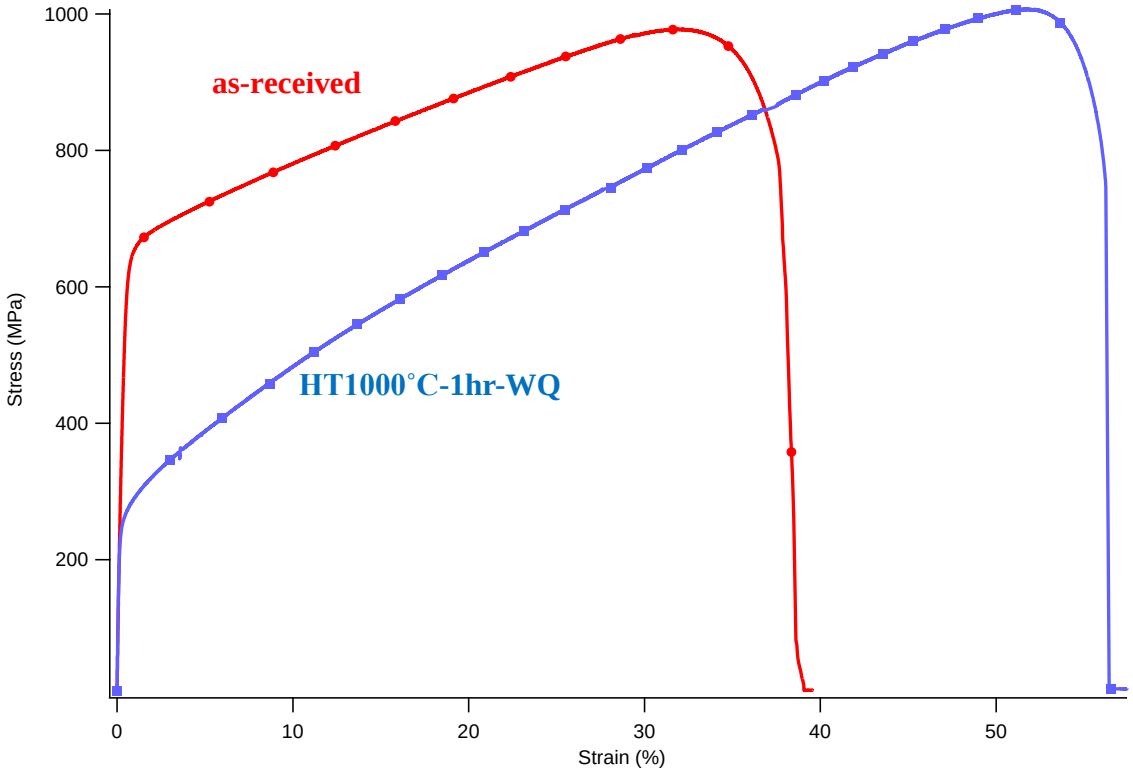

Figure 67- 316 Stainless steel stress-strain behavior, a) as-received, b) annealed at 1000C˚ for 1 hour then water quenched

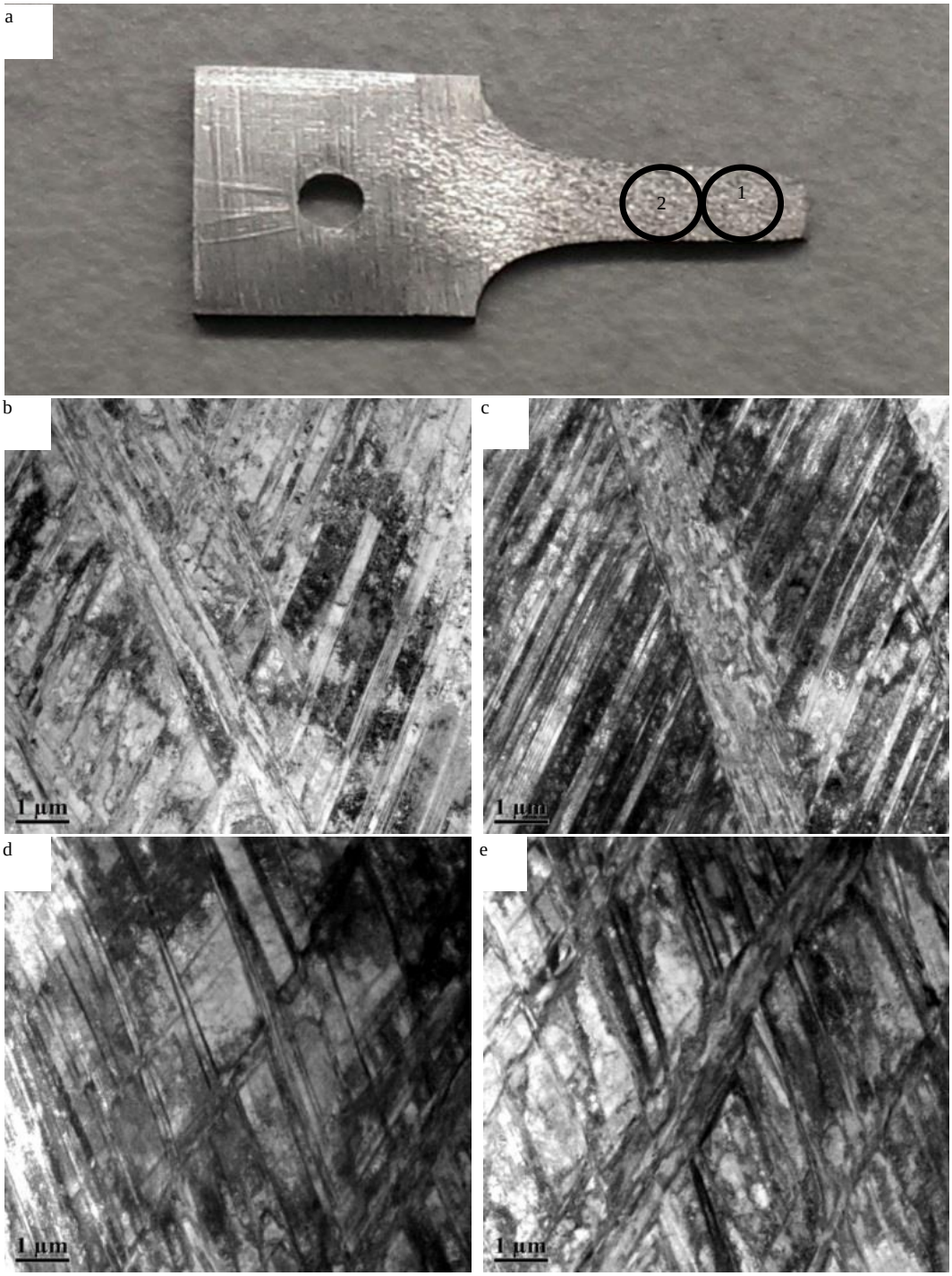

Figure 68- 316 Stainless steel annealed at 1000˚C for 1 hour, uniaxial tension till-failure a) TEM samples cut from two regions, b) and c) TEM BF image of region 1, d) and e) TEM BF images from region 2.

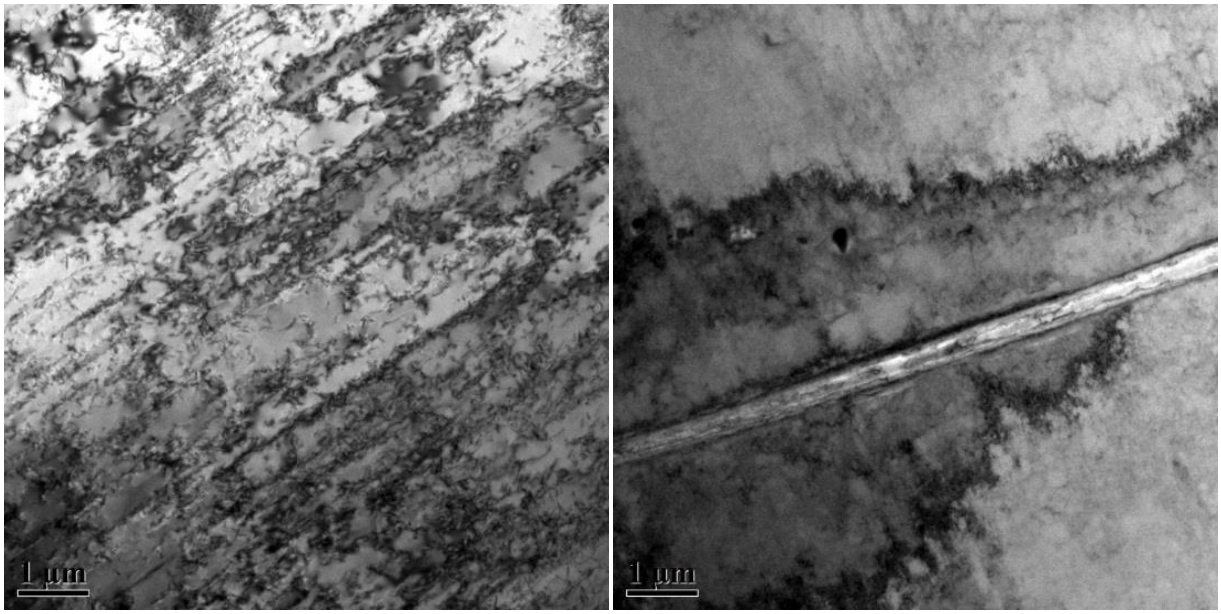

Figure 69- 316 Stainless steel annealed at 1000˚C for 1 hour, uniaxial tension 10% elongation

Next, 316 stainless steel samples, annealed at 1000˚C for 1 hour, were subjected to uniaxial tension test at room temperature to elongations of 20%, 30% and 40% (Figure 70) strains, to study the deformation twinning in different extents of elongation. The samples were then polished and etched as previously stated, and were examined using Scanning Electron Microscope (SEM) and TEM. Figure 71, Figure 72, and Figure 73, show the SEM and TEM images of the samples elongated to 20%, 30% and 40% strains at room temperature, respectively. Comparing the density of twins in the deformed samples to different strains, it can roughly be concluded that as deformation strain increases, the density of twins increases. Moreover, using SEM images, the average density of twins in the 20%, 30% and 40% deformed samples are statistically calculated to be 5.8% ± 1.5%, 9.4% ± 1.6% and 12.5% ± 2.0%, respectively.

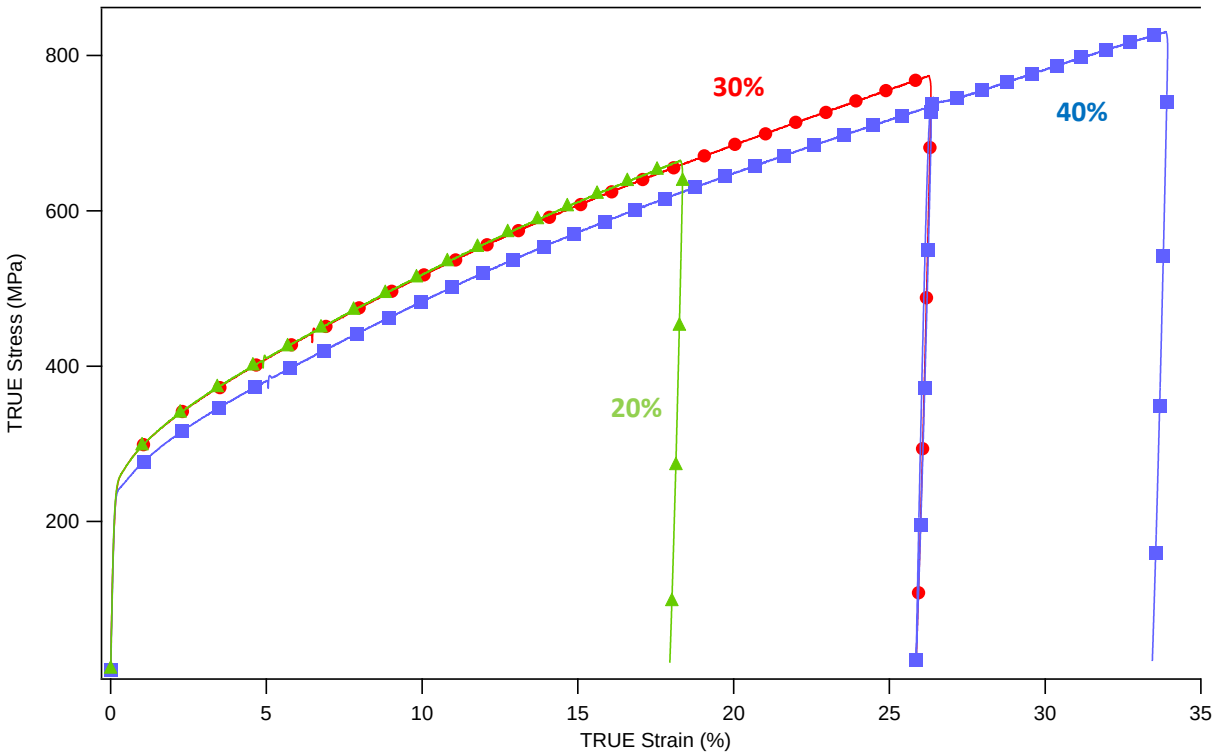

Figure 70- True stress-strain curve of stainless steel 316 samples annealed at 1000˚C for 1 hour, uniaxially elongated to 20%, 30% and 40% at room temperature

To better evaluate the thermal stability of deformation twins, a series of heat treatments on elongated samples were performed: 500˚C, 700˚C, 800˚C, 900˚C, 1000˚C and 1200˚C for 1 hr followed by rapid water quenching. Hardness measurements were taken on samples after these heat treatments. The Vickers hardness evolution is shown in Figure 74. It indicates that the microstructure starts to recover after approximately 700˚C and completely recrystallized around 1000˚C. This essentially means that twins can be stable below 1000 ˚C.

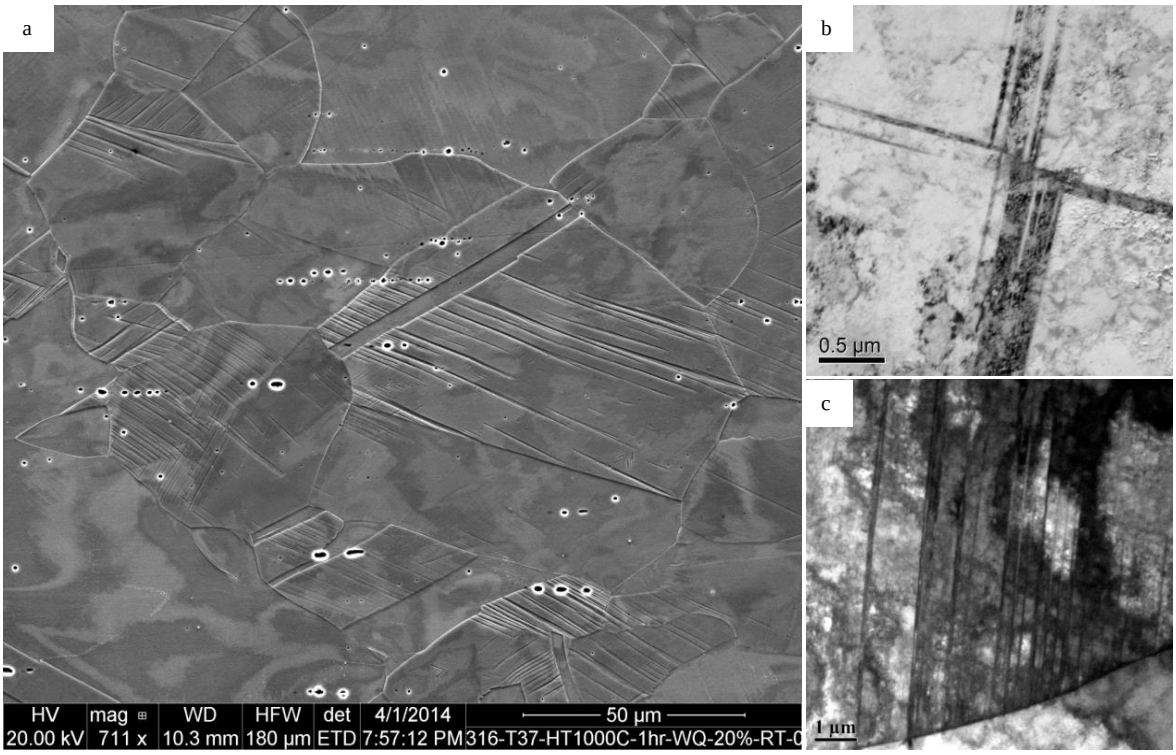

Figure 71- 316 Stainless steel annealed at 1000˚C for 1 hour, uniaxial tension to 20% elongation, a) SEM image after etching, b and c) BF TEM images.

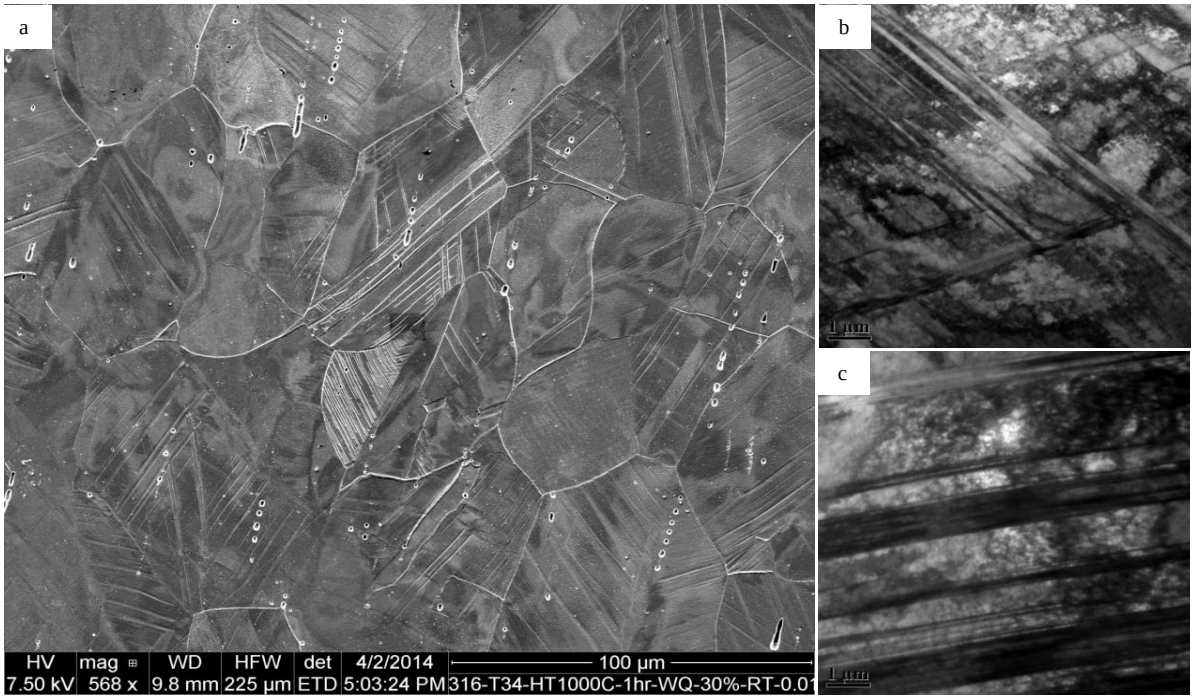

Figure 72 -316 Stainless steel annealed at 1000˚C for 1 hour, uniaxial tension to 30% elongation, a) SEM image after etching, b and c) BF TEM images.

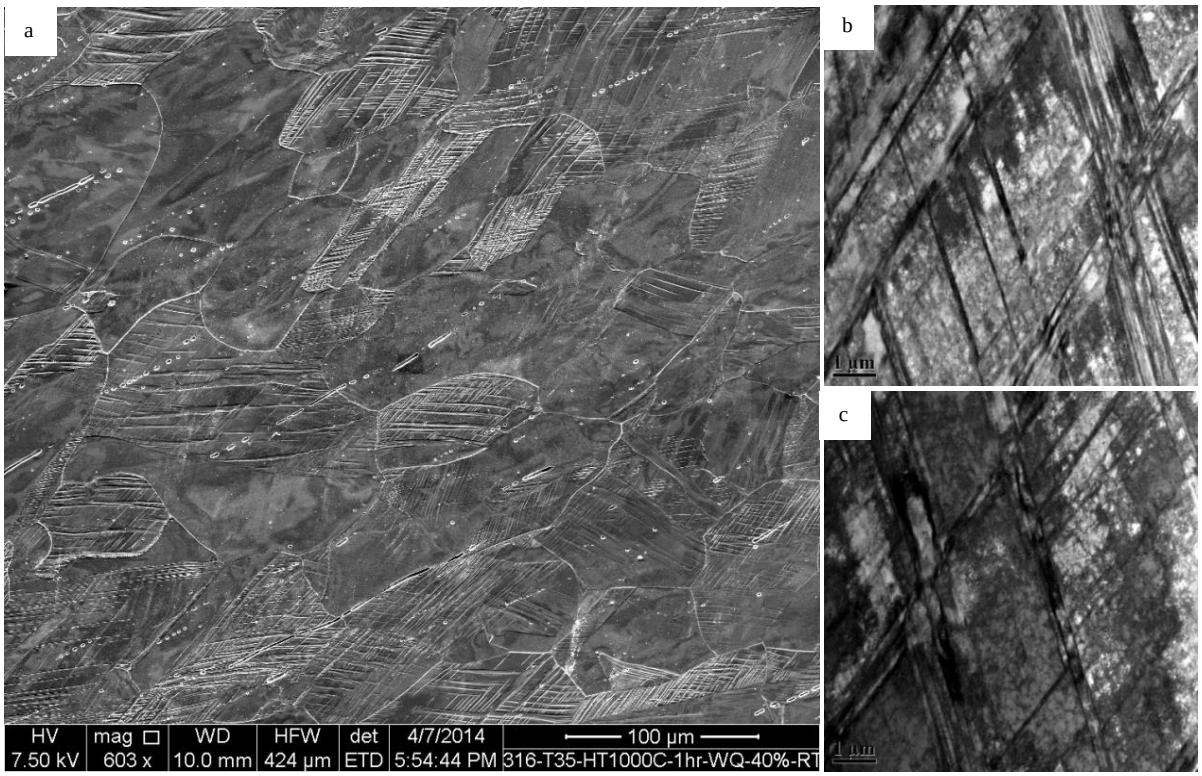

Figure 73- 316 Stainless steel annealed at 1000˚C for 1 hour, uniaxial tension to 40% elongation, a) SEM image after etching, b and c) BF TEM images.

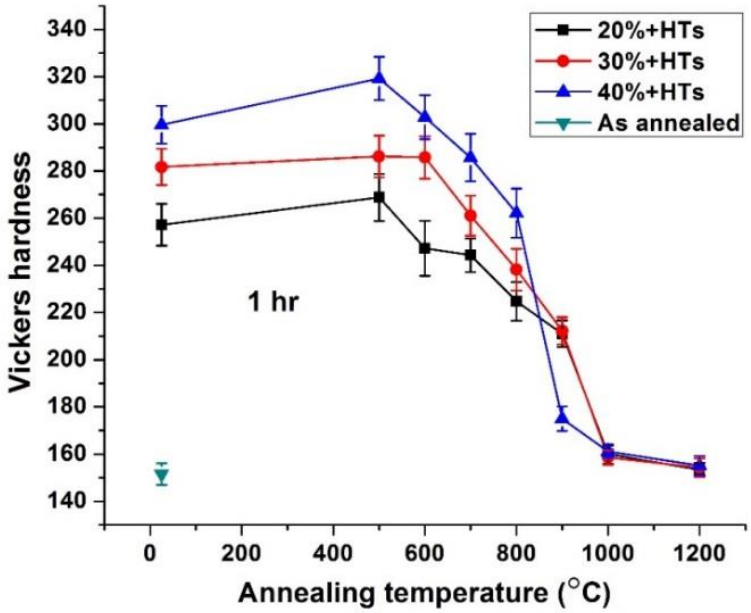

Figure 74- Evolution of Vickers hardness of uniaxially deformed 316 stainless steel, after annealing at 500˚C, 700˚C, 800˚C, 900˚C, 1000˚C and 1200˚C for 1 hour

In order to further confirm the thermal stability of deformation twins, in-situ heat treatments were conducted using a JEOL 2010 TEM. A 20% deformed sample was chosen for in-situ heat treatment experiments. 75 and Figure 76 show evolution of twins under heat treatment. They show that twins are very stable before 1000˚C. Moreover, when in-situ heated to 1000˚C, as shown in Figure 76, it can be seen that the twins are stable for about half an hour. From Figure 76-f, we can see that the twin disappeared after about 40 minutes at 1000˚C. Although the detected temperature during in-situ heating experiments has some deviations from the exact real temperature, the error range are estimated within 50˚C. So the results from in-situ heating experiments are consistent with that from the in-furnace heat treatments: the deformation twins in 316 stainless steel are stable in high temperature.

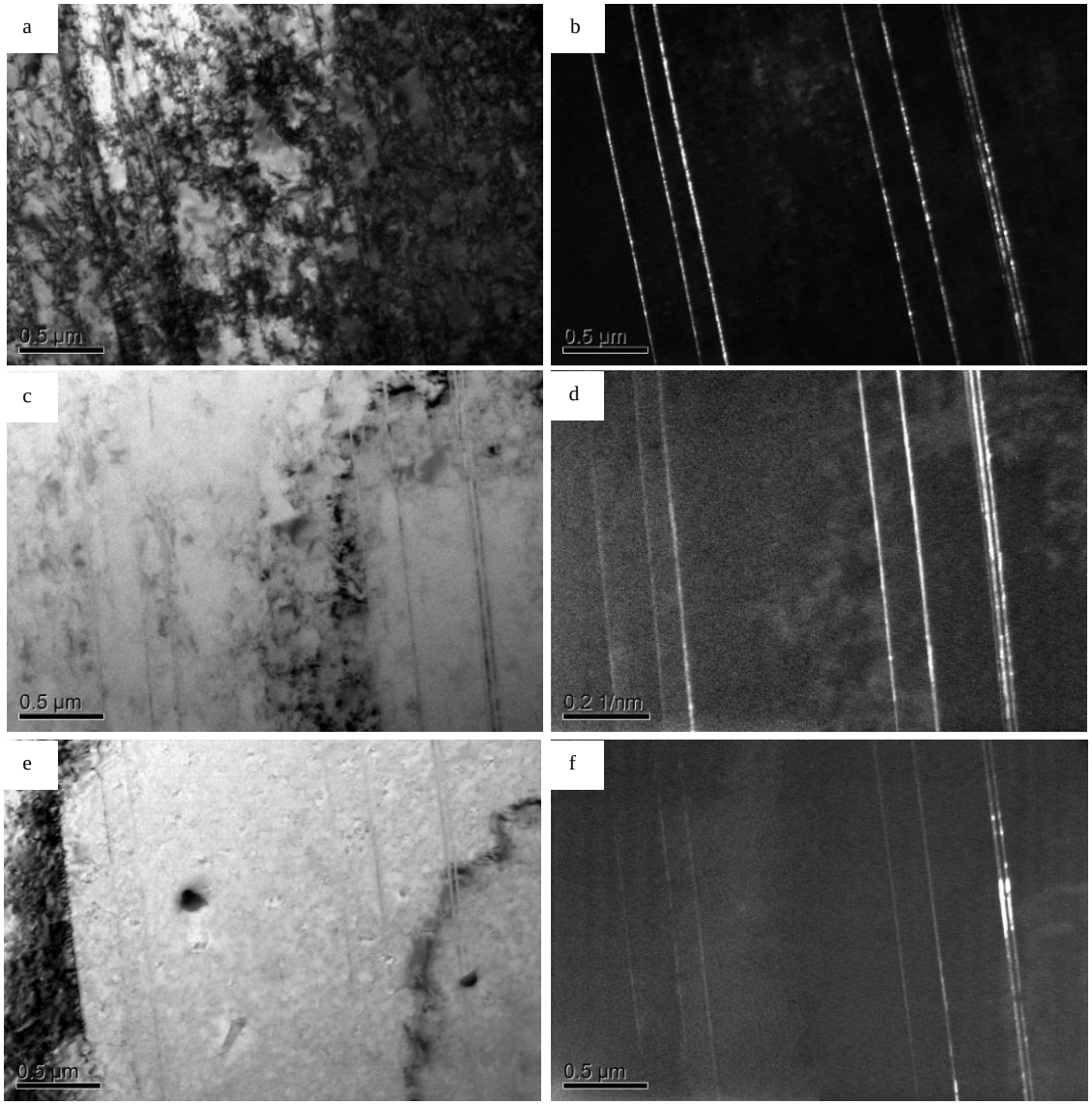

Figure 75- In-situ TEM images of 20% deformed 316 stainless steel a) BF at room temperature, b) DF of the twin at room temperature, c) BF at 470˚C, d) DF of the twin at 470˚C, e) BF at 900˚C, f) DF of the twin at 900˚C.

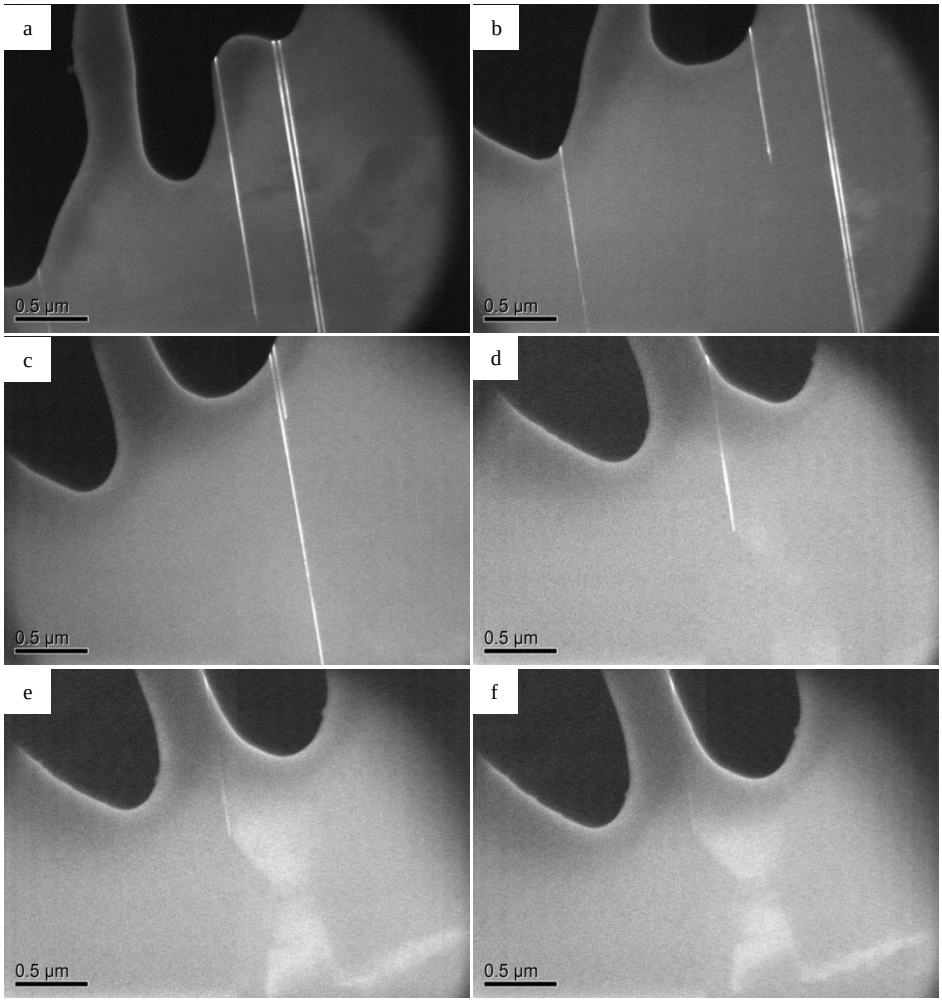

Figure 76- In-situ TEM images of 20% deformed 316 stainless steel, heated to 1000˚C for a) 10 min, b) 11 min, c) 22 min, d) 35 min, e) 36 min, f) 37 min.

The microstructural evaluation, as a consequence of the deformation, is depicted in Figure 77, which demonstrate a hierarchical microstructure consisting of very fine twin bands, which form larger twin bundles. As it can be seen, twin bundles may be from two different twinning systems that interact with each other. Higher resolution SEM images suggest that there is no interaction between the twins in the areas of contact. Moreover, the number of grains that have deformation twins increases, as well as the bundle-width and fraction of the twinning in individual grains. Figure 78 shows the statistical results of the number of grains with deformation twins, as well as the average twin density in each sample. Based on these results, the average twin density (twin fraction) increases with increasing tensile elongation, from almost 6.6% to 16.2%. In addition, the upper limit of twin fraction within any individual grain is almost 35%, meaning that a maximum of 1/3 of the grains deform by twinning. Figure 79 shows the statistical results of twin bands width, along with their relative frequencies, for the samples deformed up to different strain levels, after measuring more than ~700 twin bands at their edge-on condition in TEM. Based on these results, twin's width doesn't increase significantly with increasing strain levels. This result, combined with those of the previous figure, indicates that twin bands do grow in size as strain increases.

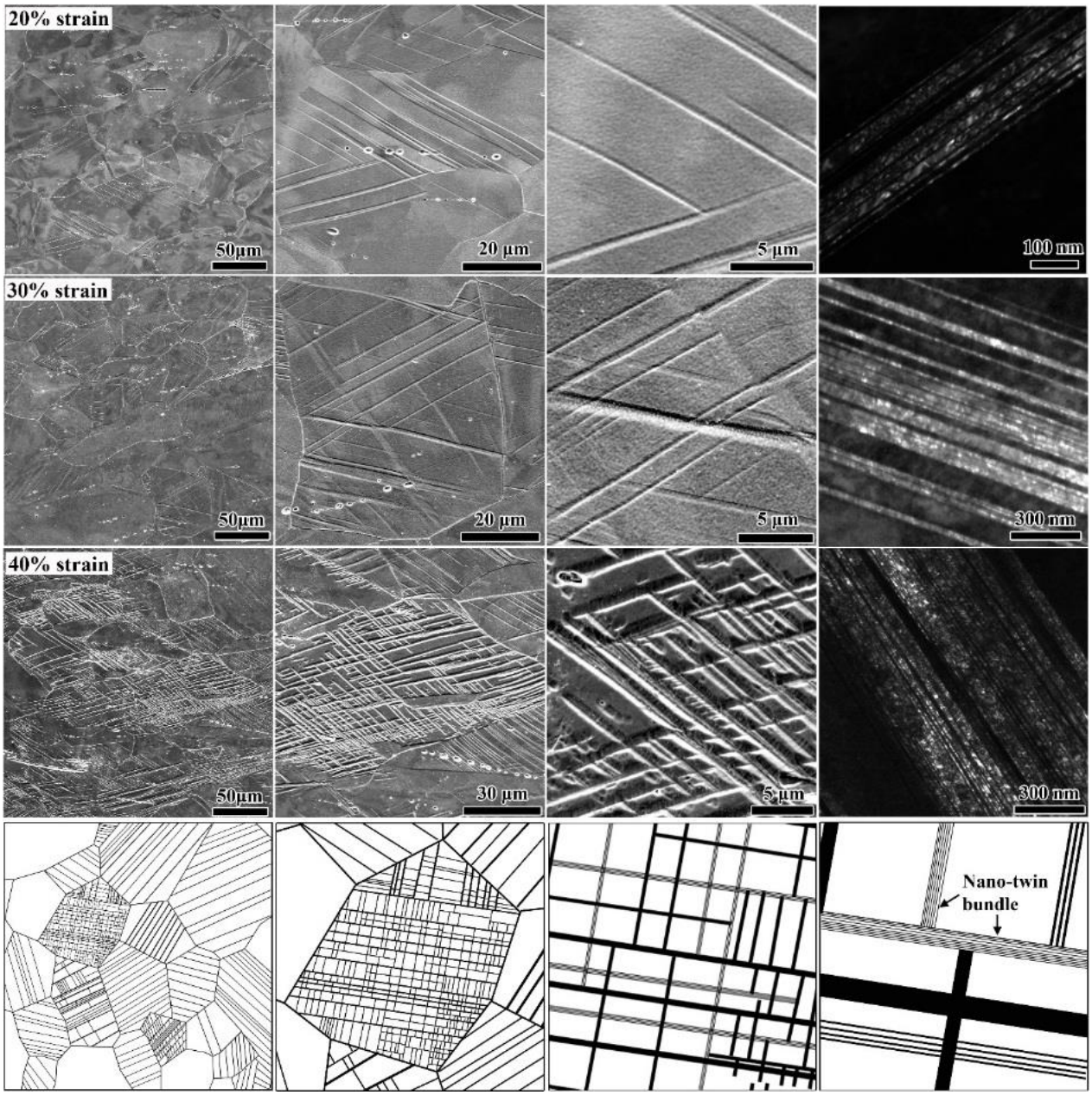

Figure 77- Microstructure evolution of 316 stainless steel samples under uniform elongations of 20%, 30%, and 40%. Bottom row images show schematics of the microstructures indicating a hierarchical structure.

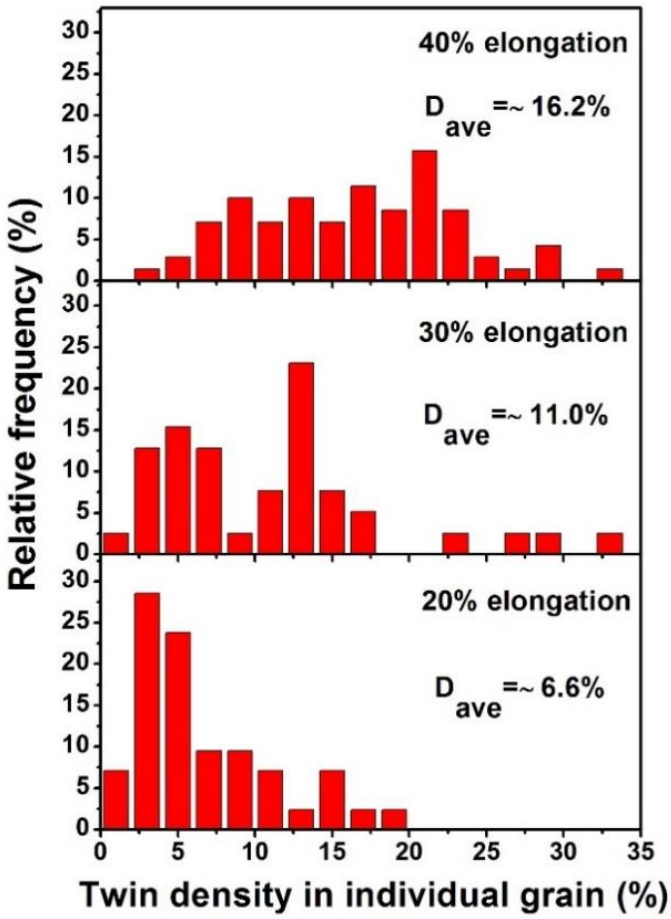

Figure 78- Distribution of twin density within individual grains after straining to different level, and their relative frequency (number of grains).

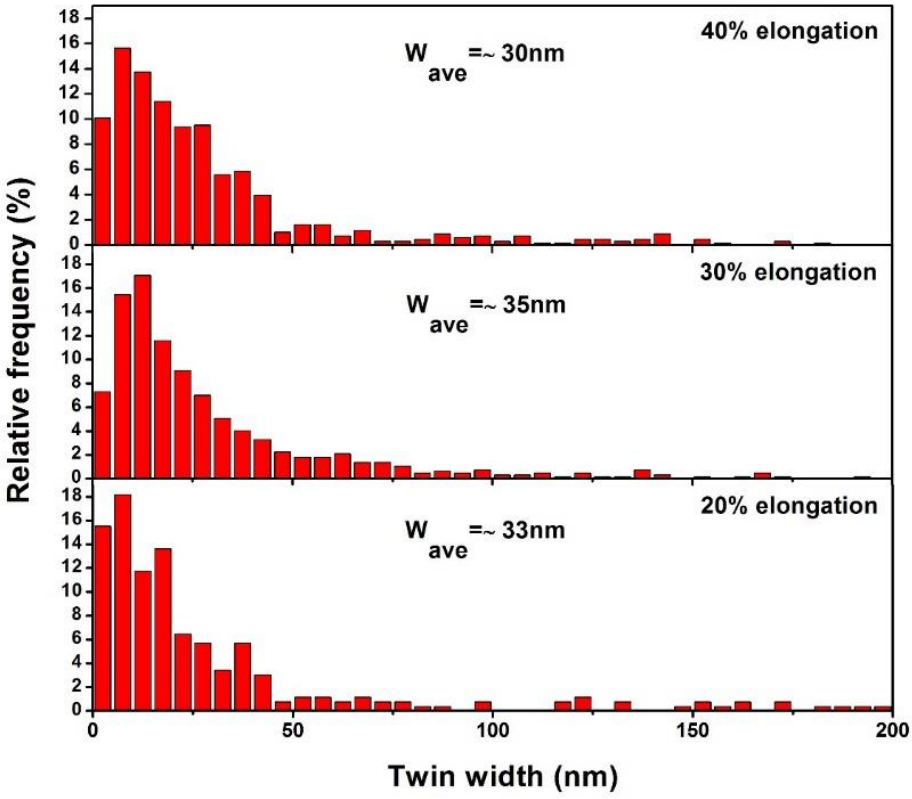

Figure 79- Distribution of twin width in deformed 316 stainless steel samples, and their relative frequency (number of twin bands).

The 20%, 30%, and 40% deformed samples were sealed in vacuum quarts tubes and then heat treated at 800˚C and 900˚C for 1 hour, followed by water quenching. These samples were then tested using uniaxial tensile tests at room temperature until failure (Figure 80). The tensile behavior of as-annealed samples (1000˚C) is shown in black for comparison. As it can be seen, the samples that were heat treated at 800˚C have yield stresses significantly higher than that of as-annealed samples, and failure-elongations are slightly smaller than that of as-annealed ones. As for the samples heat treated at 900˚C, the yield stresses are higher than that of as-annealed, and smaller than those of 800˚C heat treated. The same trend is visible at their failure elongations. This can be attributed to the partial recovery/recrystallization that occurs during heat treatments. The extent of recovery/recrystallization for 800˚C is less than that of 900˚C, thus the higher yield stresses and smaller elongations. Figure 81 shows TEM images of the samples that were deformed to different elongations and were then heat treated at 900˚C for 1 hour, then water quenched. These images prove that partial recovery/recrystallization has occurred in the samples, which is consistent with the strain-stress curves. Figure 82 is a combined TEM image, made of several TEM images. The interesting fact in this figure is that a new grain is being recrystallized from the interaction point of two twin bands, in shape of a balloon. Investigation on this phenomenon will continue, trying to determine the relation between the orientation of the matrix and the new grain.

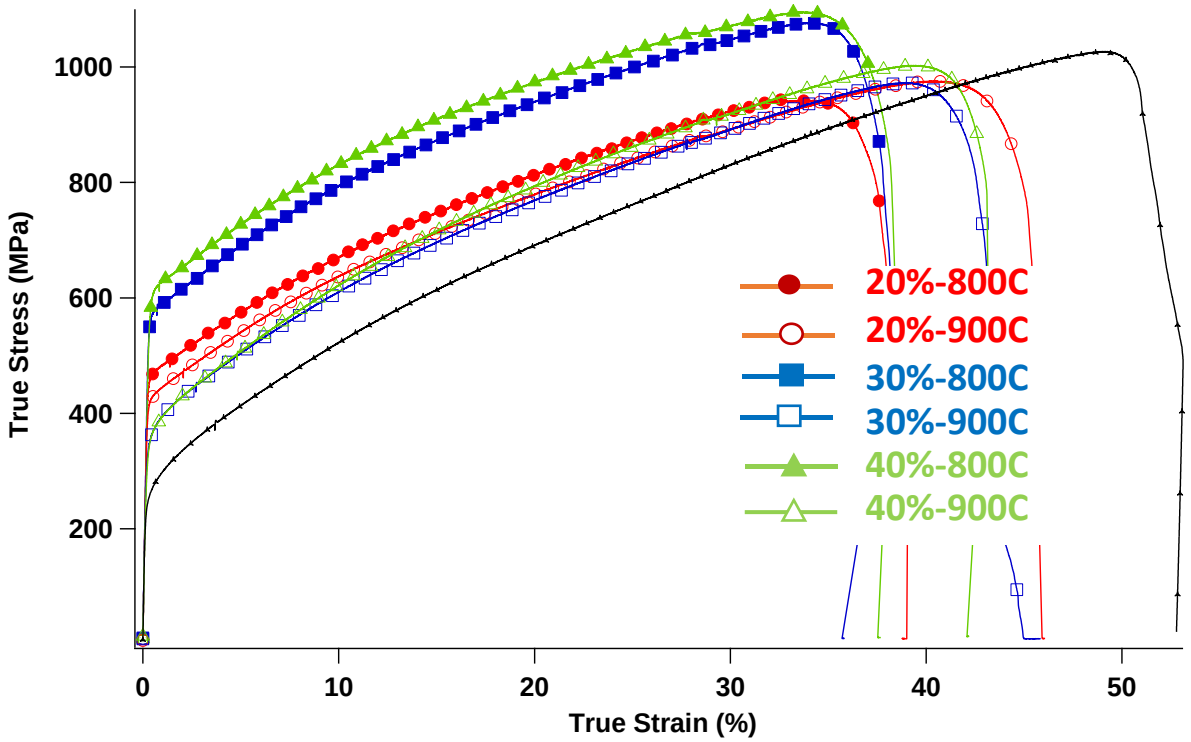

Figure 80- Stress-strain behavior of samples deformed 20%, 30%, and 40%, then heat-treated at 800C and 900C for 1 hour.

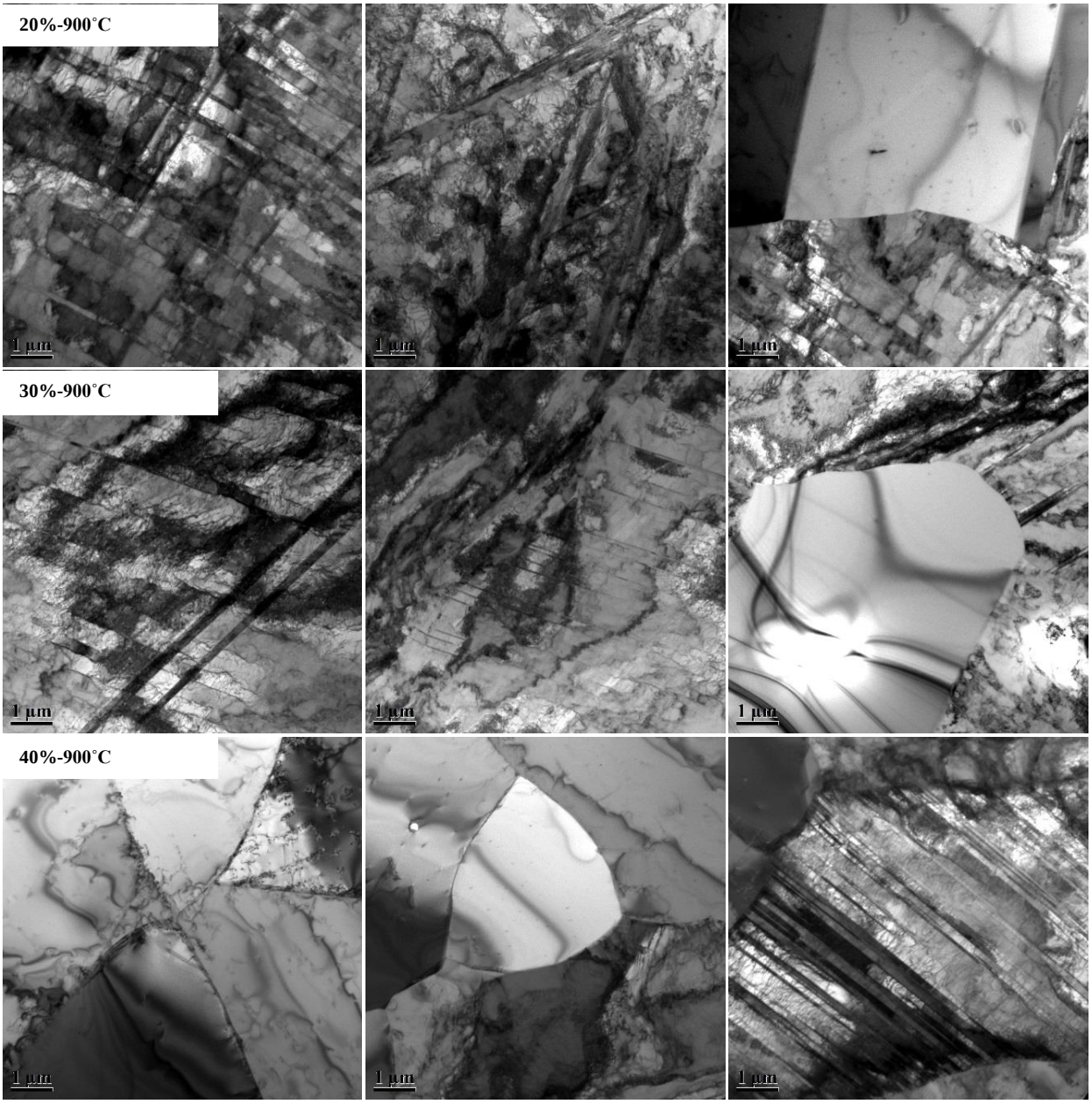

Figure 81- TEM images of samples deformed to 20%, 30%, and 40% elongations then heat treated at 900˚C for 1 hour then water quenched.

Figure 82- A combined TEM image of a recrystallizing grain.

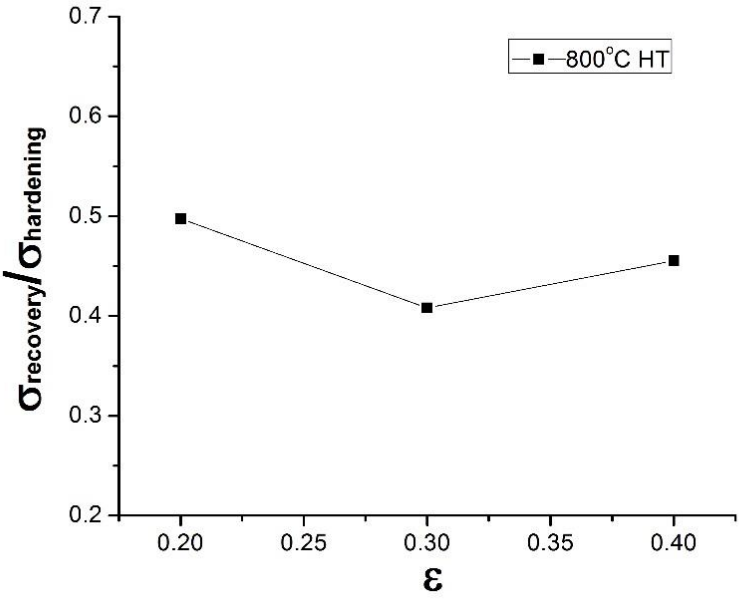

Figure 83-$\sigma_{recovery}/\sigma_{hardening}$ ratio for 316 stainless steel samples deformed to 20%, 30%, and 40% engineering strains and heat treated at 800˚C for 1 hour.

Next, the flow stresses of 20%, 30%, and 40% deformed samples were measured against their respective yield stresses after the heat treatment at 800°C. This temperature was selected for heat treatment because it was previously shown that only dislocation recovery happened at this temperature and no recrystallization was observed. Two new terms are introduced: 1-hardening stress ($\sigma_{hardening}$) which is the difference between the yield stress of the material and its highest flow stress (flow stress at 20% strain for example), 2-recovery stress ($\sigma_{recovery}$) which is the difference between the highest flow stress of a sample and its yield stress after the heat treatment. In other words, $\sigma_{hardening}$ is a measure of how much the material hardens during cold work, and $\sigma_{recovery}$ is a measure of how much the material is recovered during the heat treatment. The ratio of these two terms (i.e. $\sigma_{recovery}/\ \sigma_{hardening}$) is used as a measure for understanding how effective a thermo-mechanical process is, in terms of mechanical properties. *Figure* 83 shows this ratio for 316 stainless steel sample, after 800˚C-1hour heat treatment. Based on this figure, the 30% elongation has the lowest ratio, which means it has the most effective thermo-mechanical process.

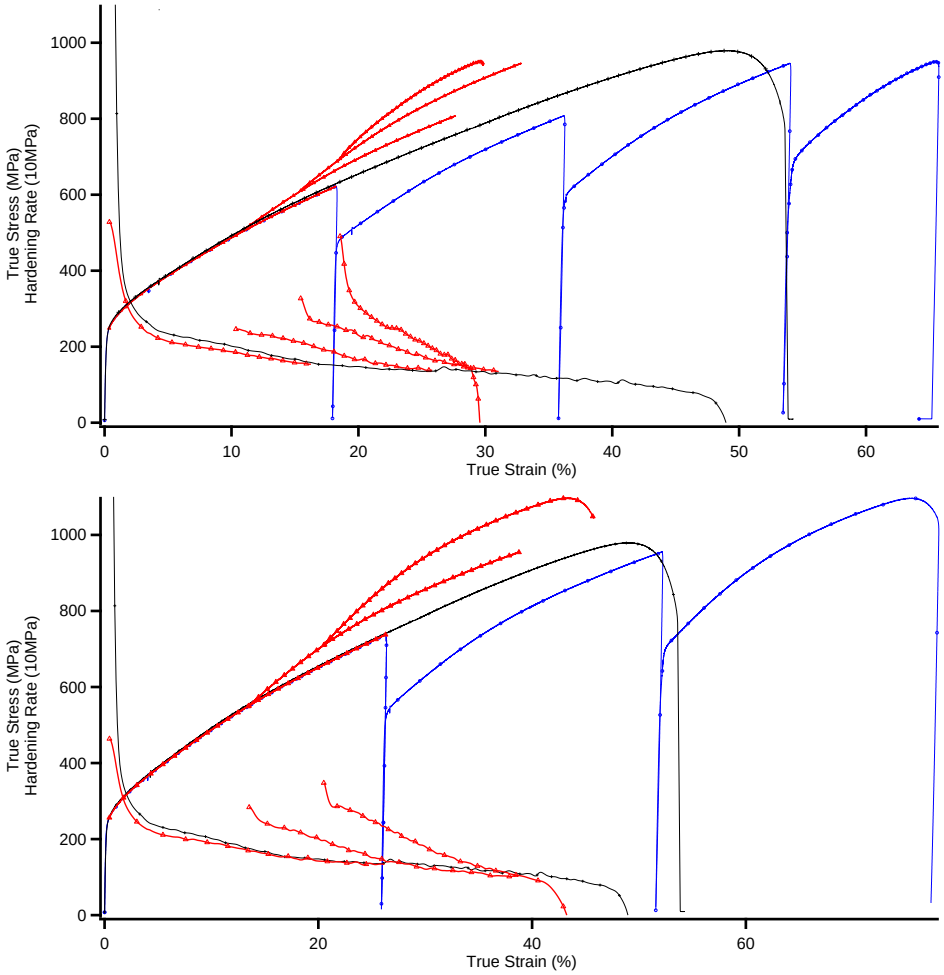

Figure 84- True stress vs. strain curves of 316 stainless steel (blue), continuous plastic flow and corresponding hardening rate (red), compared with the as-received (black), for: top) 20% eng. strain + HT800°C-1hr, and bottom)) 30% eng. strain + HT800°C-1hr

Based on the results of the previous section, in order to reach the maximum level of twin density one can achieve via repeated tension and annealing, two fully annealed 316 stainless steel tensile samples were deformed using uniaxial tension test at room temperature to 20% and 30% respectively. The samples were then heat treated at 800°C for 1 hour at controlled atmosphere, with a subsequent rapid water quenching. This specific heat treatment was selected based on previous results indicating that recovery of dislocations occur, but deformation twins remain after this heat treatment. Then the sample with 20% pre-deformation was deformed uniaxially at room temperature to 20% engineering strain, followed by the specified heat treatment. This process was repeated until the sample fails during the tension test. Same procedure was performed on the 30% strain sample too. The stress-strain response is depicted in Figure 84. Also in this figure, the plastic region of the curves are shown in a continuous manner. For example, the yield strain of the second curve was shifted so that its flow stress starts on the plastic region of the first curve. This method was applied to all the curves. The figure includes the hardening rate (slope) of the stress strain curves as well.

The purpose of this test was to study the mechanical response of this steel with a structure that has deformation twins but the dislocations are recovered. In addition, finding a relationship between the twin volume density in the structure and the mechanical response was another goal of this study. To this end, the samples after the repeated tensile tests + heat treatments were polished and etched and studied using SEM/BSE. The results (Figure 85 and Figure 86) will be studied using analytical methods to evaluate twin density in each case, and find the correlation between twin density and mechanical response, as well as high-temperature uniaxial test to study the effect of the achieved microstructure on high-temperature mechanical response.

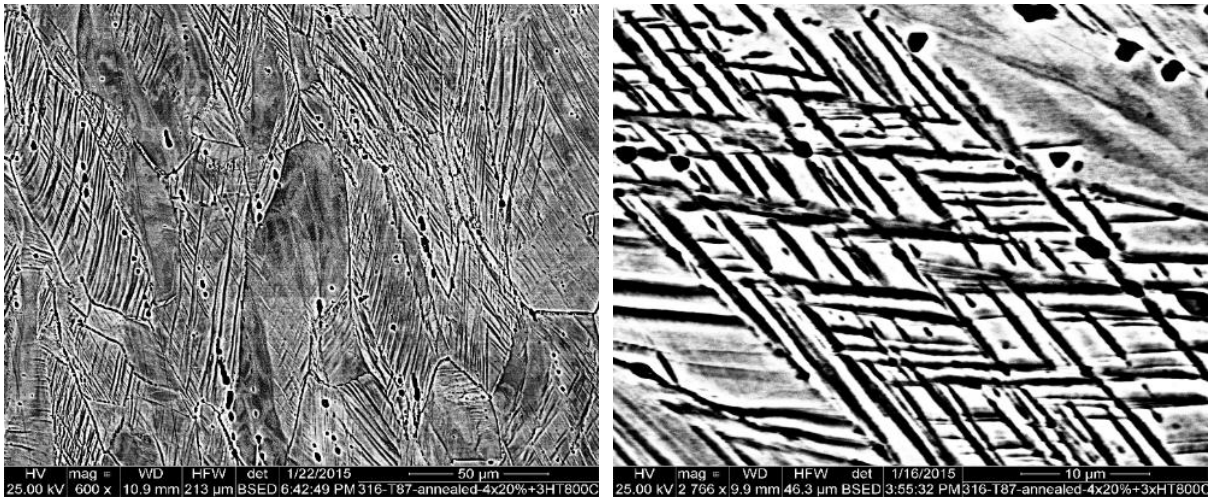

Figure 85- BSE/SEM image of 316 stainless steel etched after 4 times 20% eng. strain interrupted with 3 times heat treatments at 800°C for 1 hour showing the significant increase in the twin density upon thermo-mechanical processing.

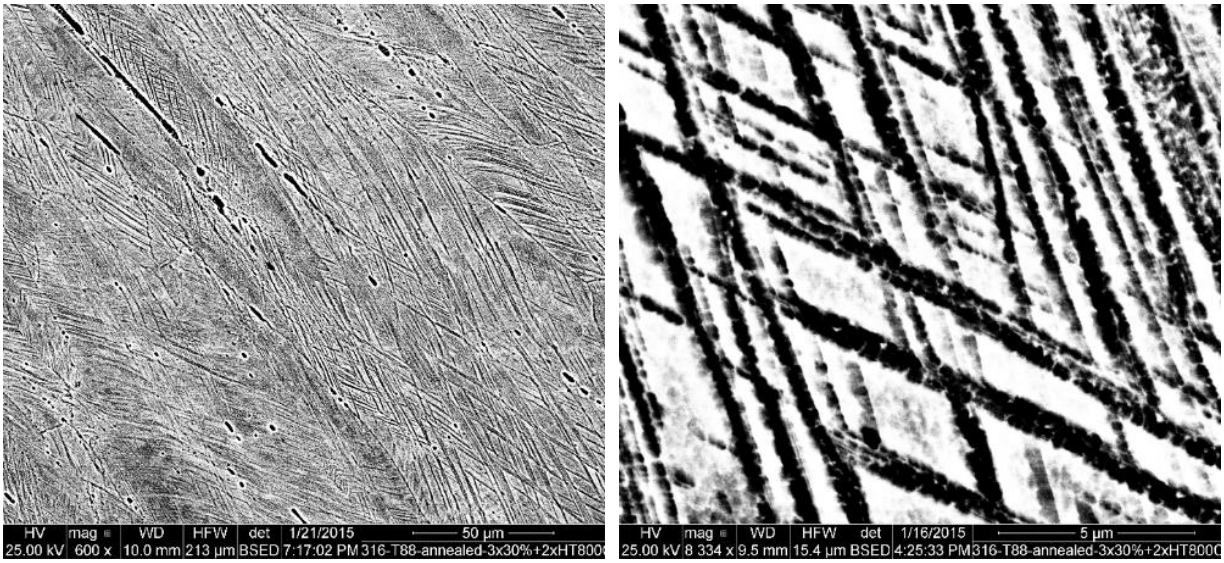

Figure 86- BSE/SEM image of 316 stainless steel etched after 3 times 30% eng. strain interrupted with 2 times heat treatments at 800°C for 1 hour

4. Customized Composition Alloy

a) Alloy 1

The OM image in Figure 87-a shows the homogenized microstructure with an average grain size of about 10 μm. In addition, the precipitates are also evident. To identify the precipitates observed in Figure 87-a, SEM was performed together with EDS analysis. Figure 87-b shows the BSE image of the as received Al1. Bright precipitates are seen throughout the sample. The black dots originate from the sample preparation. EDS was performed on both the matrix and bright precipitates, the location of which have been marked in the figure. Figure 87-c shows the EDS spectrum of the matrix. The major elements are determined to be Fe, Cr, Ni, Mn, Mo, Al, Nb and Si, which match the elemental analysis reported in Table 1. Comparing with the matrix, the bright precipitates contain mainly Nb as suggested in Figure 87-d, which indicates that the bright precipitates should most likely be Nb carbides.

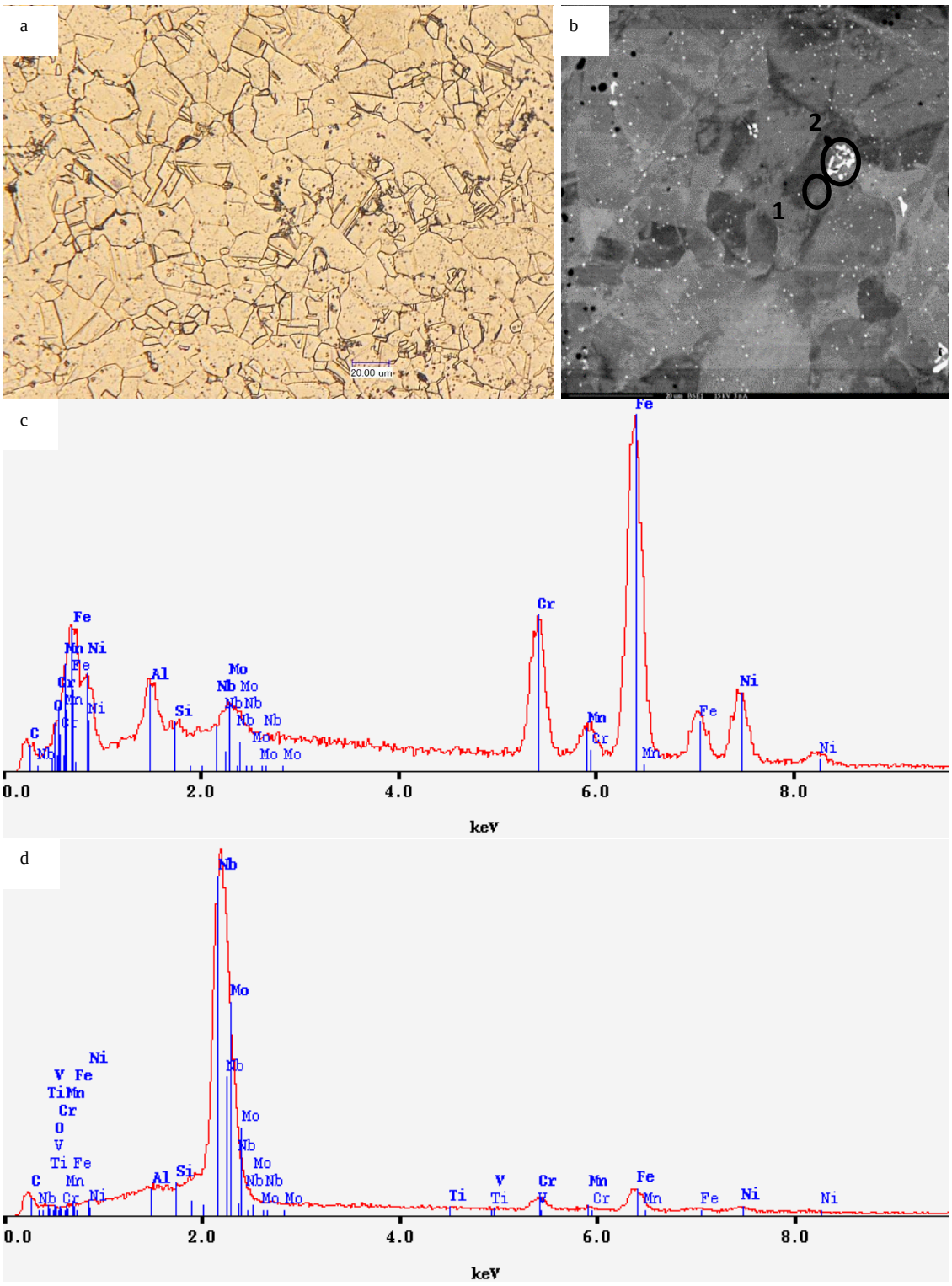

Figure 87- a) OM image of Alloy 1 (Al1), showing a homogenized microstructure together with some precipitates; (b) BSE image of Al1, showing bright precipitates throughout the sample; EDS spectrum of the matrix (c) and the bright precipitates (d). The marks in (b) indicate the location of the EDS measurements

XRD measurements were performed on the as received samples to determine the crystal structure. The results (the upper spectrum in Figure 88 show that austenite phase dominates the alloy, which fulfills the design goal. However, it can be seen that there appears to be a number of minor peaks in the spectrum, which indicates that some impurities (such as precipitates) exist in the microstructure. Attempt has been made to dissolve the impurities by an additional heat treatment at 1200 °C for 1hr and subsequently water quenching. Unfortunately, the impurities still exist according to the bottom spectrum in Figure 88.

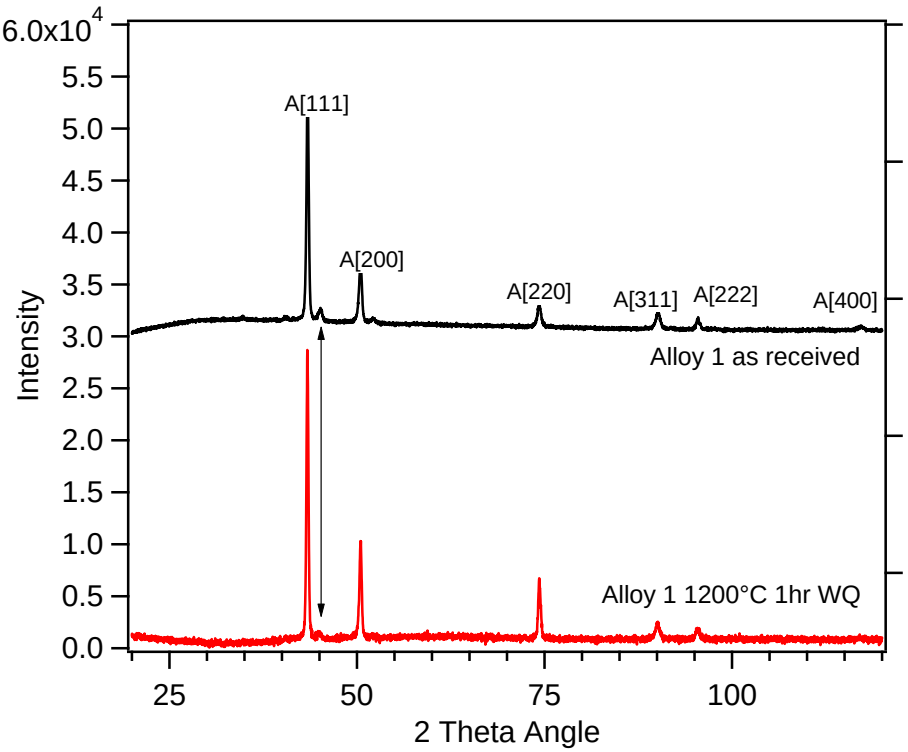

Figure 88- XRD spectrums of as received Al1 (top),

The microstructure of the Al1 sample after the additional heat treatment at 1200°C for 1 hr was further studied. The OM image (

Figure *89*-a) indicates that the heat treated microstructrue has a much larger grain size (~100 μm). The precipitates can still be observed, which supports the results obtained from XRD. The BSE image (

Figure *89*-b) is in agreement with the OM observation. Similar bright precipitates remained in the microstructure. EDS characterization shows that the bright precipitates are still dominated by Nb and is most likely Nb carbides (

Figure *89*-c).

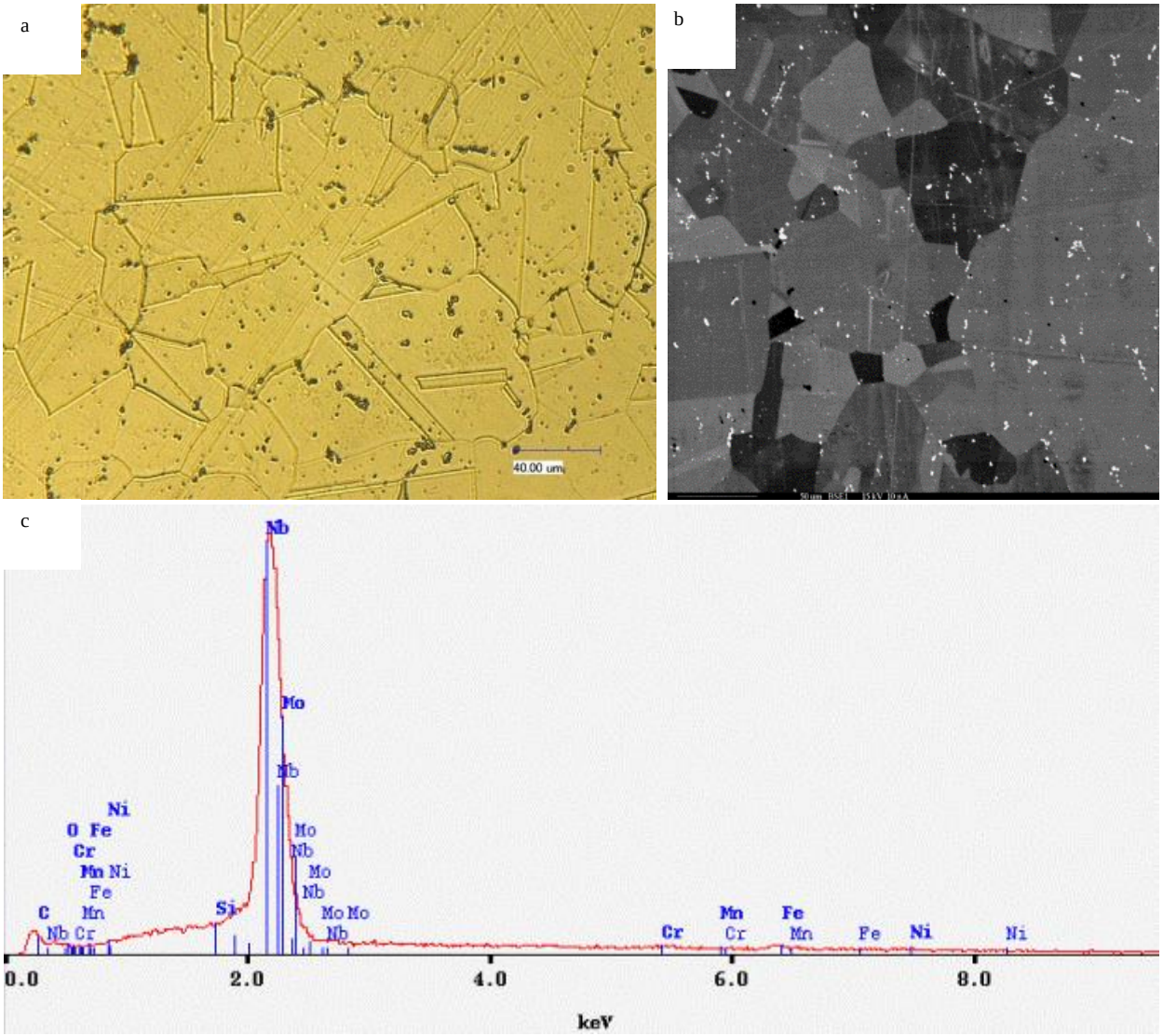

Figure 89- a) The OM image of the Al1 sample after the heat treatment at 1200°C for 1hr and water quenching, corresponding BSE image (b), and the EDS spectrum of the bright precipitates

Dog-bone shaped samples were used for uniaxial tension tests. Figure 90-a shows the stress-strain behavior of this sample and the derivative of stress with respect to strain. The observed behavior implies that twinning has had a role in deformation. OM images of the sample (Figure 90-b) show surface features that can be a sign of twinning. EBSD analysis was performed on Al1 samples deformed to 10% at room temperature (Figure 90-c), but the obtained IPF analysis (Figure 90-d) were inconclusive regarding the presence of twinning. As a result, samples were studied using TEM, and the results are shown in Figure 91.

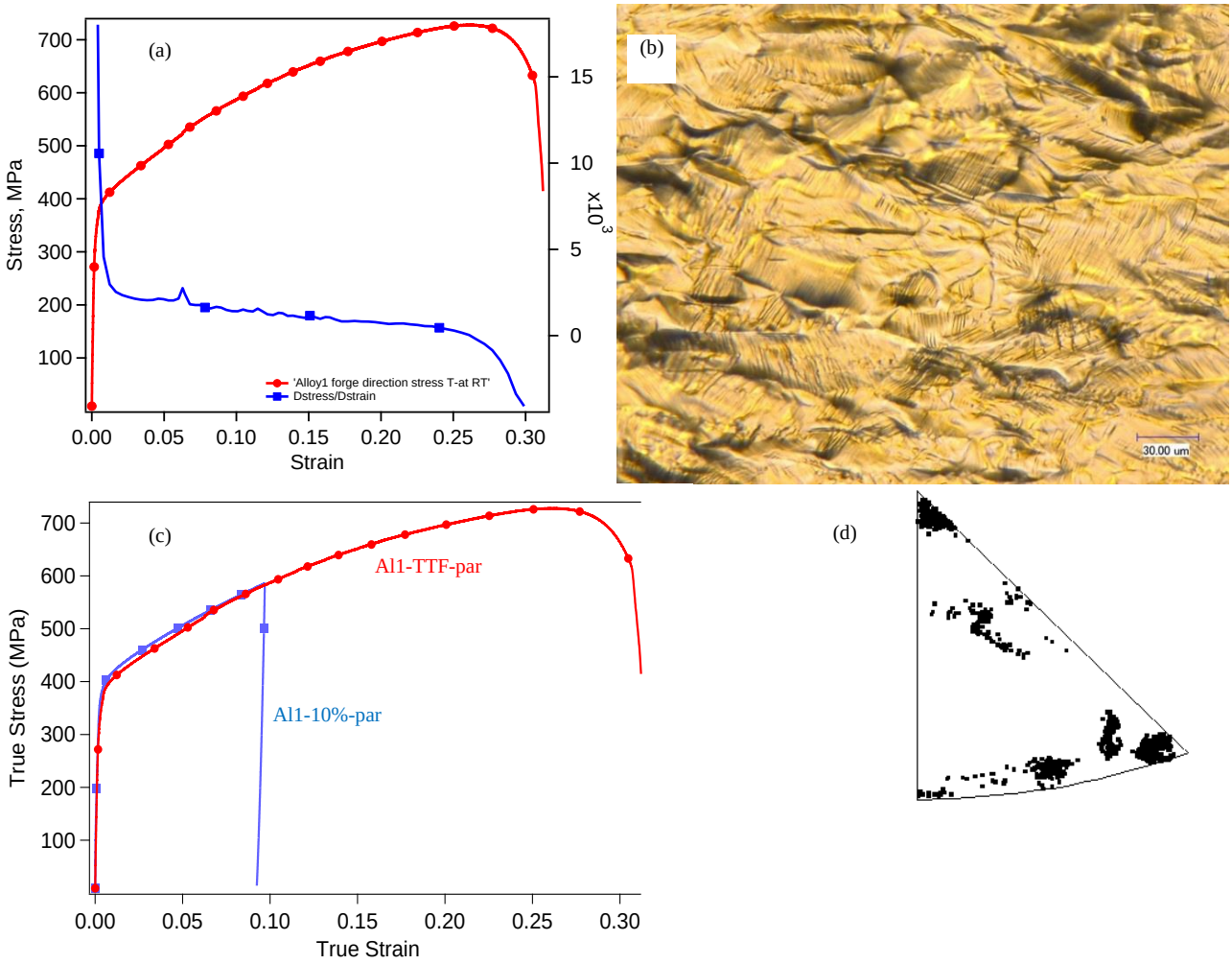

Figure 90- Al1 parallel to forging direction: a) stress-strain behavior to-failure at room temperature and its derivative, b) OM of surface features of the sample in (a), c) stress-strain response of the samples up to 10% deformation and till failure at room temp

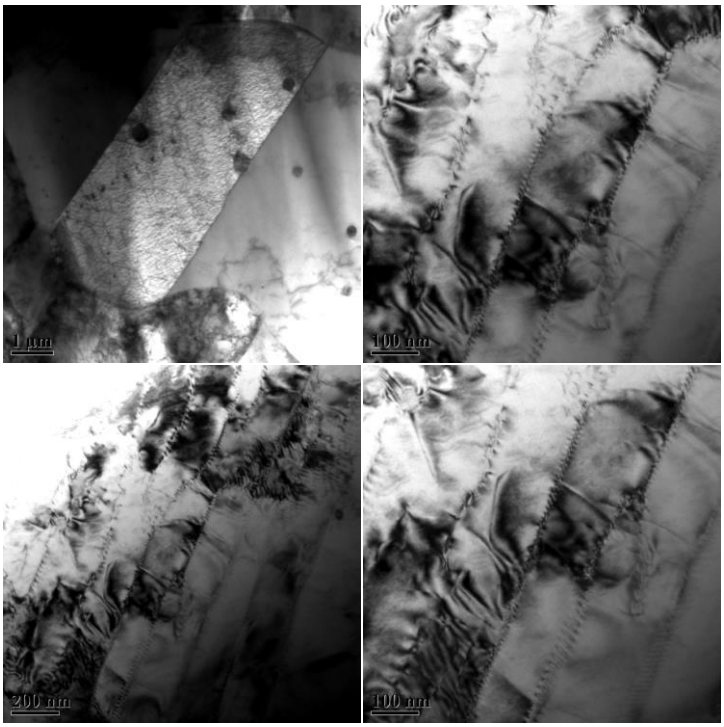

Figure 91- TEM image of Al1 samples after 10% strain deformed parallel to the forging direction

To maximize twinning, Al1 bar, which was received as-forged, was studied using X-ray Diffractometry (XRD) in order to find out the texture so that dog-bone samples can be prepared with the tensile direction closest to {111} direction (i.e. in a way that most grains {111} orientation are along the tension direction). The results (Figure 92-left) showed that the transverse direction provides the closest orientation to {111}, thus the samples were cut out of that direction and were called Al1-TD.

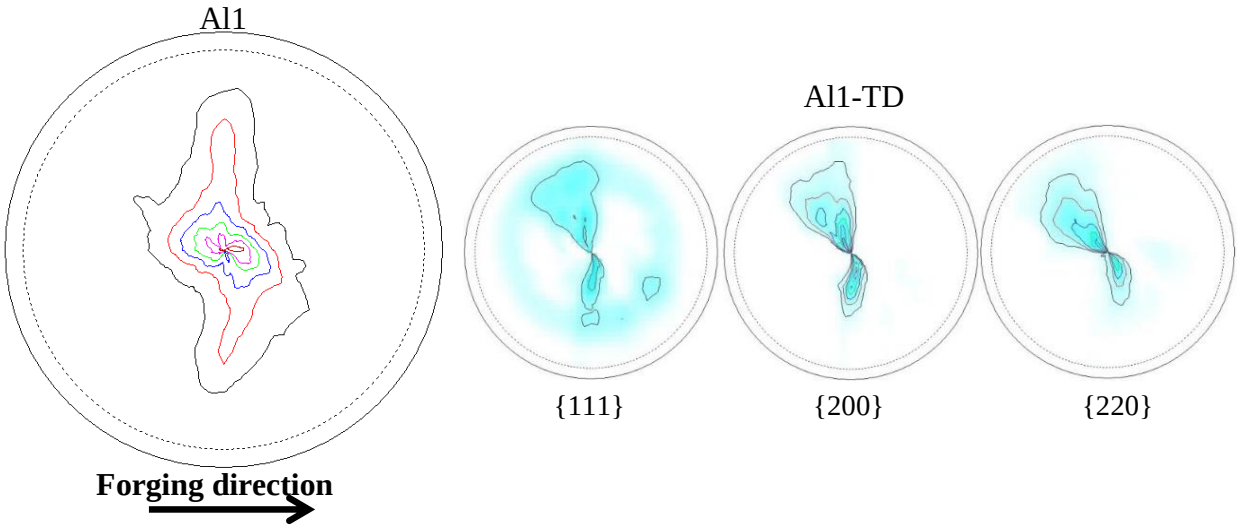

Figure 92- Texture of Al1 left) as-forged and right) cut along Transverse Direction

Al1-TD samples were then deformed uniaxially to 5 and 10% at room temperature (Figure 93-a) and their texture was studied using XRD (Figure 93-b). In order to investigate the twin-ability, deformed samples were studied using EBSD, and the acquired pole map (Figure 93-c), suggests that bands of twinning exist in the sample. To confirm, TEM was performed on the sample and as the results in Figure 94 show, twin formation has been a mechanism of deformation. In Figure 94-a, the bright field TEM shows bands in order of less than to a couple of μm, which are then found to be twins with the help of the SAD pattern in Figure 94-b. Further studies are being performed on this baseline material to better understand the twin formation and other mechanical properties at room temperature and elevated temperatures.

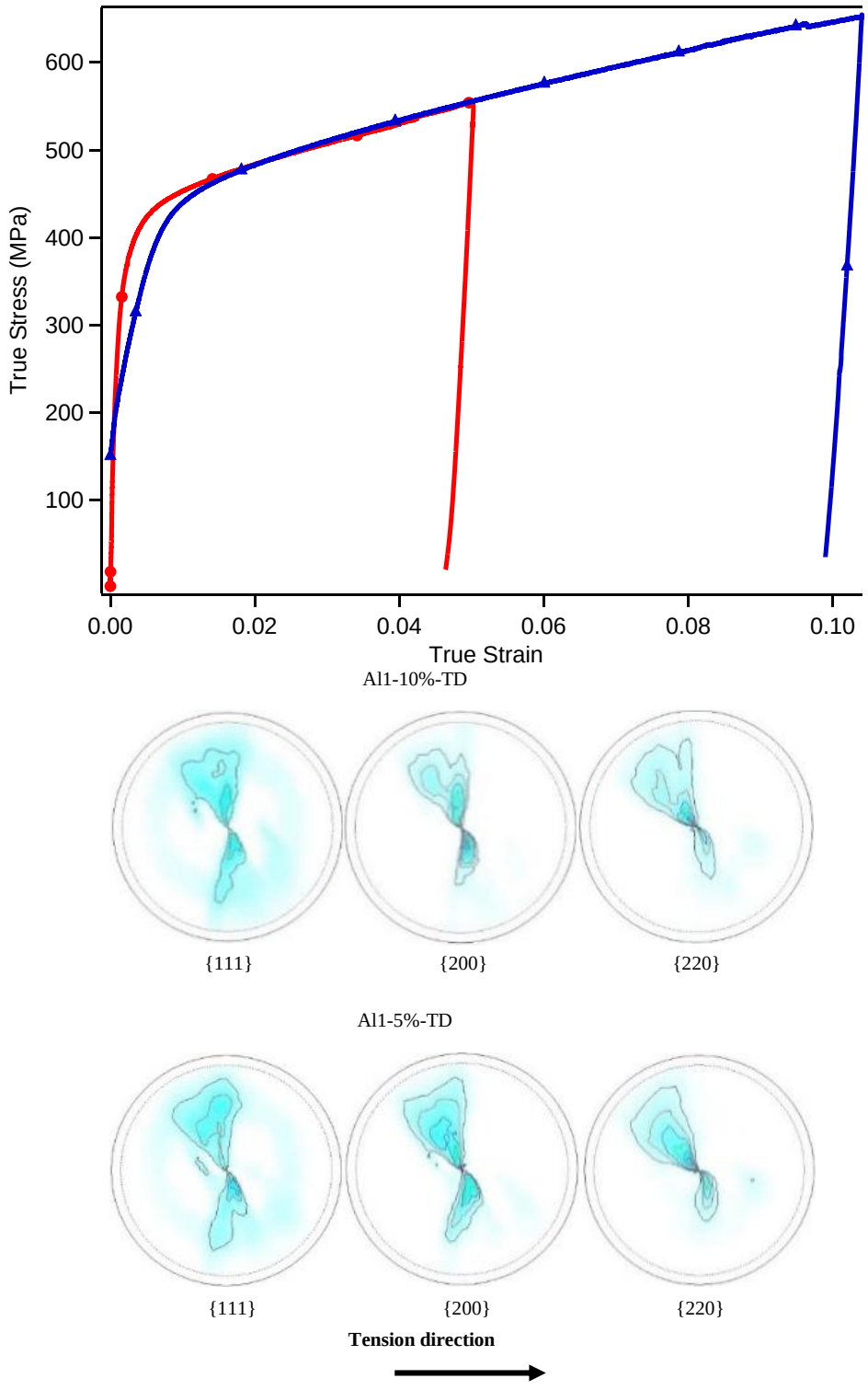

Figure 93 a) uniaxial tension test of Al1-TD, b) texture of Al1-TD after 5% and 10% deformation at room temperature

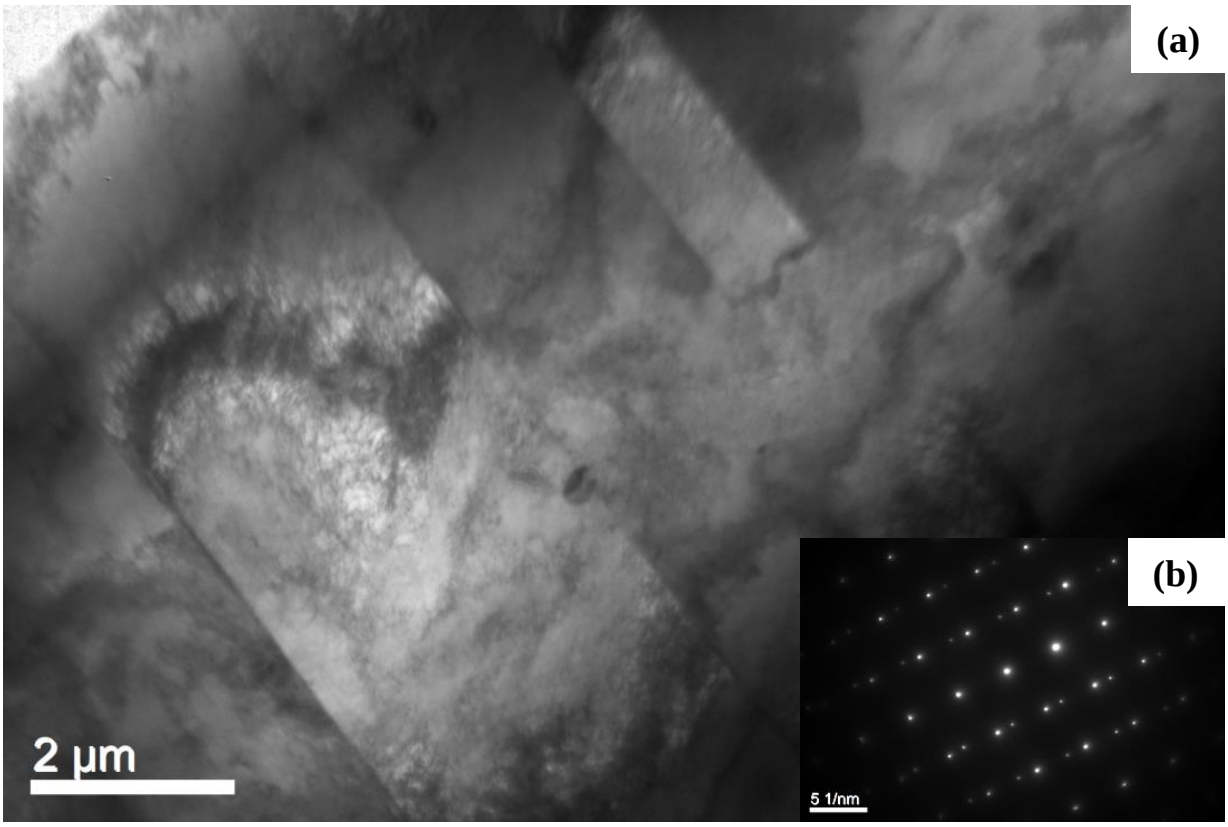

Figure 94-TEM image of Al1-TD sample deformed to 10% strain at room temperature showing deformation twins

The EBSD map with 1µm step size (Figure 95), however, shows very little sign of twinning within the sample. One of the possible justifications for this phenomenon is that the mechanical twinning formed due to plastic deformation is too small to be detected, but maybe after heat treatment and converting to heat treatment twining, EBSD will be able to detect the twin bands.

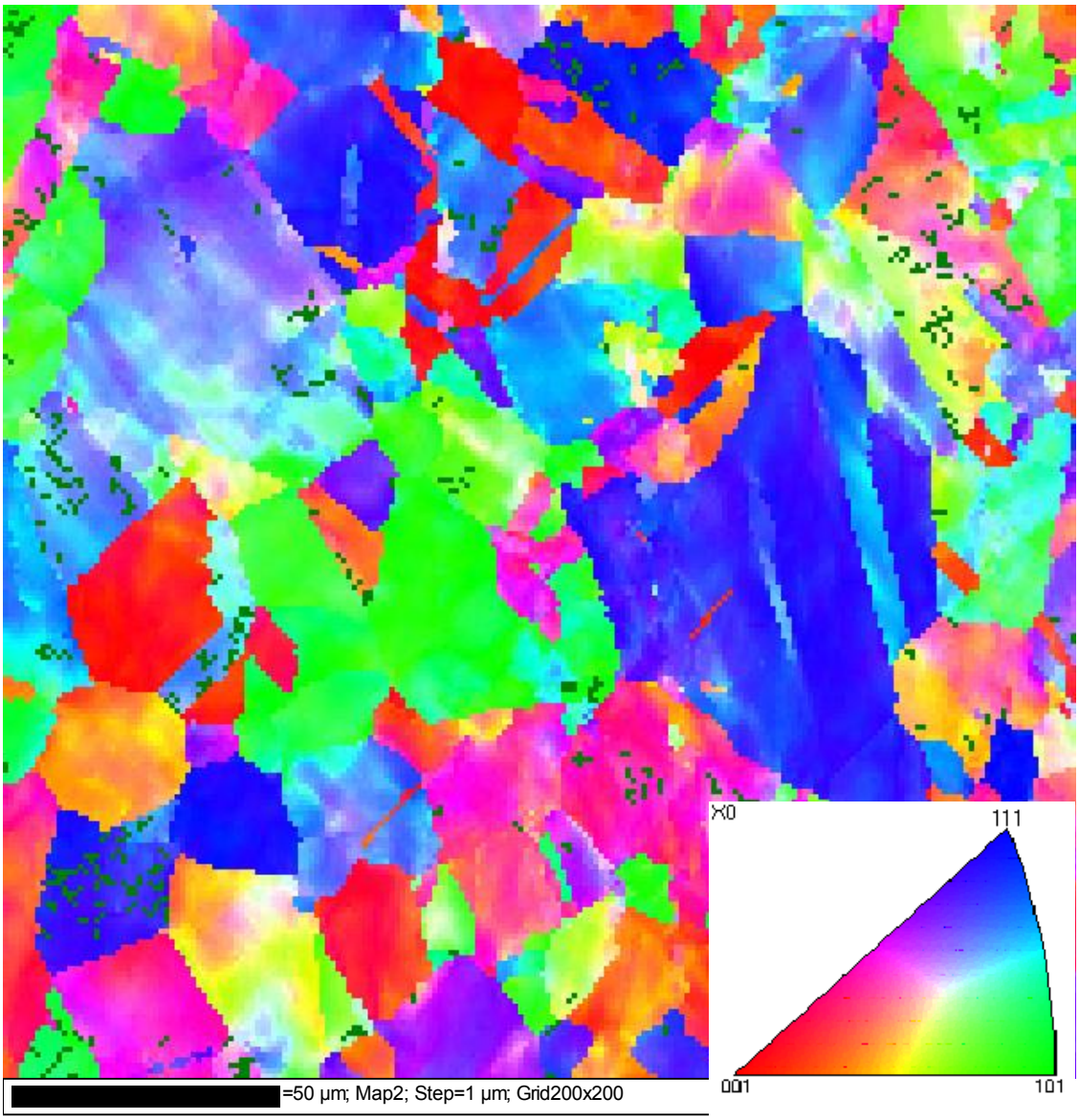

Figure 95- EBSD map of Al1-TD deformed 10% at room temperature

The evaluation of the alloy 1 single crystalline samples started with optical microscopy of the samples. The results (Figure 96-a and b) depict the presence of an inter-dendritic precipitate. In order to try and dissolve these precipitates, samples of this alloy were heat treated at 1200°C and 1300°C separately, for 1 hour and then subsequently water quenched. The OM images of the heat treated samples (Figure 96-c and d) show that the precipitates persist without any significant change during the somehow drastic heat treatment.

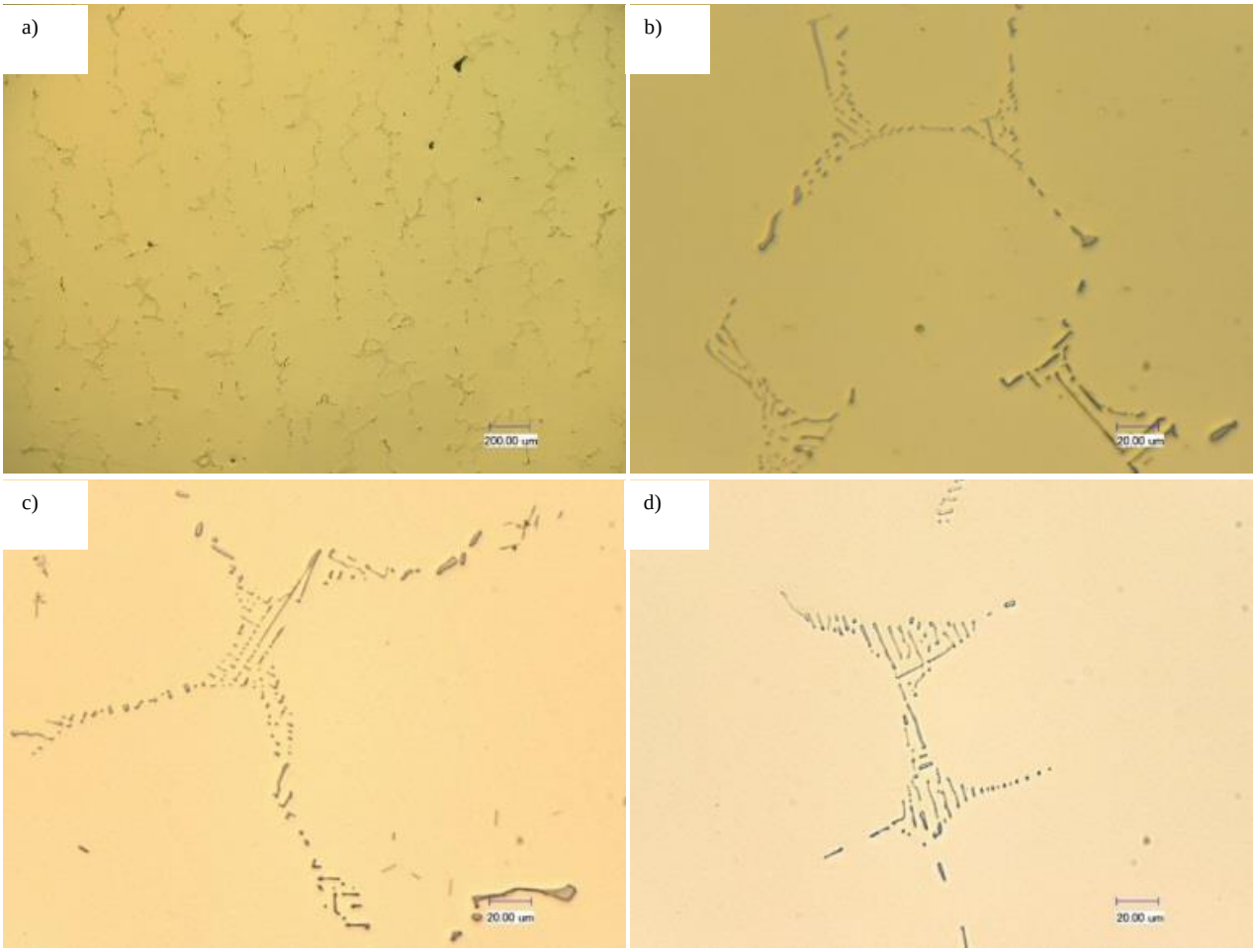

Figure 96-OM images of alloy 1 [111] single crystals a) and b) as received, and after heat treated at c) 1200°C, and d) 1300°C for 1 hour

In order to identify the nature of the precipitations in alloy 1 [111] single crystal, they were studied using SEM and BSEM as well as EDS. The electron microscopy images (Figure 97) vividly show the presence of these precipitates. The element mapping of this sample (Figure 97-c) shows that these precipitates are highly concentrated with niobium. The quantitative analysis of the spot shown in Figure 97-a depicts that these precipitate is mostly niobium and carbon, with an almost 1:1 ration, making this a niobium carbide precipitate, which then explains why it couldn't be dissolved with heat treating even at 1300°C.

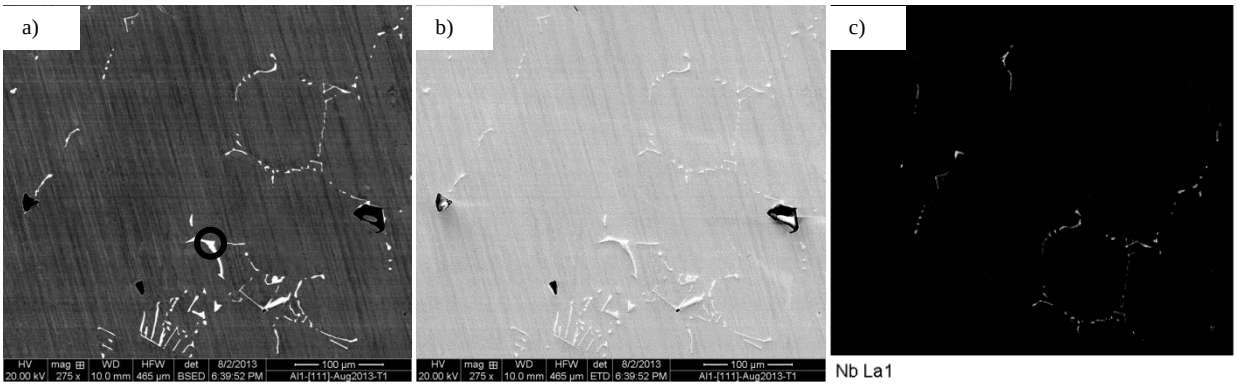

Figure 97- Alloy 1 [111] single crystals a) BSE image, b) SEM image and, c) Nb map

Single crystalline [111] tensile samples prepared from alloy 1 were heat treated at 1200°C for 1 hour followed by water quenching, and were then characterized using OM (Figure 98). This tensile sample was then used in a uniaxial tensile test at room temperature and then deformed until fracture. The obtained stress vs. strain curve from this test (Figure 99-a) is very similar to that of the polycrystalline alloy 1 previously reported, with the difference that the single crystalline sample showed an ultimate elongation almost equal to one third of that of the polycrystalline sample. The OM investigation of the samples (Figure 99-b and c) reveals parallel surface features similar to those of stainless steel single crystals. These surface features were also present in the poly crystalline deformed samples previously reported.

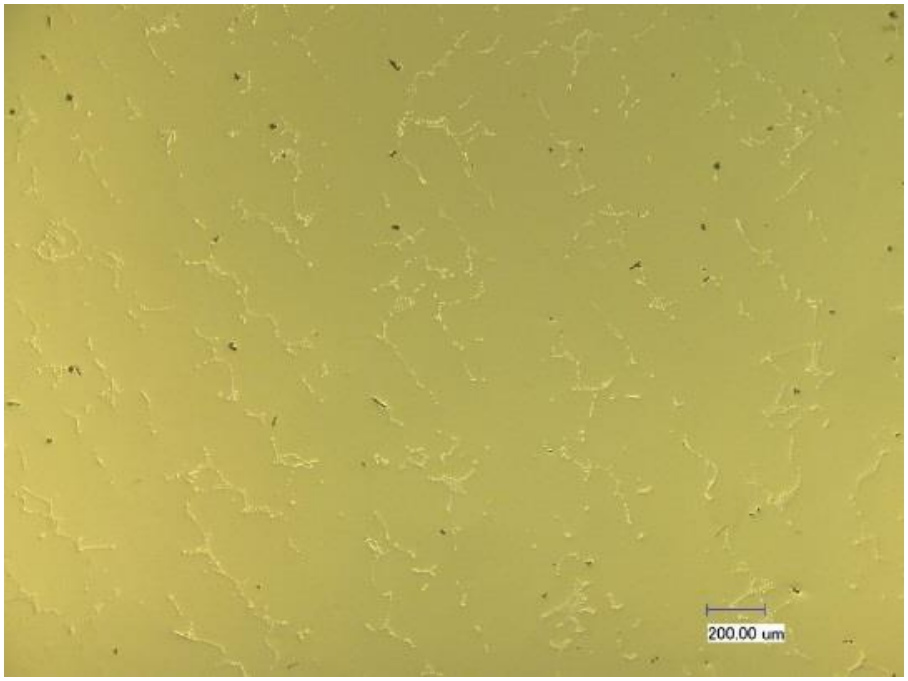

Figure 98-OM image of Alloy 1 [111] single crystalline sample heat treated at 1200°C for 1 hour and water quenched

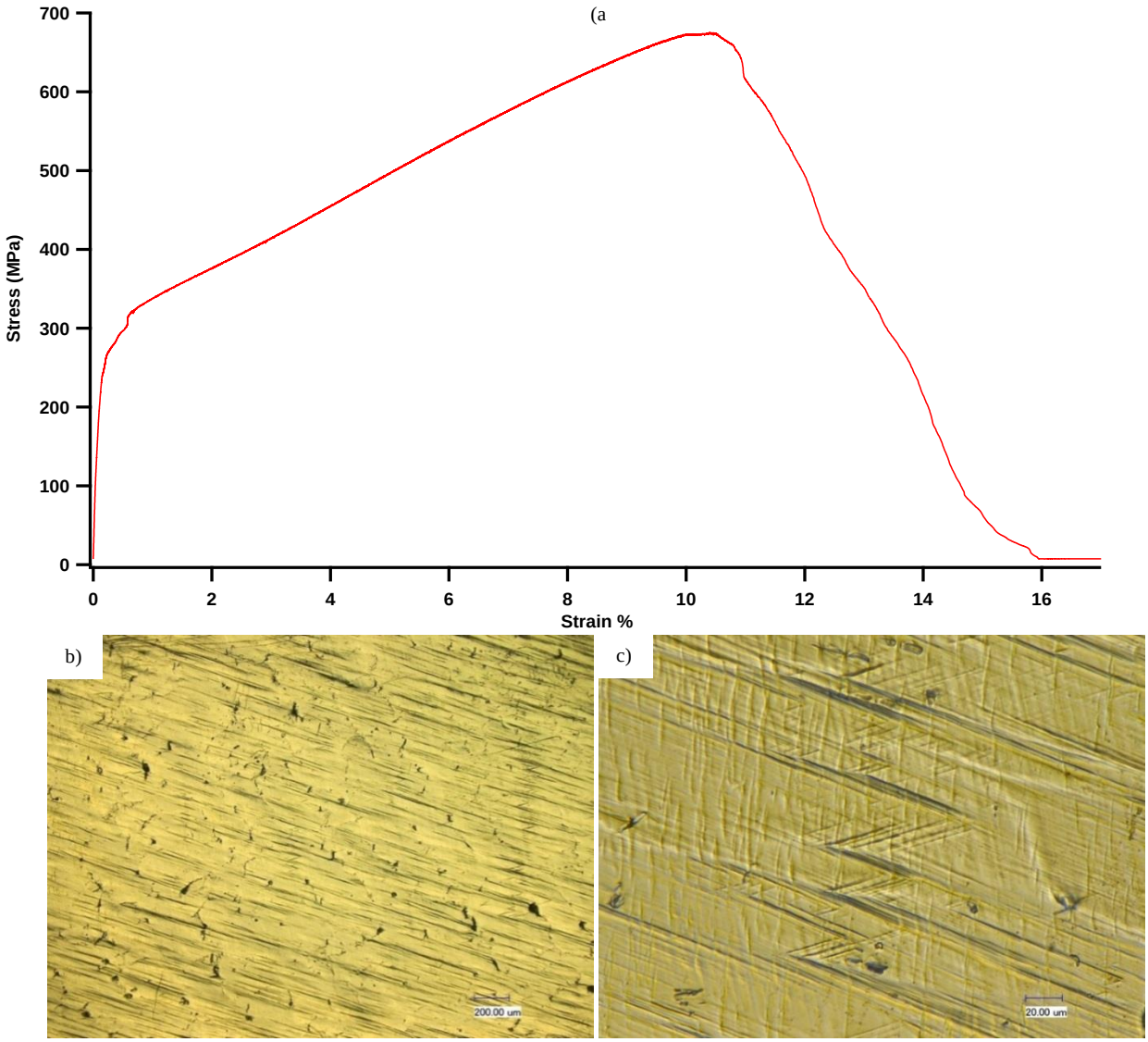

Figure 99- Alloy 1 [111] single crystalline sample heat treated at 1200°C for 1 hour and water quenched: a) stress vs. strain curve of uniaxial tension test to failure, b) and c) OM images after the tensile test

The alloy 1 [111] single crystalline samples that were deformed until fracture were prepared for EBSD analysis. The EBSD mapping of these samples didn't show any sign of the presence of misorientation, even when scanned using a very small 100nm step sizes. This result, as in the case of the polycrystalline alloy 1, may be a consequence of ultra-fine mechanical twining that may show up after heat treatment. Alternatively, trying to impede deformation by slip with methods such as decreasing the temperature may be able to produce twin bands with a detectable size. Single crystalline tensile samples of alloy 1 that had been prepared along their [111] orientation, in order to study the twin-ability of this alloy as the baseline customized alloy, and were previously tested in uniaxial tension test up to fracture at room temperature were studied using EBSD. However, no sign of twinning could be found anywhere in the sample suing EBSD, even after using step sizes as small as 100nm.

To investigate the stress-strain behavior of this alloy single crystal, another uniaxial tension test was performed up to 10% elongation at room temperature (Figure 100-a). Moreover, uniaxial tension tests were also performed at -80˚C and the curves show a significant difference in their yield stress value. While the higher curve for the tension test at -80˚C makes sense, the lower one seems unreasonable as the yield stress is supposed to increase by decreasing the temperature. The sample with this curve was then studied using EBSD (Figure 100-b), which showed that the orientation of the sample is not the assumed [111].

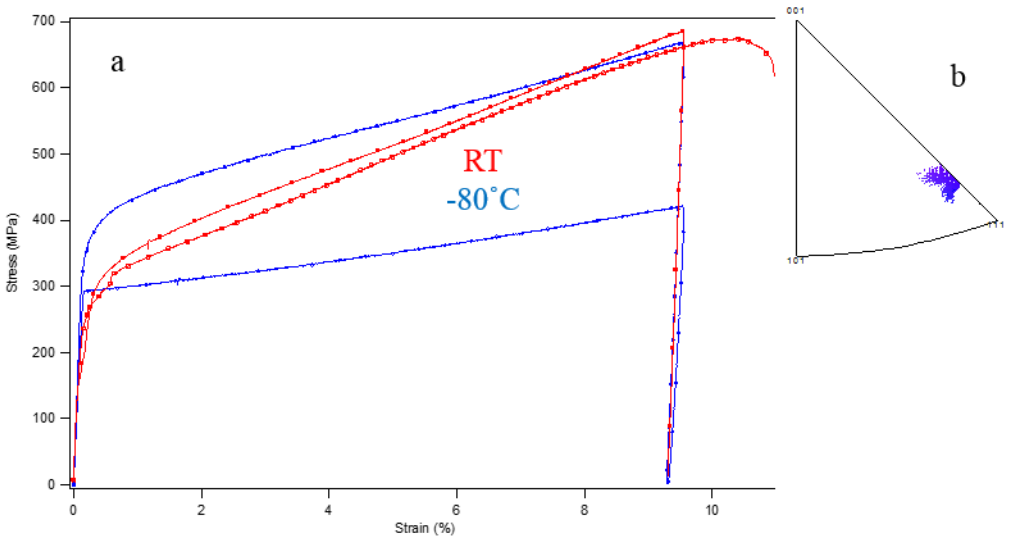

Figure 100- a) Stress vs. strain curve of Al1 [111] single crystals at room temperature an -80˚C

Optical microscopy surface images of the sample deformed at -80˚C are shown in Figure 101, and it can be seen that the surface features, in larger scales, for this sample is more significant than those previously reported for the room temperature tension tests. In smaller scales, the features appear to be more condense and more frequent, hinting that two different mechanisms are at work for different temperatures. A sample of this alloy was tested using uniaxial tension test till-failure at room temperature. The sample was then studied using TEM, in search of deformation twins. The result (Figure 102) shows no sign of twinning. As a result, investigation on this alloy was not continued.

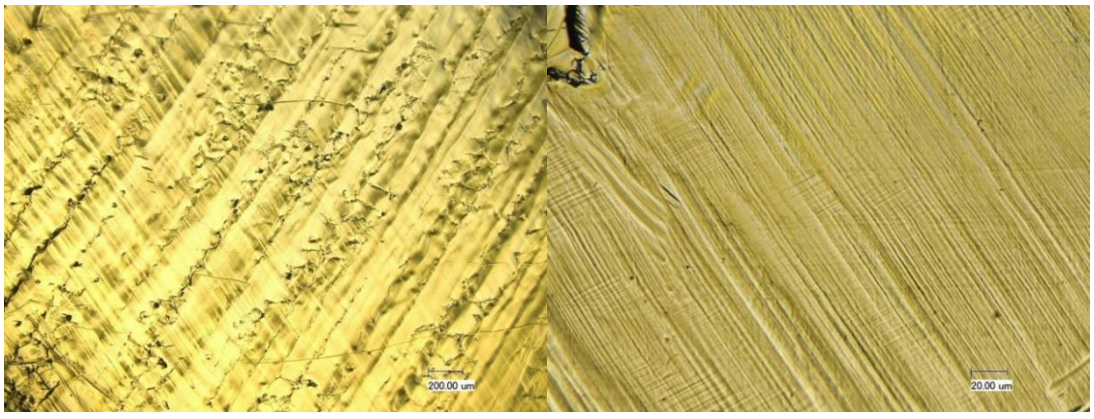

Figure 101- OM of Al1 [111] single crystals deformed 10% at -80˚C

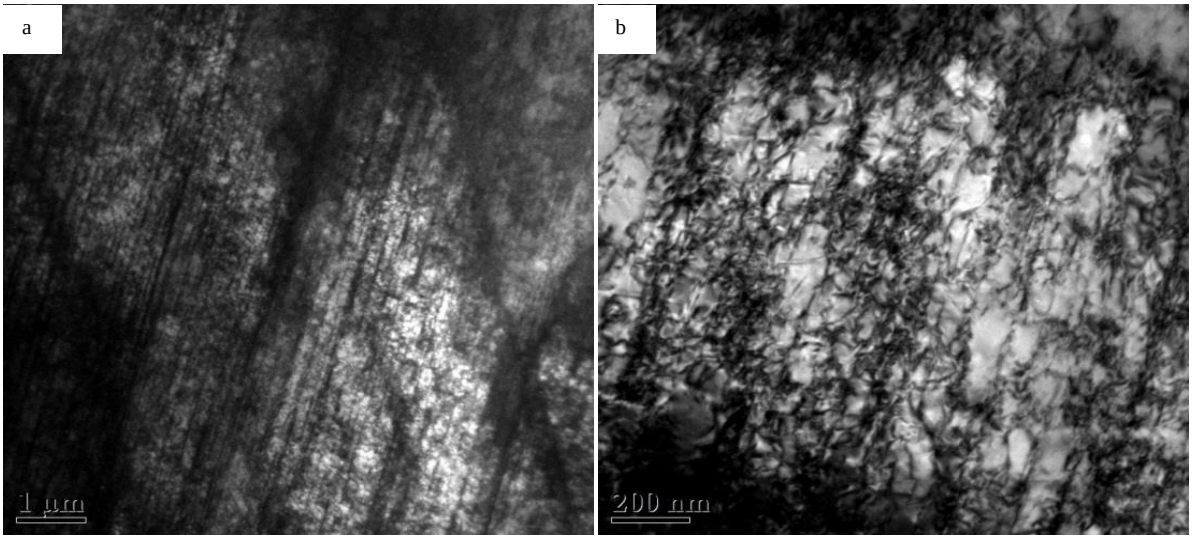

Figure 102-TEM BF image of Al1-[111] single crystal uniaxially elongated till-failure at room temperature

In addition, polycrystalline samples were prepared for uniaxial tension testing. Uniaxial tension tests were carried out with different displacement rates to investigate the effect of the deformation rate. Figure 103 shows optical microscopy images before the tension test. Precipitates can be seen in the samples as well as different grains, and in some locations, 1-10 µm wide rectangular grains that appear to be annealing twin bands.

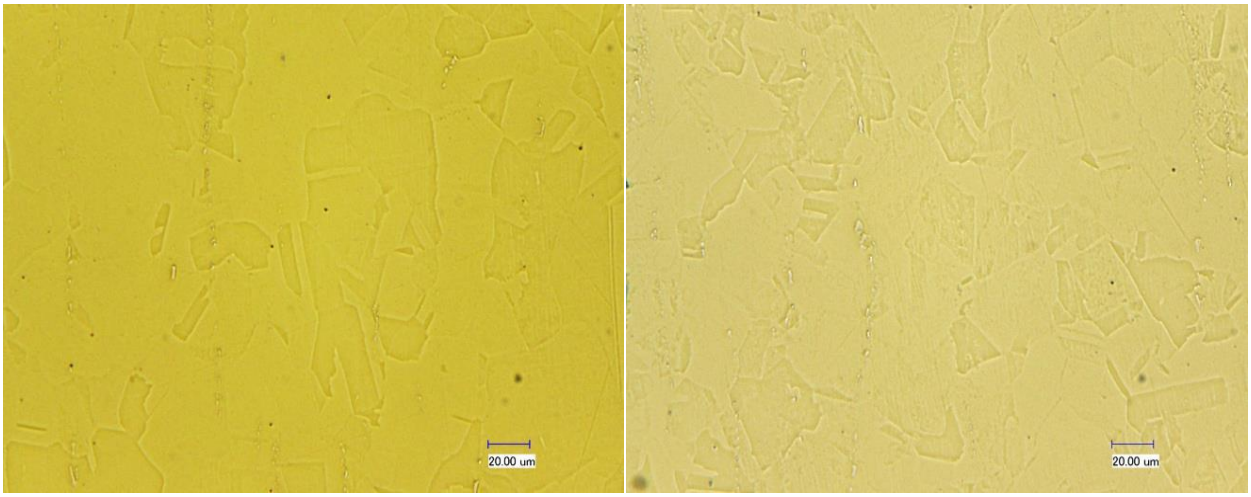

Figure 103-OM of Al1 polycrystalline sample

Figure 104 shows the stress-strain curves for different displacement rates, and as it can be seen, the work hardening exponent is independent from the displacement rate, indicating that the major deformation mechanism is not dislocation slip. Figure 105 shows optical images from the surface of the samples tested in the uniaxial tension test with different displacement rates. No significant difference is observable in the surface features created by deformation with different displacement rates, supporting the theory that deformation mechanism is not dislocation slip.

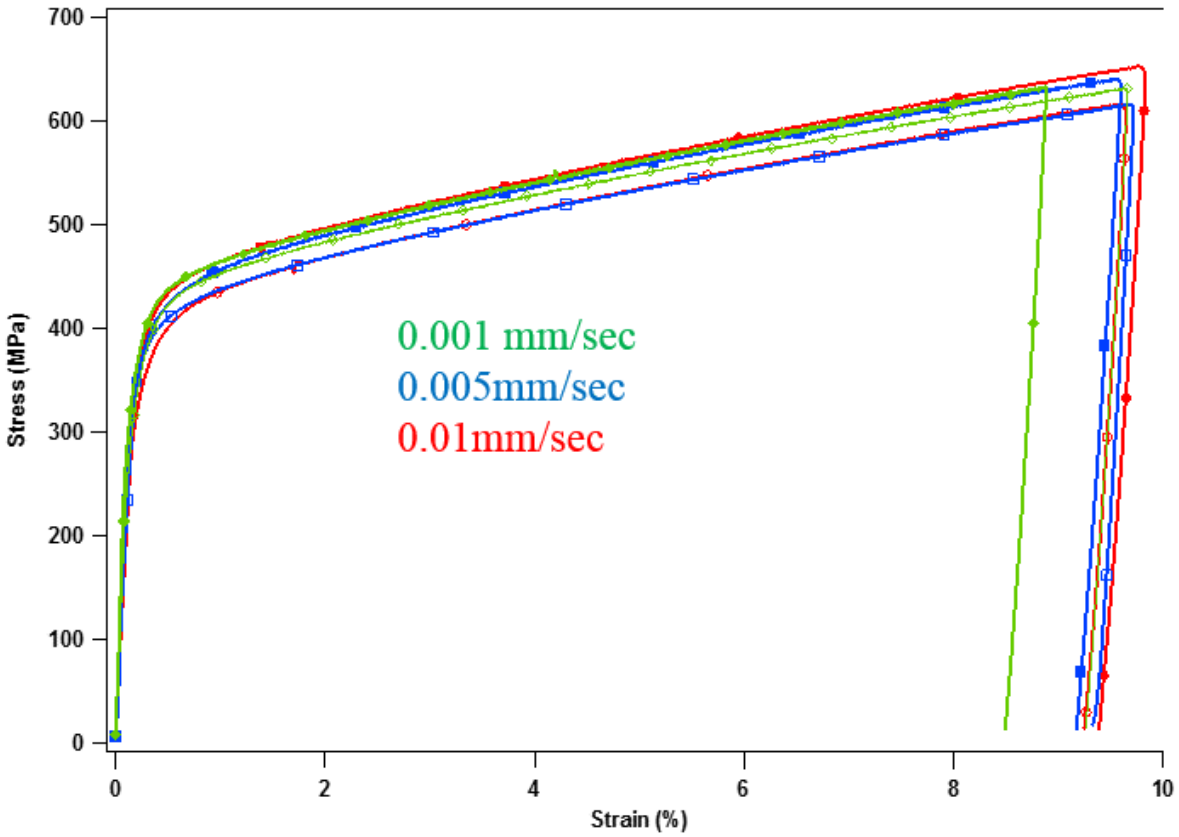

Figure 104-Stress strain curve of Al1 poly-crystalline samples with different displacement rates

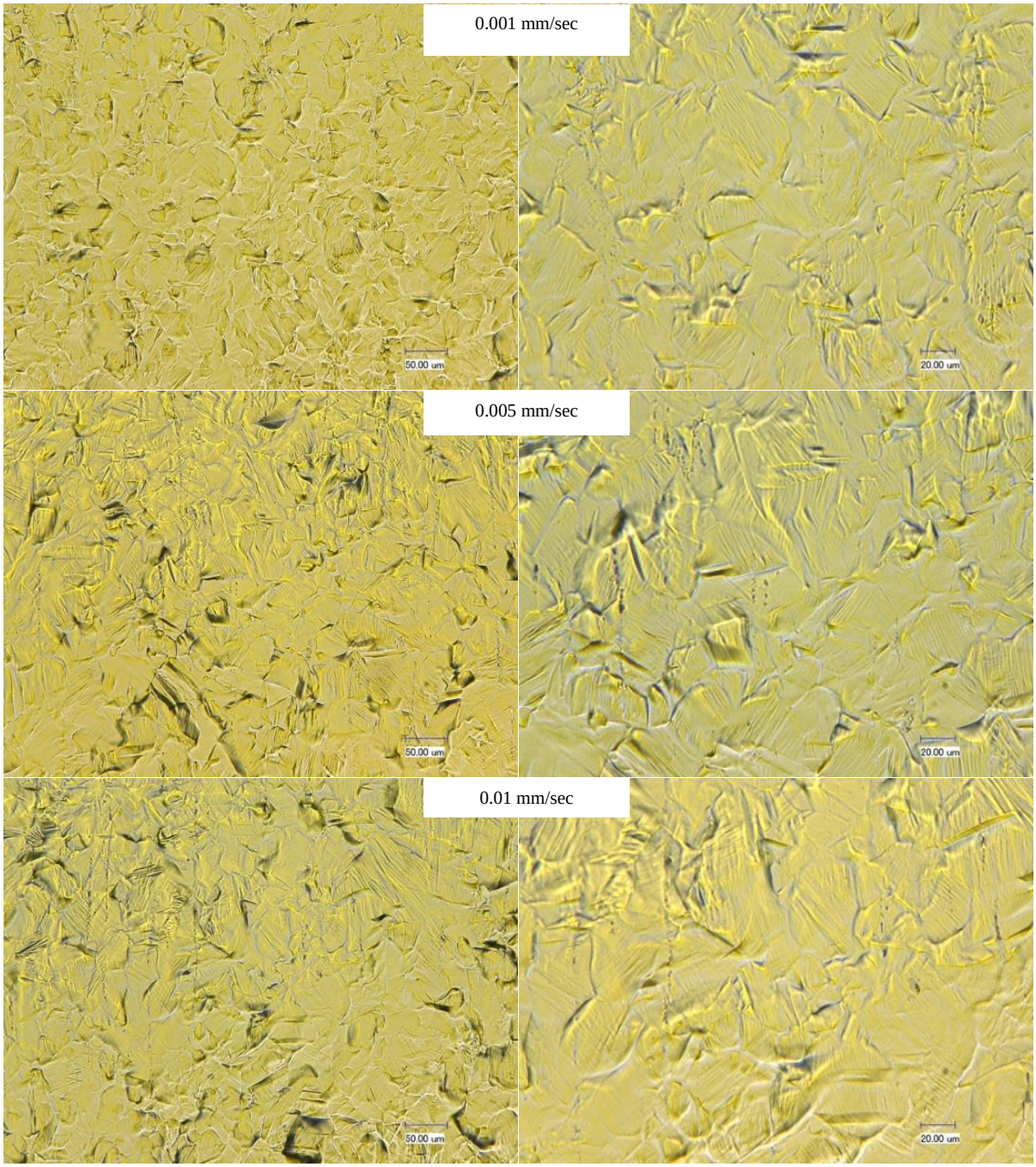

Figure 105-OM images of poly-crystalline Al1 samples after 10% elongation at room temperature with different dis-placement rates

b) Alloy 2

The as-received condition for this batch (Al2) was reported to be arc melted, where the material had a two phase structure. To homogenize the microstructure, the as received Al2 was cold rolled for 80% reduction in thickness at room temperature followed by solution heat treatment at 1200°C for 1hr. OM images of the cold rolled samples (Figure 106-a) show a typical elongated

microstructure along the rolling direction. Figure 106-b shows the microstructure after the homogenization. The homogenized microstructure is successfully obtained together with some annealing twins and precipitates. To identify the crystal structure of the homogenized microstructure, XRD was performed. Figure 107 suggests that both ferrite and austenite coexist in the microstructure. Since a fully austenitic structure is desired in this work, the efforts will be directed towards removing the ferrite through thermo-mechanical treatments. Unfortunately, based on the calculated phase diagram, no feasible temperature range exists for single austenite phase as indicated in Figure 108.

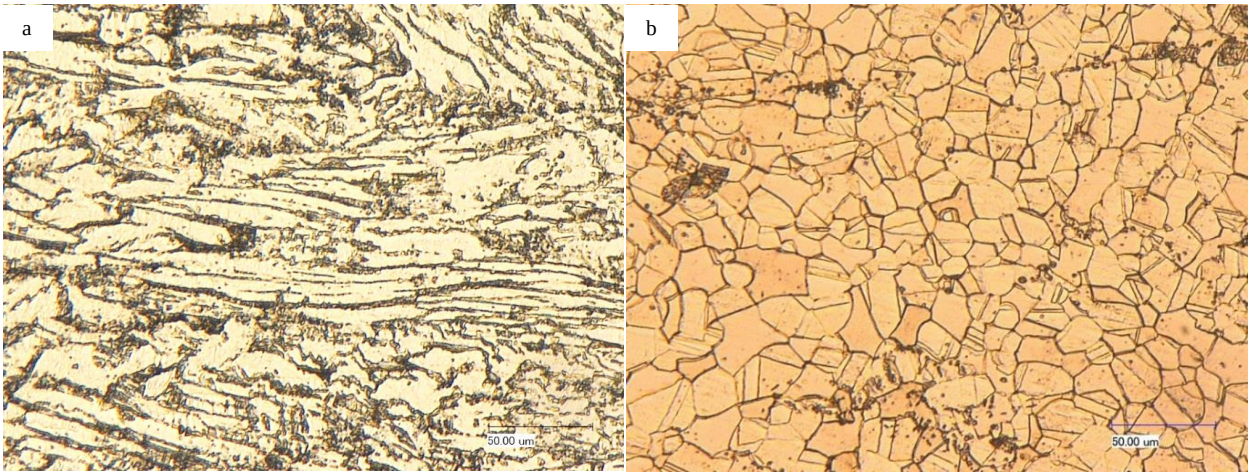

Figure 106- The OM image of the Al2 samples after cold rolling to 80% thickness reduction at room temperature (a), and after cold rolling plus solution heat treatment at 1200°C for 1hr (b).

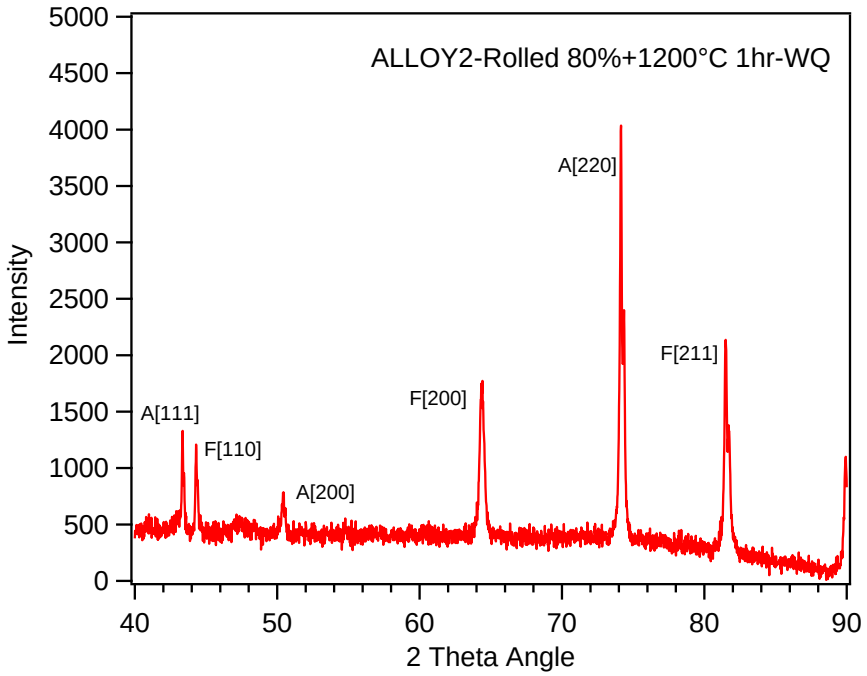

Figure 107- XRD spectrum of the Al2 sample after cold rolling plus solution heat treatment showing a two phase structure.

a

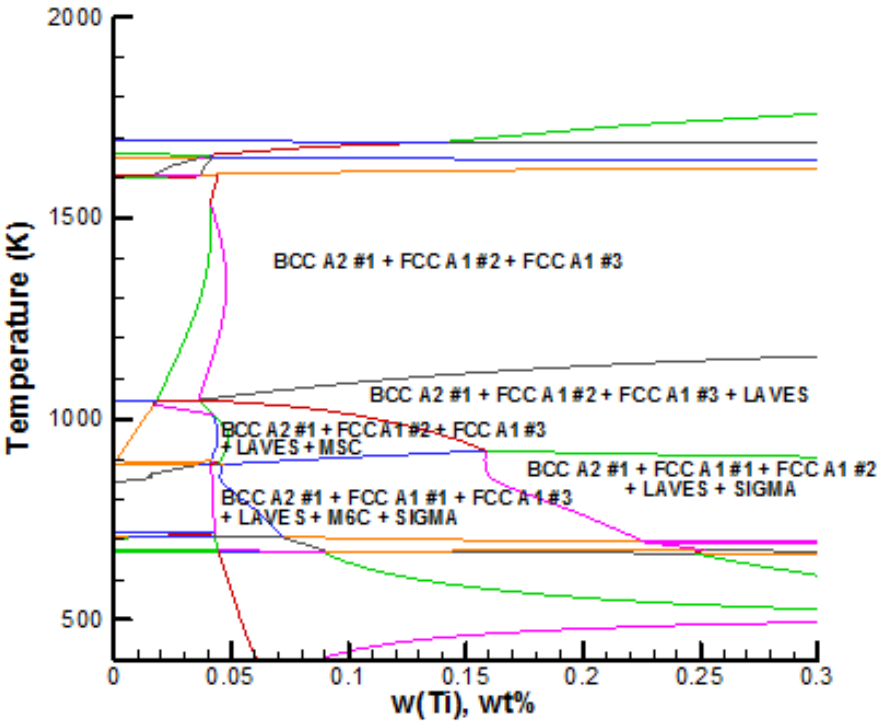

b

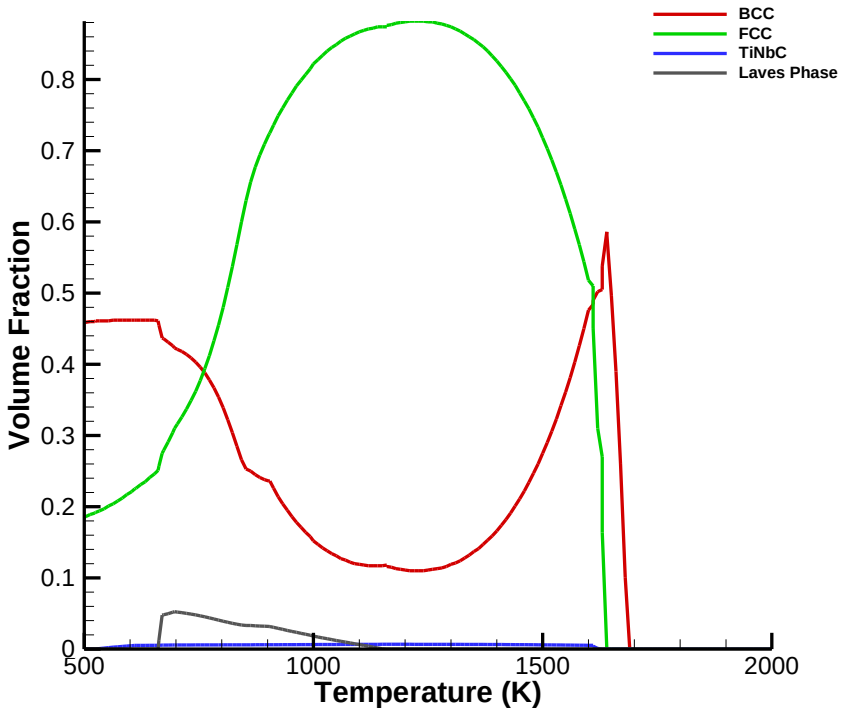

Figure 108- Calculated Phase Diagram (a) and Volume Phase Diagram (b) of Alloy 2 showing the lack of a single phase region.

In order to determine the composition of the precipitates, SEM with EDS and WDS analyses were carried out on the cold rolled plus heat treated samples. The BSE image in Figure 109-a shows grains with different orientations, as well as bright precipitates. The EDS spectrum of the bright precipitates (circled in Figure 109-a) indicates that the precipitates contain mostly Nb and Ti (Figure 109-b). Recall that Al2 contains both C and N, WDS analysis was further performed to find out whether the precipitates are carbides or nitrides. Figure 109-c show the energy spectrum obtained from WDS spectrometry rotation. O, N, and C Kα positions are marked by the colored lines. It is obvious that the examined precipitate is carbon rich without any indication of N or O in it. Thus, it can be concluded that the precipitates in the homogenized Al2 are (Nb,Ti) carbides.

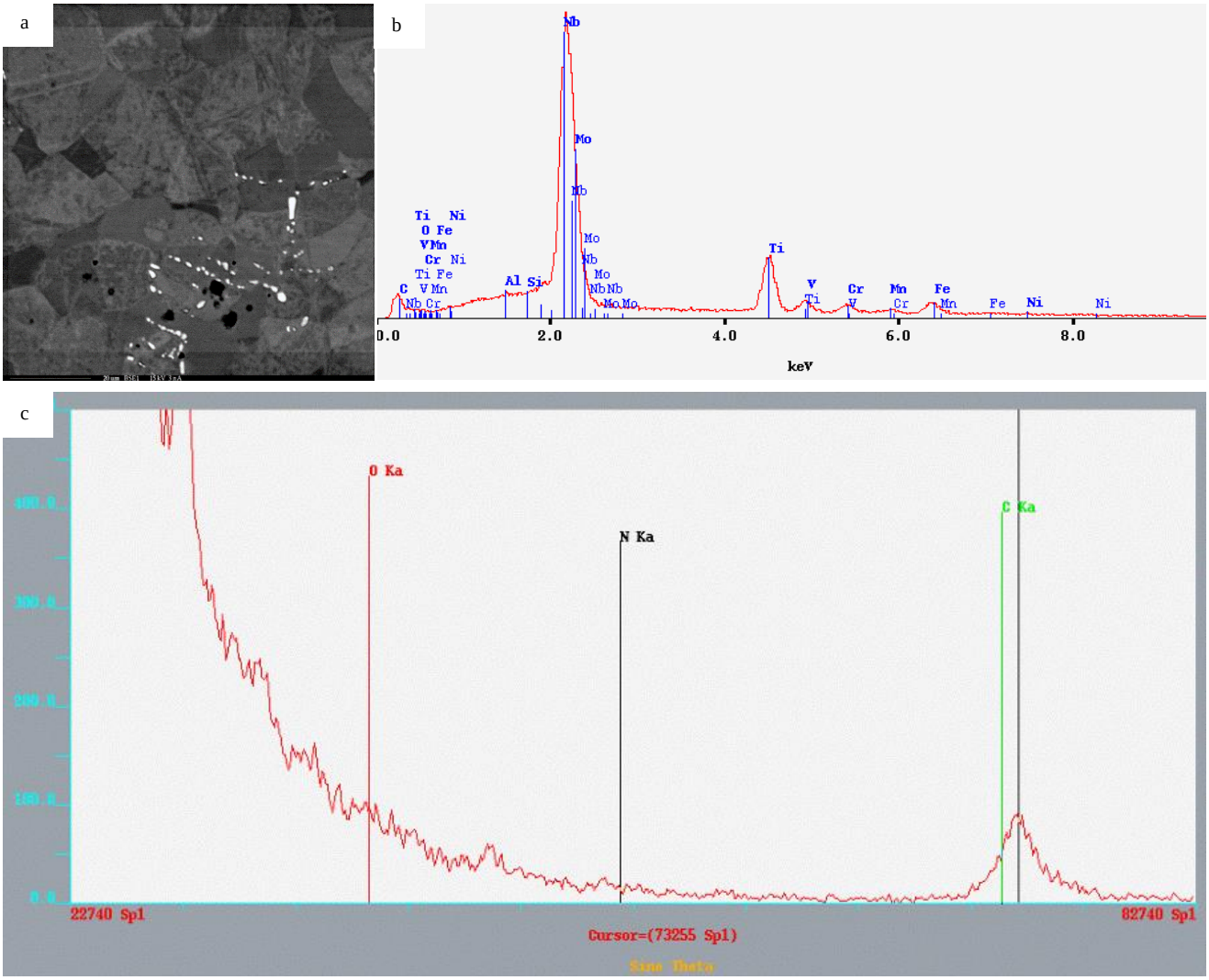

Figure 109- BSE image of the cold rolled plus heat treated Al2 sample with bright precipitates (a), EDS spectrum (b) showing the chemical composition of the precipitates circled in (a), and the energy spectrum of the precipitate obtained from WDS spectrometry rotation showing that the precipitate is carbide (c).

c) Alloy 3

The as-received condition for this batch (Al2) was reported to be arc melted. Similar to Al2 samples, in order to obtain a homogenized structure, the as received Al3 samples were cold rolled to 80% thickness reduction at room temperature followed by 1200°C solution heat treatment for 1hr and water quenched. Figure 110-a shows the microstructure after cold rolling and heat treatment. Second phases exists as in the Al2 samples as indicated by the dark inclusions and small dots in the figure. The XRD spectrum indicates that after homogenization treatment, austenite dominates the microstructure and no ferrite exists (Figure 110-b).

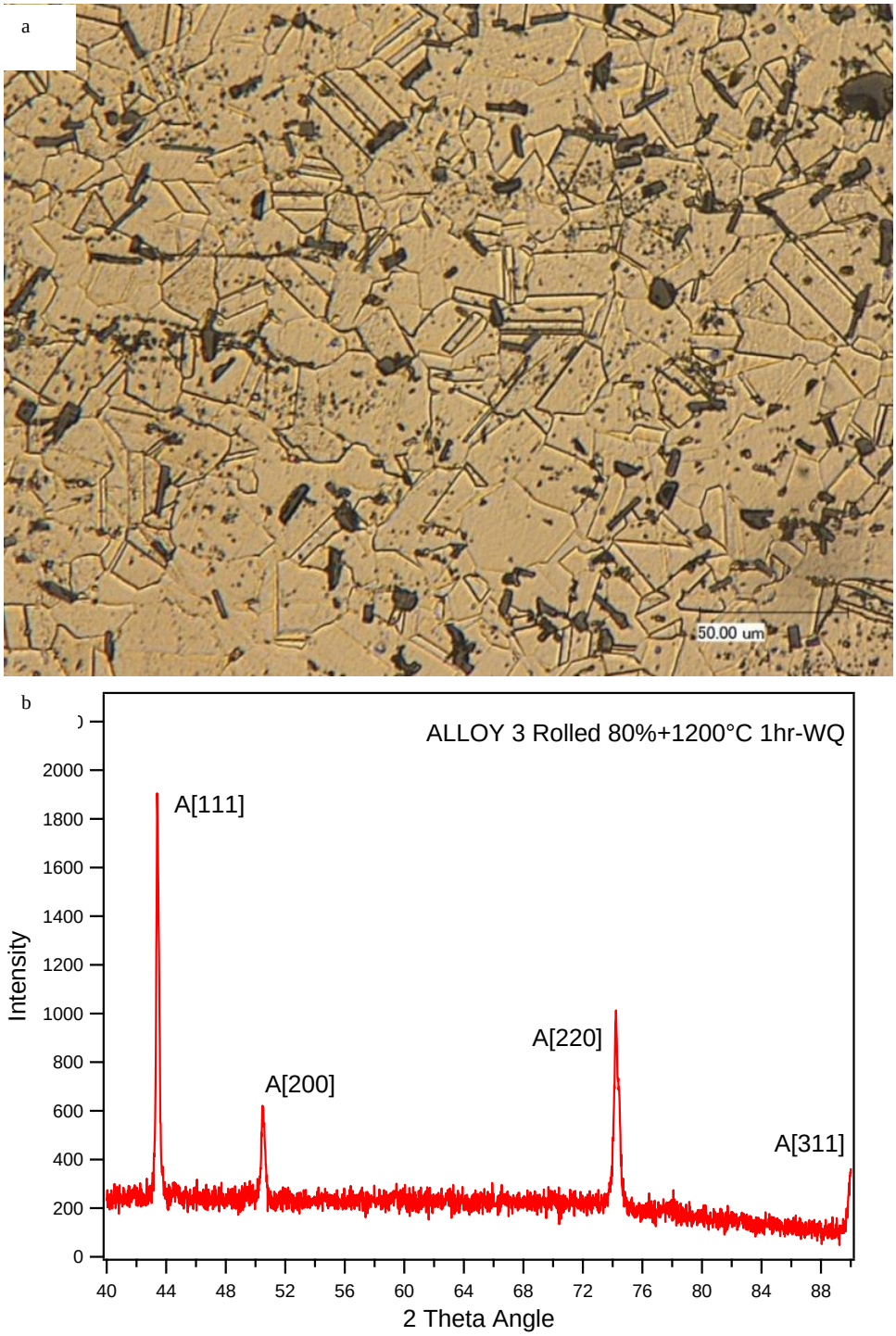

Figure 110- The OM image of the Al3 samples after cold rolling to 80% thickness reduction at room temperature followed by solution heat treatment at 1200°C for 1hr (a). The XRD spectrum of the same sample (b) showing mainly austenite phase

To identify the type of second phase particles, the samples after cold rolling and solution heat treatment was studied using SEM with EDS and WDS. Figure 111-a shows the BSE image of the sample. The particles show different tones of gray, which indicates that multiple second phase

particles exist in the microstructure. To validate this, EDS and WDS were performed on three representative regions, as marked in the figure. Region 1 represents very dark precipitates, region 2 is grey precipitates, and region 3 is bright precipitates. Figure 111-b-d show the EDS spectrums of regions 1, 2 and 3, respectively. The dark precipitates in region 1 are clearly Al rich. The gray precipitates (region 2) are rich in Ti with some Nb. The bright precipitates (region 3) also contain mainly Nb and Ti, but the Nb is richer than Ti in these precipitates. Considering that both C and N exist in the alloy, WDS analysis was performed on the same regions to identify whether these precipitates are carbides or nitrides. Similar to the method described for the Al2 samples, the WDS spectrometry rotation was applied to detect the O, C and N in the precipitates. Figure 111-e-f show the WDS energy spectrum of regions 1, 2, and 3, respectively. It can be observed that region 1 (Figure 111-e) is N rich, indicating the dark precipitates are probably Al Nitride. In region 2 (Figure 111-f), both N and C exist, with N richer than C. This means that the composition of these gray precipitates is a complicated carbo-nitride containing Ti and Nb. In region 3 both N and C are detected, with much less N as compared to region 2. The presence of both N and C indicates that the bright precipitates are also a carbo-nitride with Nb and Ti. The difference between regions 2 and 3 lies in the relative concentration of Ti and Nb.

Alloy 3 (Al3) as previously reported, is fully austenite at room temperature after a homogenization process at 1200˚C for 1 hour followed by water quenching. Initial Wavelength-Dispersive X-Ray Spectroscopy (WDS) previously reported showed the presence of precipitates consisting of Aluminum nitrides, and Titanium and Niobium carbo-nitrides. Further investigation using Energy-dispersive X-ray spectroscopy (EDS) showed (Figure 112) that the precipitates are either rich in Aluminum, or rich in other alloying elements such as Niobium, Titanium, Molybdenum and Vanadium. The fact that these elements are concentrated in the precipitates and not dispersed in the matrix makes it more probable for deformation twinning, Alumina scale formation, and precipitation strengthening mechanisms to happen.

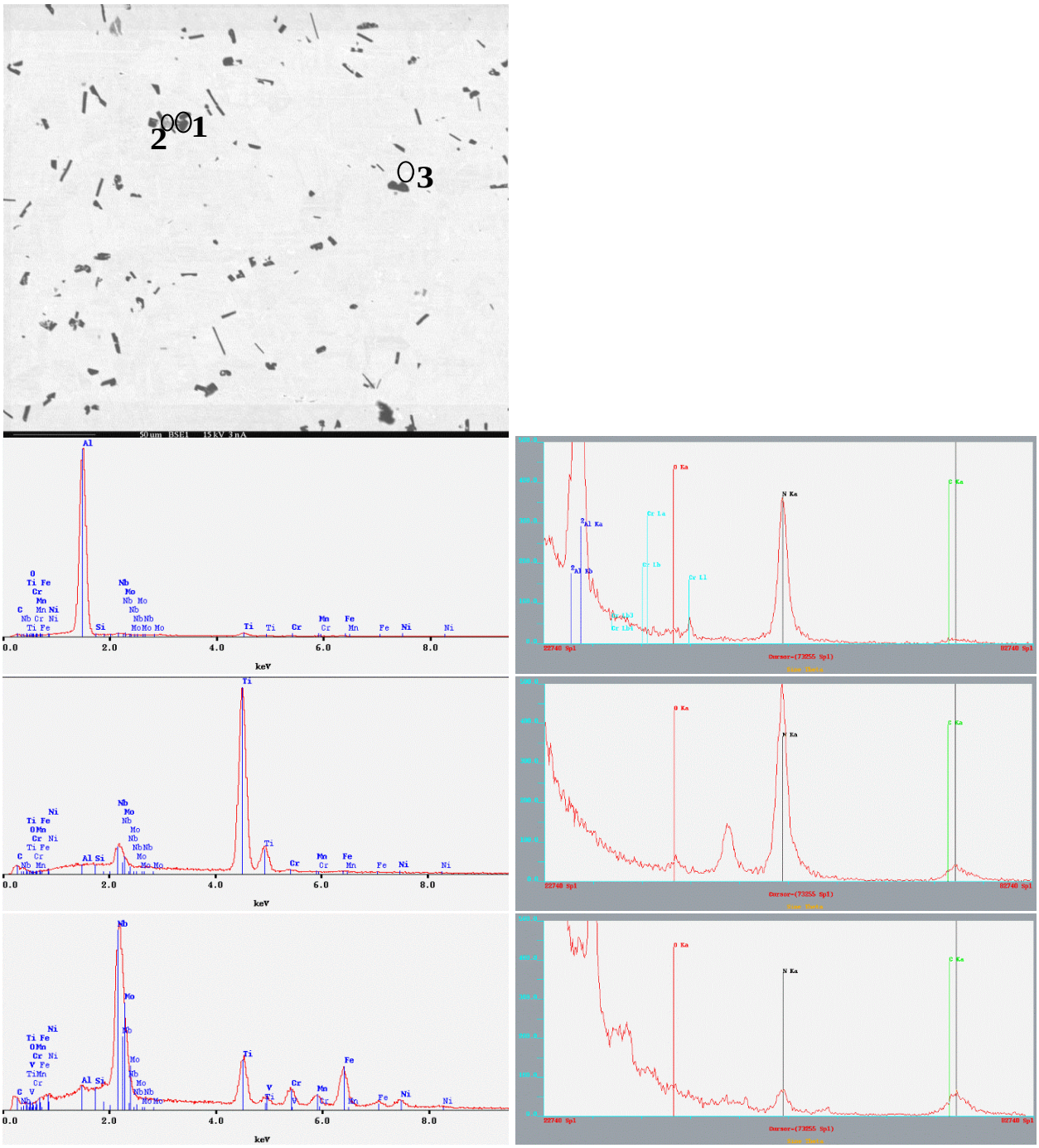

Figure 111- The BSE image of the Al3 samples after cold rolling to 80% thickness reduction at room temperature followed by solution heat treatment at 1200°C for 1hr (a), showing the existence of multiple precipitates, as marked by regions 1, 2, and 3. Corresponding EDS spectrums (b-d) and WDS spectrums (e-g) from the regions 1, 2, and 3, respectively.

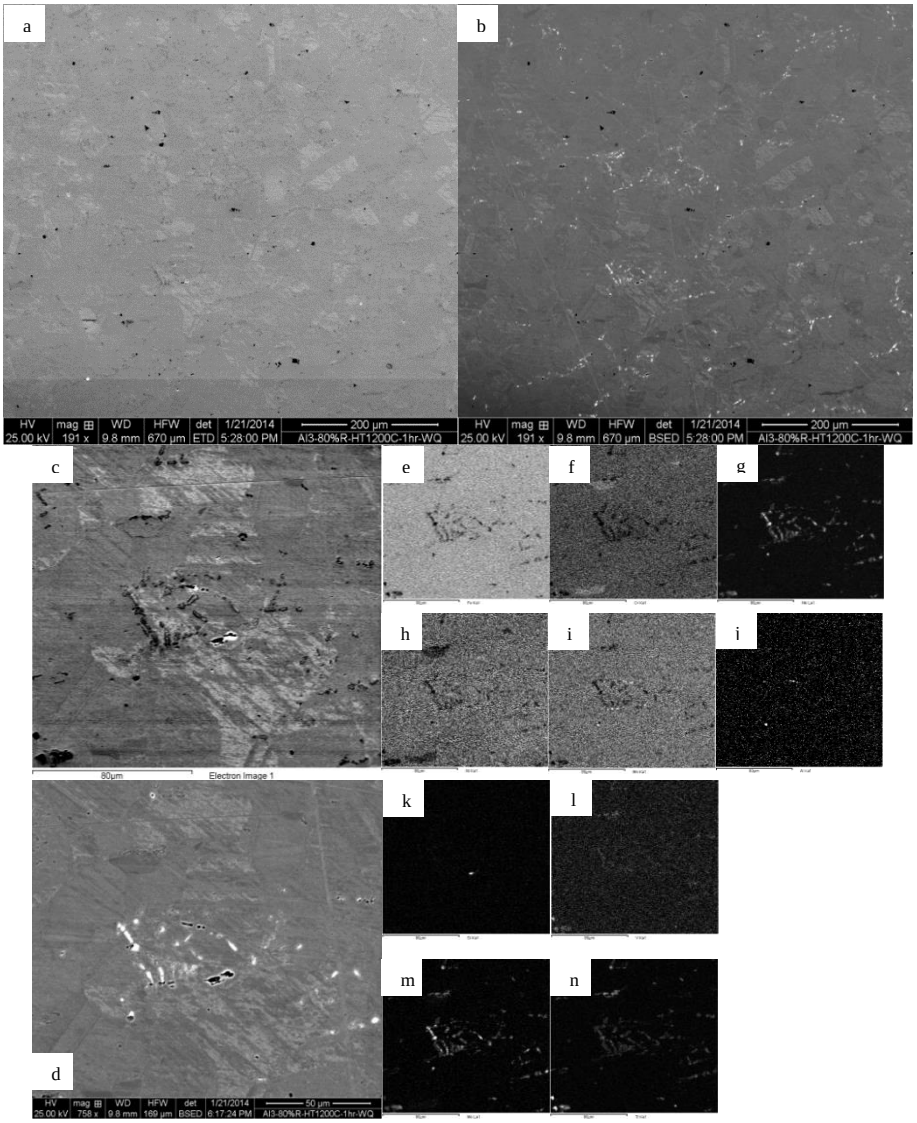

Figure 112-Al3 after being cold rolled for 80% reduction in area, a) surface SEM, b) surface BSE, c) precipitate SEM, d) precipitate BSE, e) Fe, f) Cr, g) Nb, h) Ni, i) Mn, j) Al, k) Si, l) V, m) Mo, n) Ti

d) Proposed Genetic Algorithm Alloys (PGAA)

Figure 114-a shows the as-received structure of this alloy. Initial BSE image shows a dual structure existing, which is expected from a regularly cast metal. As it can be seen in Figure 114-b to f, the EDS maps show that there are two types of second phase particles: one is richer in Mn a Mo, and the other is rich in Al. Both types are almost void of other elements, that is, Cr, Fe, and Ni. Moreover, these maps show that the dual phase structure of the matrix has slightly different amounts of Cr, Ni, and Mo. Next, we have tried to homogenize the microstructural homogeneities in this alloy and prepare it for mechanical and oxidation tests. Figure 115-a shows the load vs. stroke curve during this extrusion (red curve). Figure 115-.b is an image of the extruded sample. The failure of this extrusion resulted in two other experiments. Two ingots were heated to 1050°C

and kept for 30 minutes, and then were extruded with 1inch/sec and 0.5 inch/sec rates. The trend, as seen in Figure 115-c and d, suggests that decreasing the temperature and decreasing the strain rate will improve the extrusion. As a result, ingots were heat treated at 1200°C in controlled atmosphere for 50 hours, to solutionize the different second phase particles as much as possible. The solutionized ingots were expected to have a single phase structure, and thus, a slower extrusion rate at lower temperatures should have been successful. However, the structure achieved after this heat treatment, shown in Figure 116 also demonstrates two phase structure, but the size of the second phase particles have decreased. Later, an investigation into the theoretical phase diagram of this alloy calculated using ThermoCalc (Figure 113) shows no thermally stable single phase austenite exists. This fact, combined with the poor formability of this alloy during ECAE, makes it a discouraging candidate, since the study of both alumina-formation and twinning were proposed in a fully austenitic matrix.

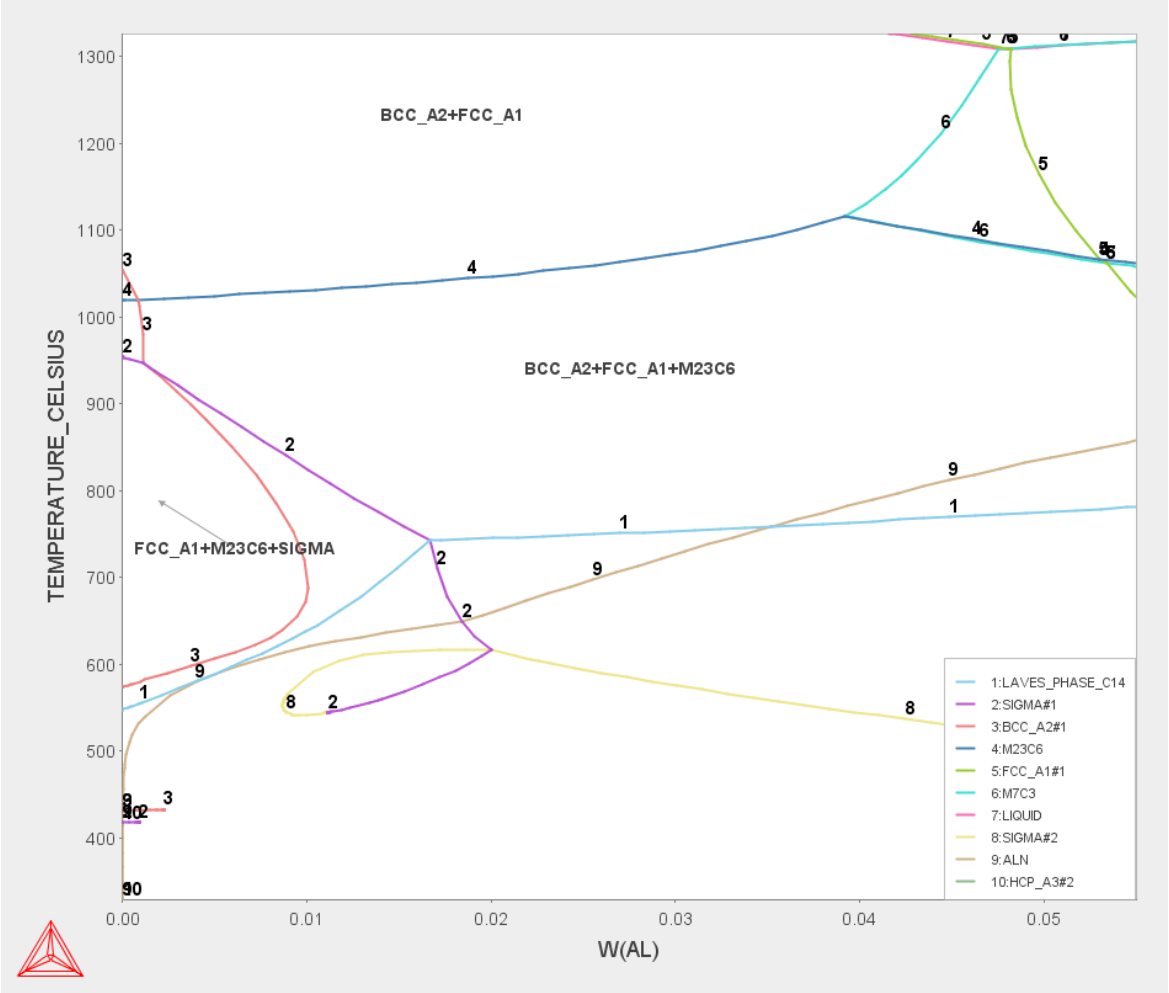

Figure 113- Theoretical phase diagram of PGAA1, temperature vs. weight fraction of Al

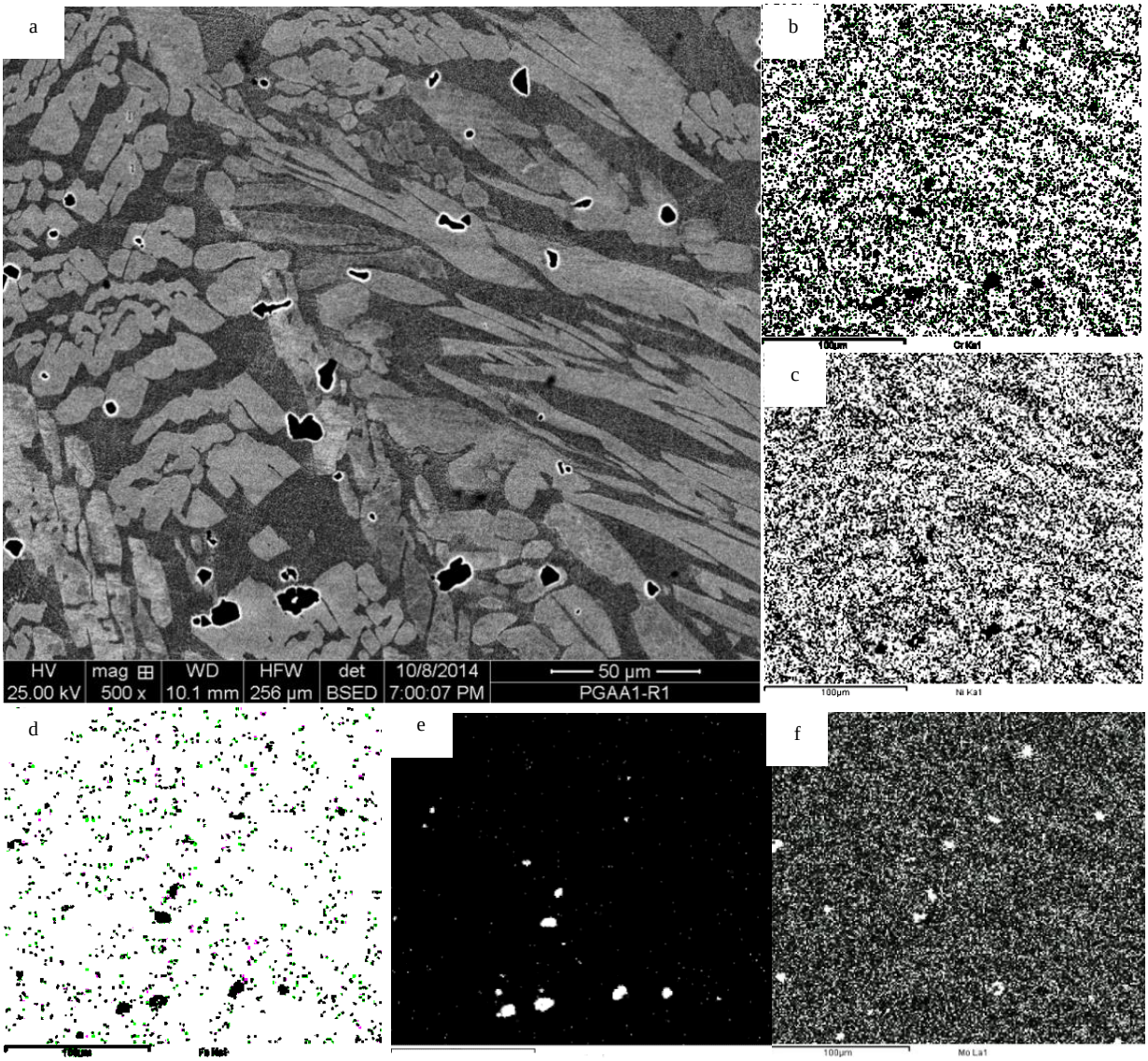

Figure 114-BSE image (a), and EDS maps (b-g) of the as-cast PGAA1 alloy showing elemental distribution of b)Cr, c)Ni, d)Fe, e)Al, f)Mo

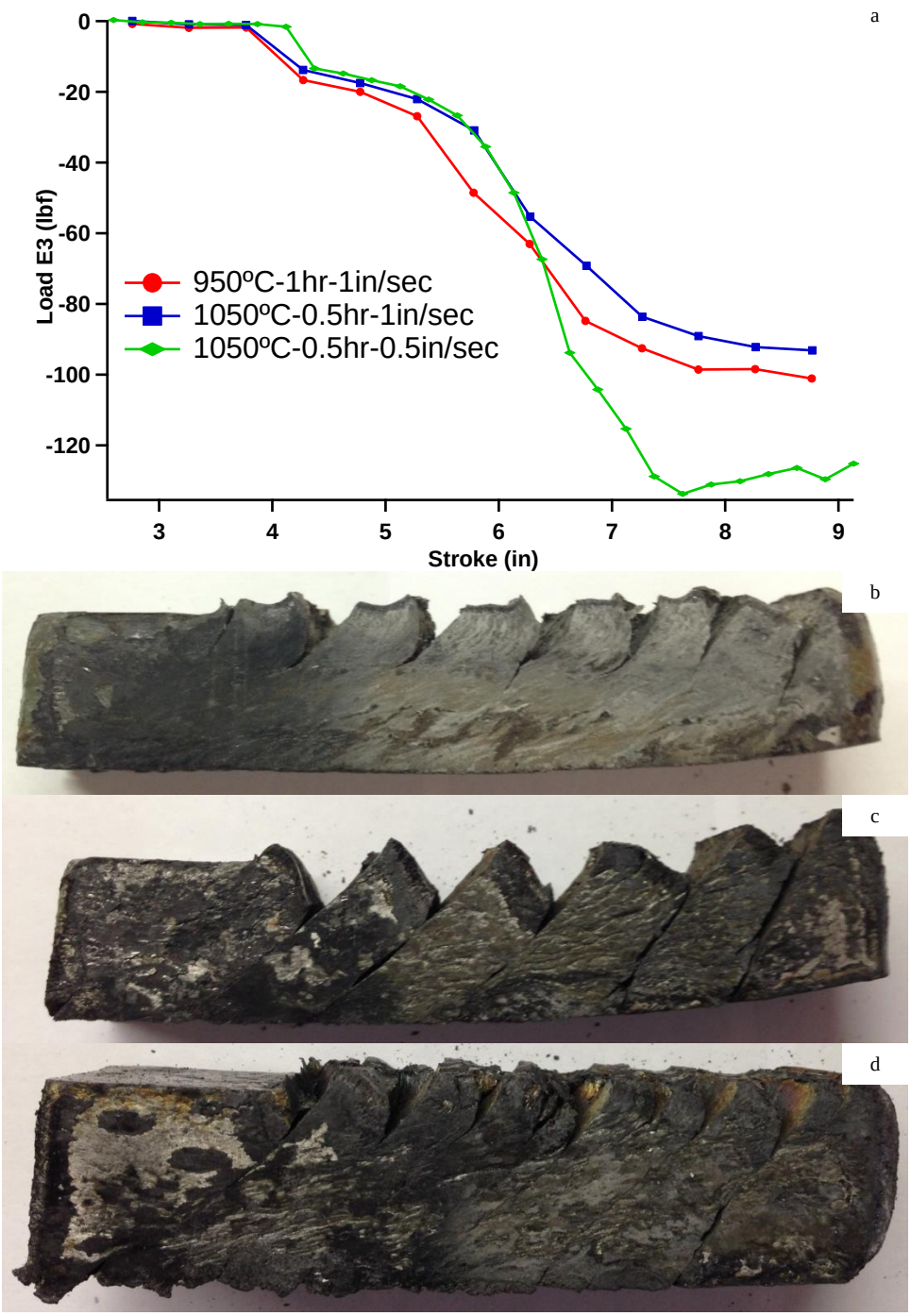

Figure 115- (a) Load vs. stroke diagram of ECAE processing of PGAA1 alloy, b) ingot after ECAE at 950˚C-1hr with an extrusion speed of 1in/sec, c) ingot after ECAE at 1050˚C-0.5hr with an extrusion speed of 1in/sec, d) ingot after ECAE at 1050˚C-0.5hr with an extrusion speed of 1in/sec, d) ingot after ECAE at 1050˚C-0.5hr with an extrusion speed of 0.5in/sec

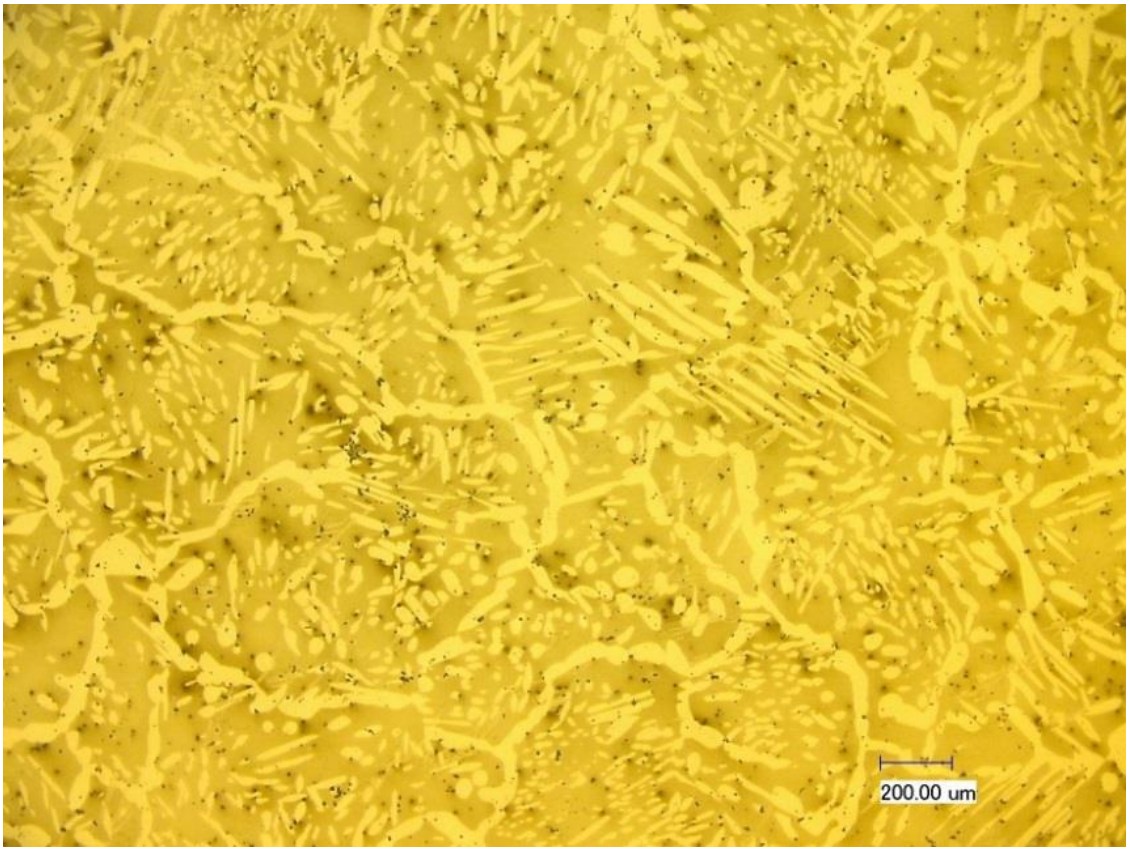

Figure 116-OM image of the PGAA1 alloy after heat treatment at 1200˚C for 50 hours at controlled atmosphere followed by water quenching

PGAA2, meeting both the alumina-formation as well as the theoretical single phase austenite (Figure 117) criteria, is a promising candidate for the present study. This alloy was, too, heat treated at 1200°C for 50 hours at an inert atmosphere, and the obtained microstructure, as depicted in Figure 118-a, shows a mostly homogenized structure. The precipitates seen in the figure are the two previously observed Al-rich and (Mn,Mo)-rich particles, as it can be seen from the BSE image and corresponding EDS maps shown in Figure 118-b to e.

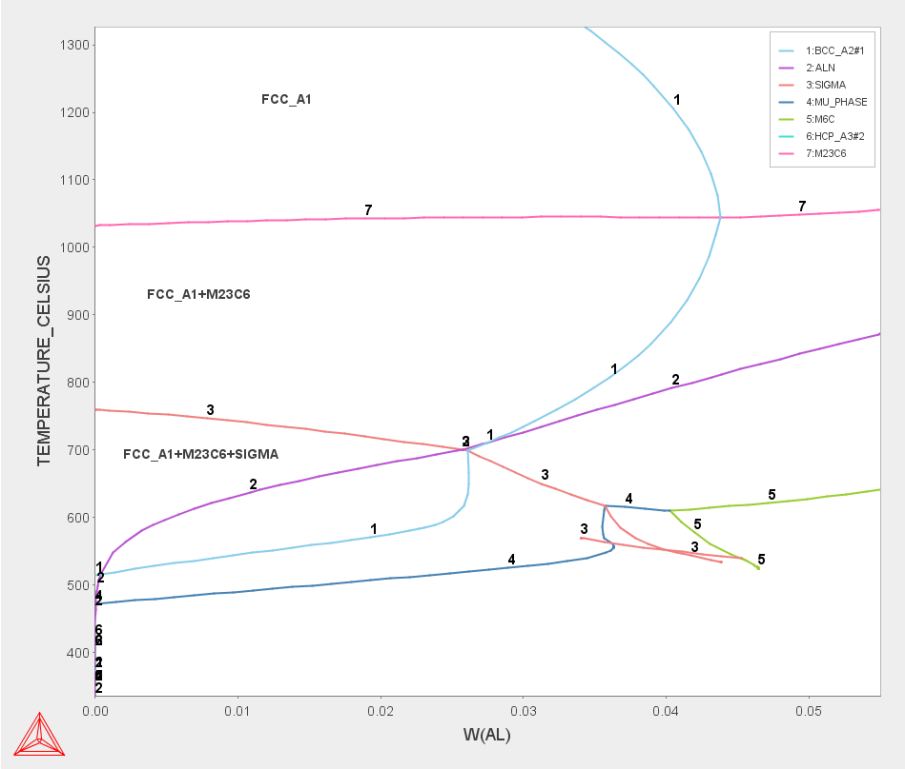

Figure 117- Theoretical phase diagram of PGAA2, temperature vs. weight fraction of Al

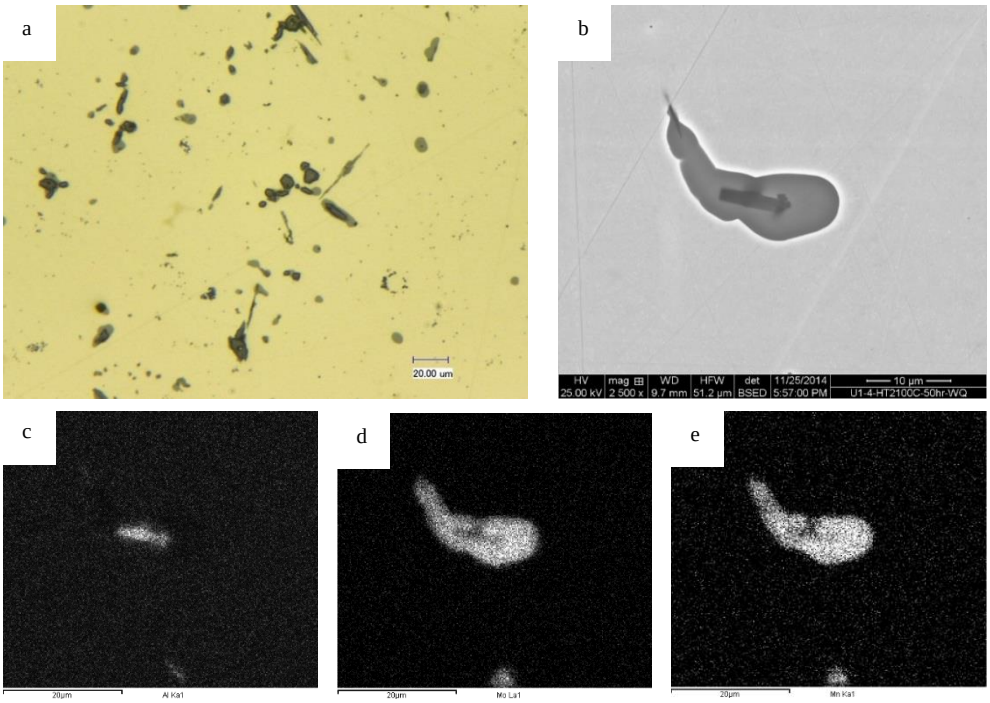

Figure 118- OM image of PGAA2 after heat treating at 1200°C for 50 hours, b) BSE image of a precipitate in the sample, and EDS maps showing distribution of c) Al, d) Mo, and d) Mn

Figure 119 shows that the as-cast structure of these alloys is heavily dendritic, as expected. The sample was then used for further investigation using WDS (Figure 120), and based on the results, region 1 and 2 have the same composition with different orientations. Region 3 is a precipitate, richer in Al, Mo, and Cr but has less Ni, and region 4 is highly rich in Al, and contains nitrogen, and is probably an aluminum nitride precipitate with sharp edges. Next, we will try to homogenize this alloy.

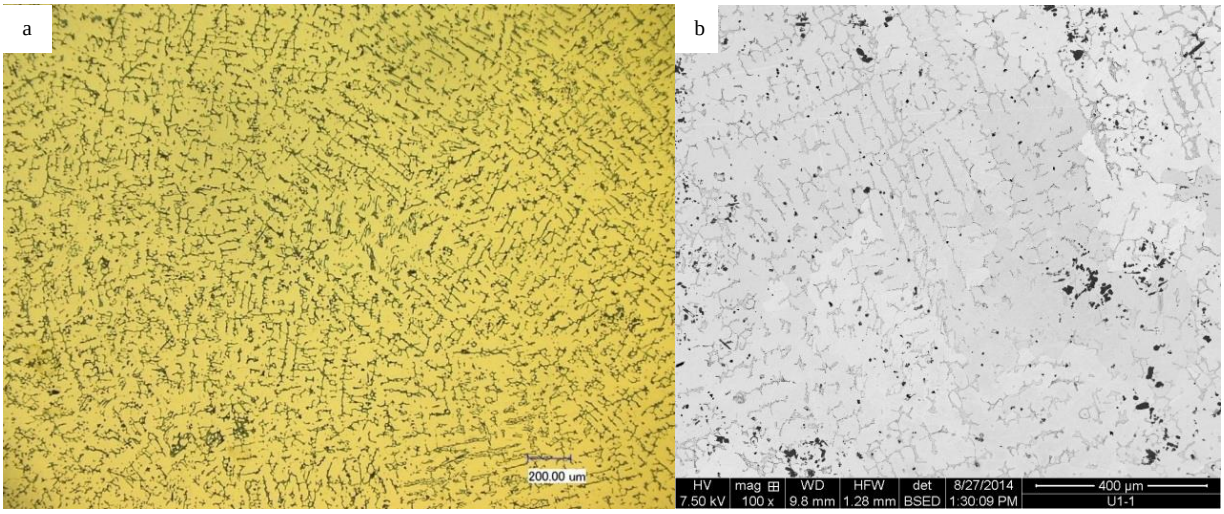

Figure 119- PGAA2 as-cast alloy (a) OM, and (b) BSE images

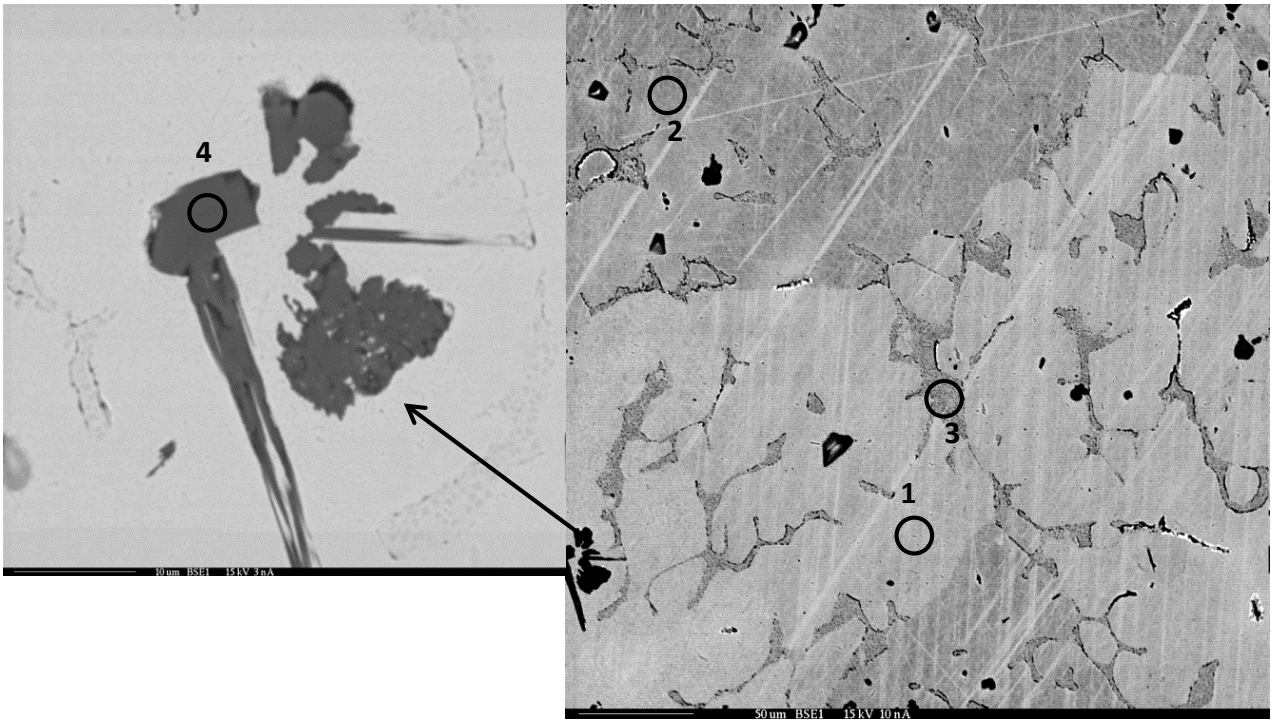

Figure 120- BSE image of PGAA2 alloy showing the regions analyzed with WDS

In an attempt to dissolve these precipitates, a sample of this bar was heat treated at 1300°C for 1 hour in vacuum then water quenched. Figure 121 is the OM image of the sample, illustrating evolution of a continuous phase along the grain boundaries. The sharp corners of this second phase suggests that it is aluminum nitride. The other spherical precipitates also still persist. Presence of impurities such as Nitrogen and Sulfur prevents dissolution of the particles. As a result, this 1300°C heat treatment is deemed unfavorable.

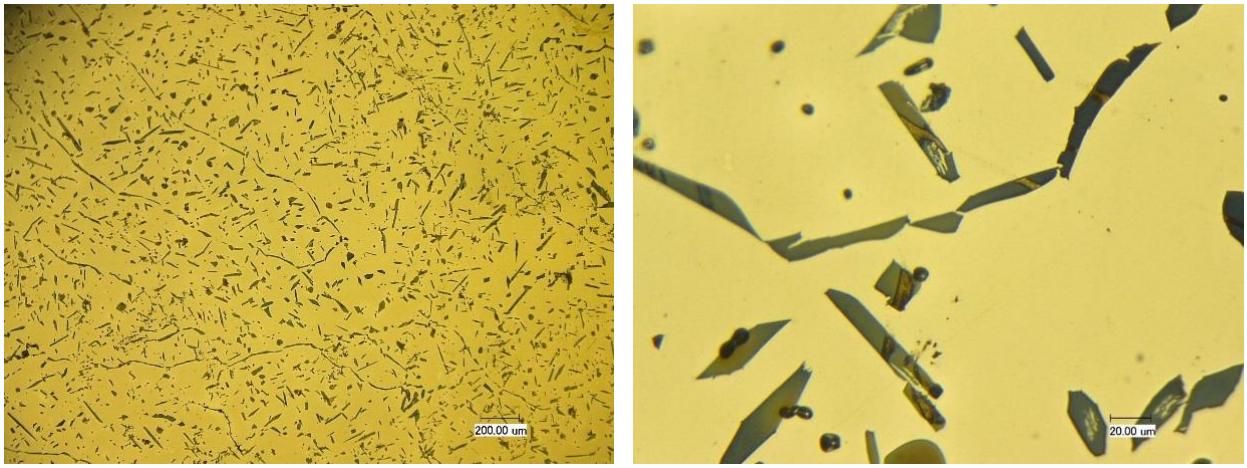

Figure 121- OM image of PGAA2 pre-treated at 1200°C for 50 hours, then heat treated at 1300°C for 1 hour in vacuum then water quenched.

Figure 122-a is the optical image of another ingot from this batch, and Figure 122-b is the OM image of a sample of the same ingot, cold rolled 80% reduction in thickness and then heat treated at 1150°C for 23 hours and then 1200°C for 1 hour, followed by water quenching, performed in order to homogenize the microstructure. As the image shows, two different regions appear on the sample: one has small precipitates forming on grain boundaries and within grains, and second with sizeable precipitates. Another attempt at homogenization was made on a new sample with a cold rolling of 80% reduction and heat treatments at 1080°C for 23 hours and 1150°C for 1 hour followed by water quenching. The OM images are shown in Figure 123 indicating the absence of the dendrites or a massive second phase, but precipitates with significant sizes.

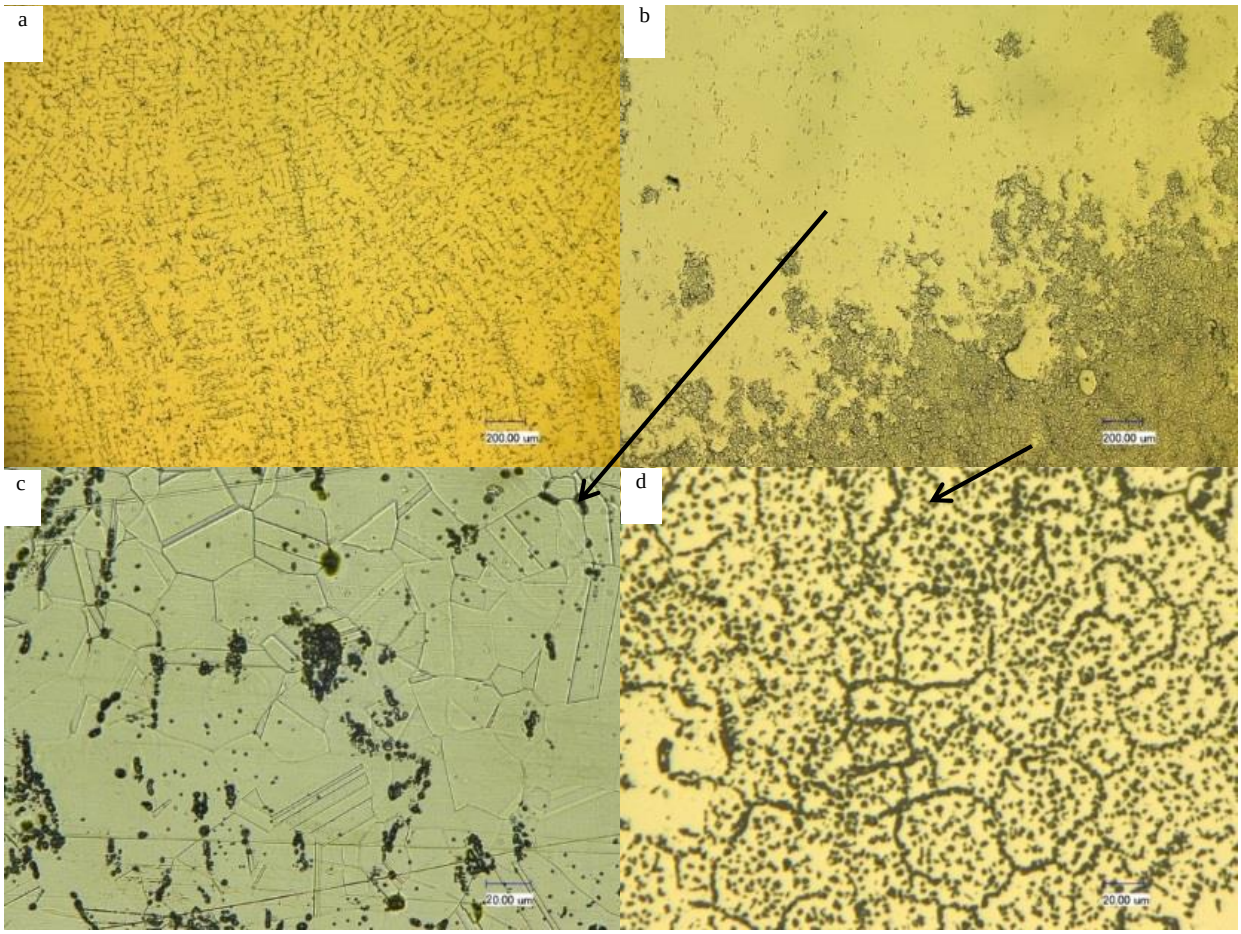

Figure 122- OM image of (a) as-cast sample of PGAA2 alloy, and (b)-(d) the sample cold rolled with 80% reduction, and then heat treated at 1150˚C for 23 hours and 1200˚C for 1 hour followed by water quenching.

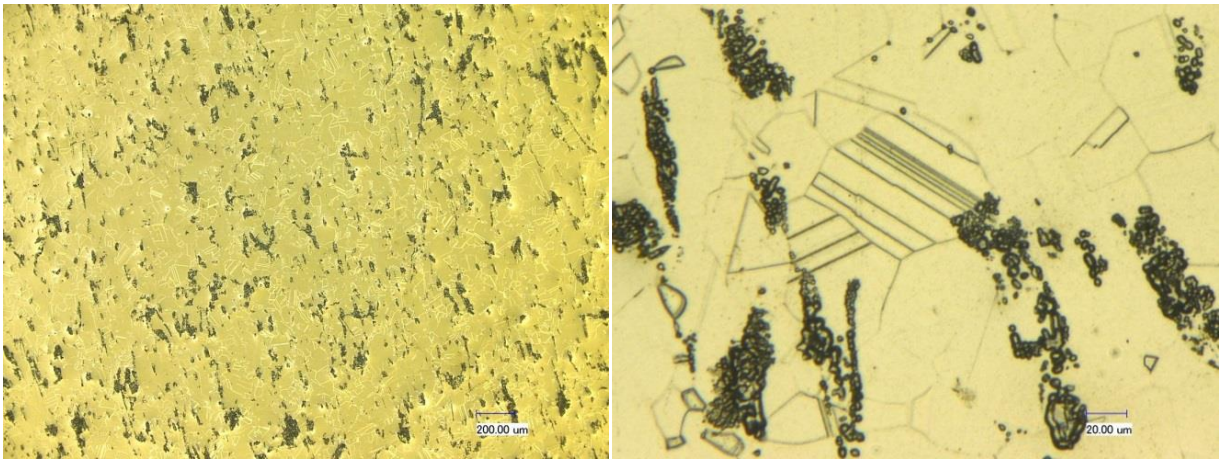

Figure 123- OM image of the PGAA2 sample cold rolled with 80% reduction, and then heat treated at 1080˚C for 23 hours and 1150˚C for 1 hour followed by water quenching.

This sample was then taken to SEM for further investigation and the images in Figure 124 show a recrystallized structure with particles. Figure 125-a shows a precipitate with higher magnification and with the EDS maps shown in Figure 125-b to g, two types of precipitates can be seen. The medium dark precipitates with round corners which are richer in Mn and Mo, and darker precipitates with sharper edges that contain Al (probably aluminum nitride).

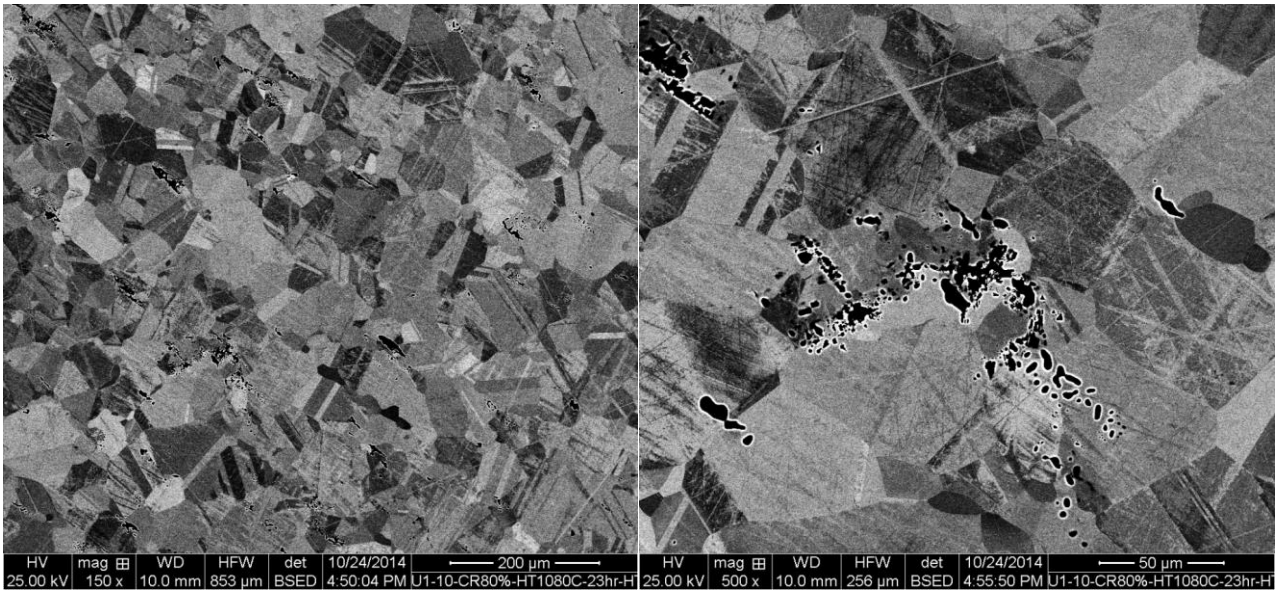

Figure 124- BSE image of the PGAA2 sample *cold rolled with 80% reduction, and then heat treated at 1080˚C for 23 hours and 1150˚C for 1 hour followed by water quenching*

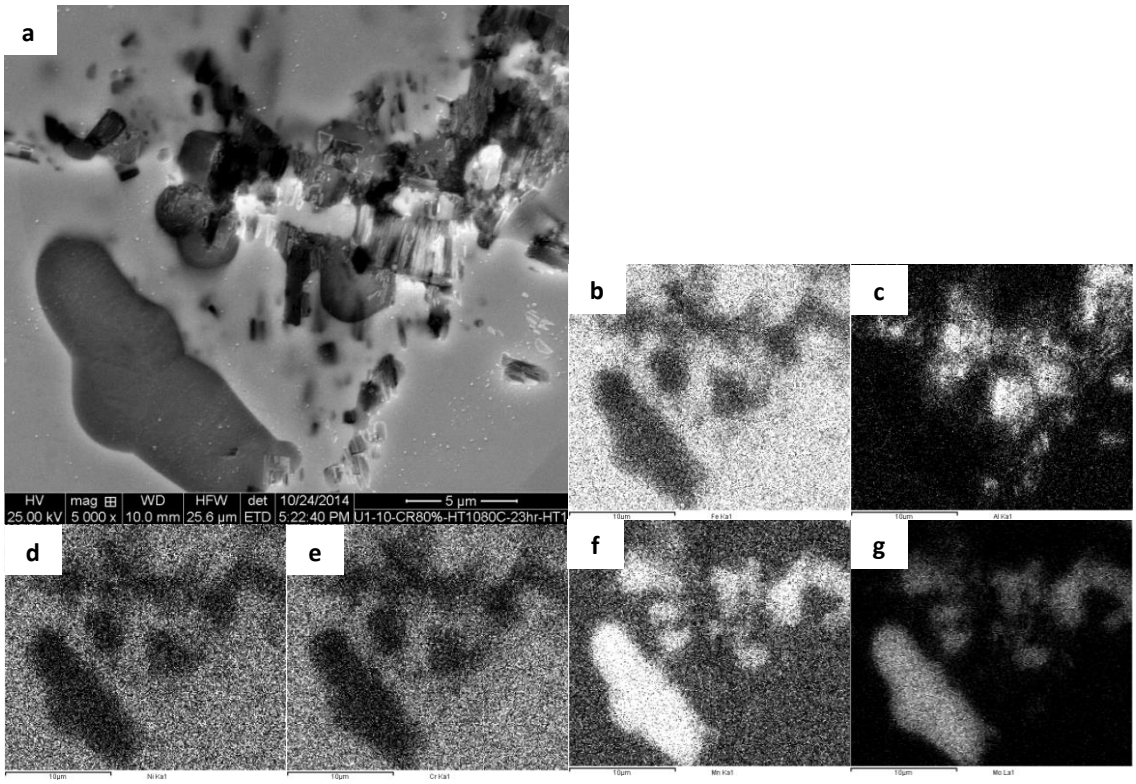

Figure 125- a) SEM image of the PGAA2 sample cold rolled with 80% reduction, and then heat treated at 1080˚C for 23 hours and 1150˚C for 1 hour followed by water quenching, EDS mappings of b)Fe, c)Al, d)Ni, e)Cr, f)Mn, g)Mo.

Another ingot from this batch was used for a heat treatment at 1200°C for 50 hours in a controlled atmosphere followed by water quenching. The OM images are shown in Figure 126 which shows no sign of a second phase, with significantly smaller precipitates, and rather large grain boundaries. Given that this microstructure is what is desired, further investigations regarding mechanical and oxidation properties of this alloy is currently undergoing.

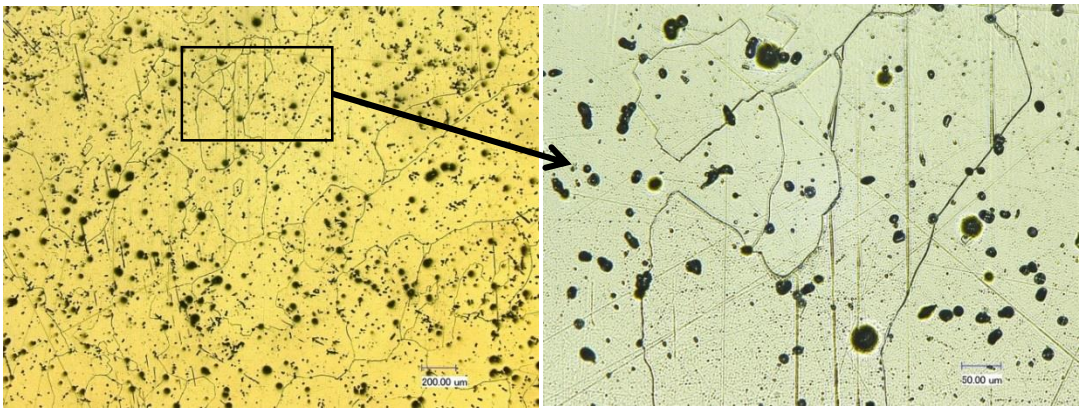

Figure 126- OM images of the PGAA2 alloy ingot heat treated at 1200˚C for 50 hours in controlled atmosphere followed by water quenching.

Next, samples were prepared from a bar of this alloy that was previously solutionized at 1200°C for 50 hours followed by water quenching, in a 10mm by 10mm by 1mm plates, and polished down to 0.25 micron. After cleaning the samples, they were placed inside a furnace with ambient air atmosphere (~50% humidity) at 800°C and removed after 12 hours and cooled down to room temperature. The samples were then cut in half using wire EDM and their cross sections were studied using Scanning Electron Microscopy (SEM) and Energy Dispersive Spectroscopy (EDS). Figure 127-a shows the Secondary Electron (SE) image of the cross section, and formation of a very thin, sub-micron oxide layer is observed. Figure 127-b to h show the EDS elemental maps of the same region of the cross section. Based on the maps, the outer-most scale is mostly made of Cr and O, hinting that this layer is mainly chromium oxide. Moreover, an Al-rich layer is formed right under the chromium oxide layer, with relatively smaller concentration of oxygen, pointing to internal oxidation of aluminum. Also, the EDS map of Mn shows that a significant part of the oxide layer is made of Mn, with a Mn-depleted zone right below the oxide layer. Based on these results, samples from the same bar were prepared in the same manner for a longer oxidation test at a higher temperature, in order to investigate whether higher temperature at longer times allows the aluminum to diffuse to surface and form a continuous alumina layer after the chromium oxide layer is disintegrated. Therefore, a 200 hour long oxidation test at 850°C was designed and carried out on disk-shaped samples with a diameter of ~5mm and ~1mm thick.

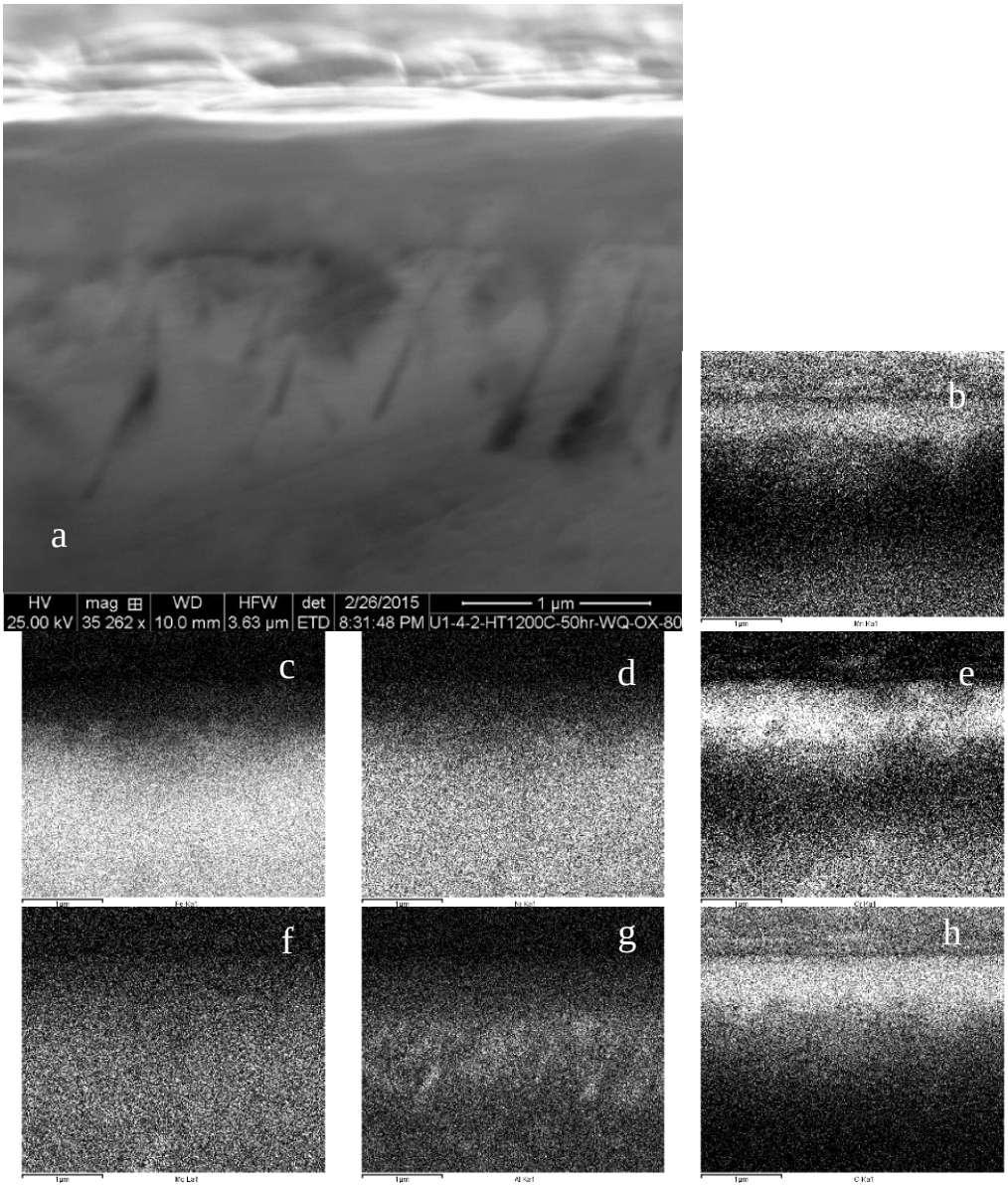

Figure 127- PGAA2 after oxidation at 800°C for 12 hours a) SE image, EDS maps of b) Mn, c)

Figure 128-a is the SE image of the cross section of the scale formed after 60 hours at 850°C, and Figure 128-b to f depicts the EDS elemental maps of this region. It can be observed that a very thin (~2 micron) and continuous layer of Mn+Cr oxide is formed on the surface, followed by a zone of rod-like Al-rich features in a matrix which is depleted from Mn and Cr. This second zone has a width of about 5 microns. Followed by this zone, is an Al-depleted layer, of ~2 microns. And finally, the base alloy as had been reported earlier. The peculiar shape of Al-rich rods suggests that these are aluminum nitrides, as had been previously reported in the base alloy. The proposed mechanism is that Al diffuses to surface but then reacts with the nitrogen and forms stable nitrides, which prevents the aluminum from forming an alumina surface scale.

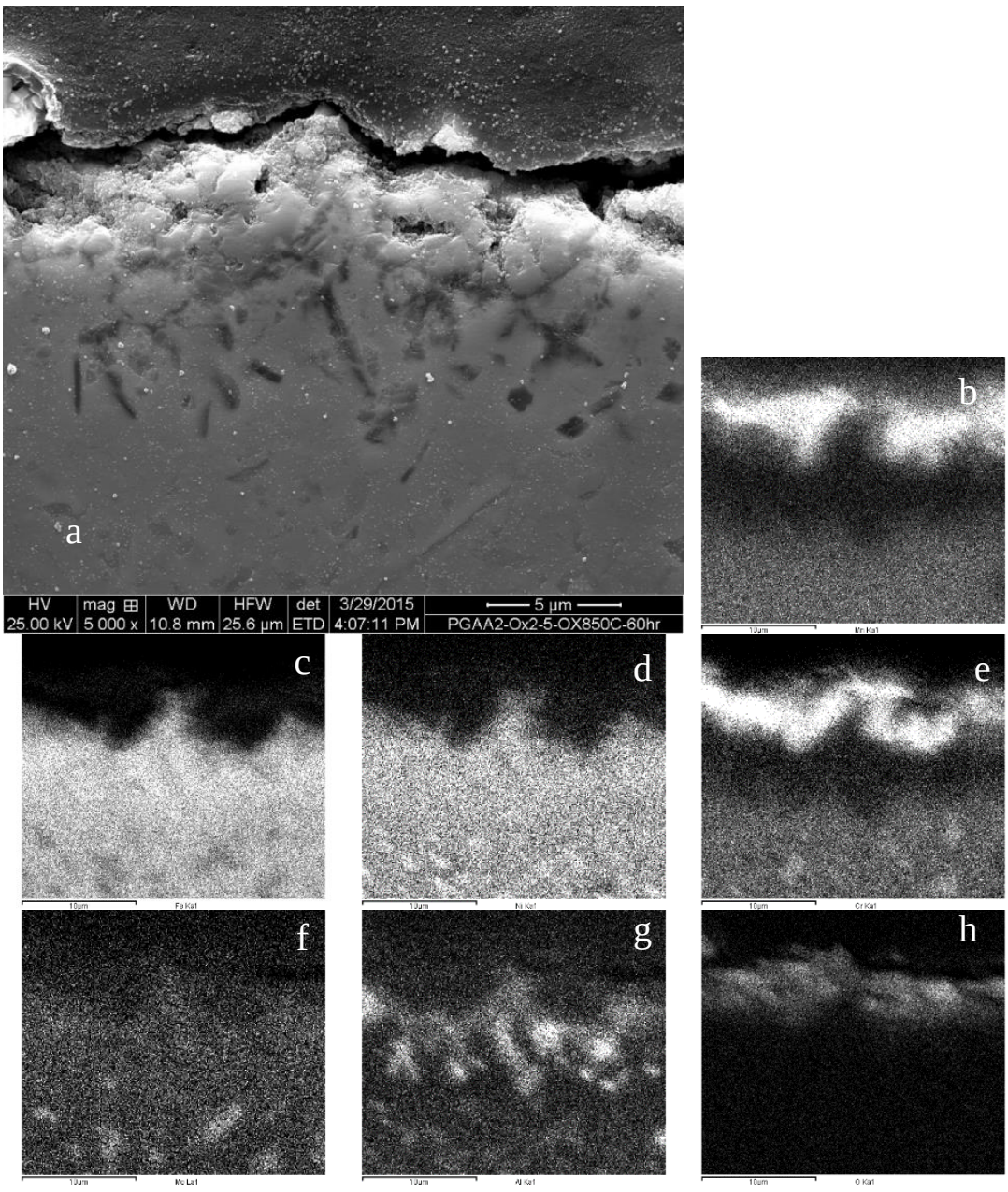

Figure 128- PGAA2 after oxidation at 850°C for 60 hours. a) SE image, EDS maps of b) Mn, c) Fe, d) Ni, e) Cr, f) Mo, g) Al, h) O

By continuing the oxidation test, at 108 hours, the cross section images, as shown in Figure 129, show that three layers described earlier still exist only with larger dimensions. The Mn+Cr oxide layer is now ~5 microns thick, and is detached from the surface, indicating its mechanical instability. After the crack, the Al-rich Mn/Cr-depleted layer, ~5 microns, exists, and then the Al-depleted layer of ~3-5 microns.

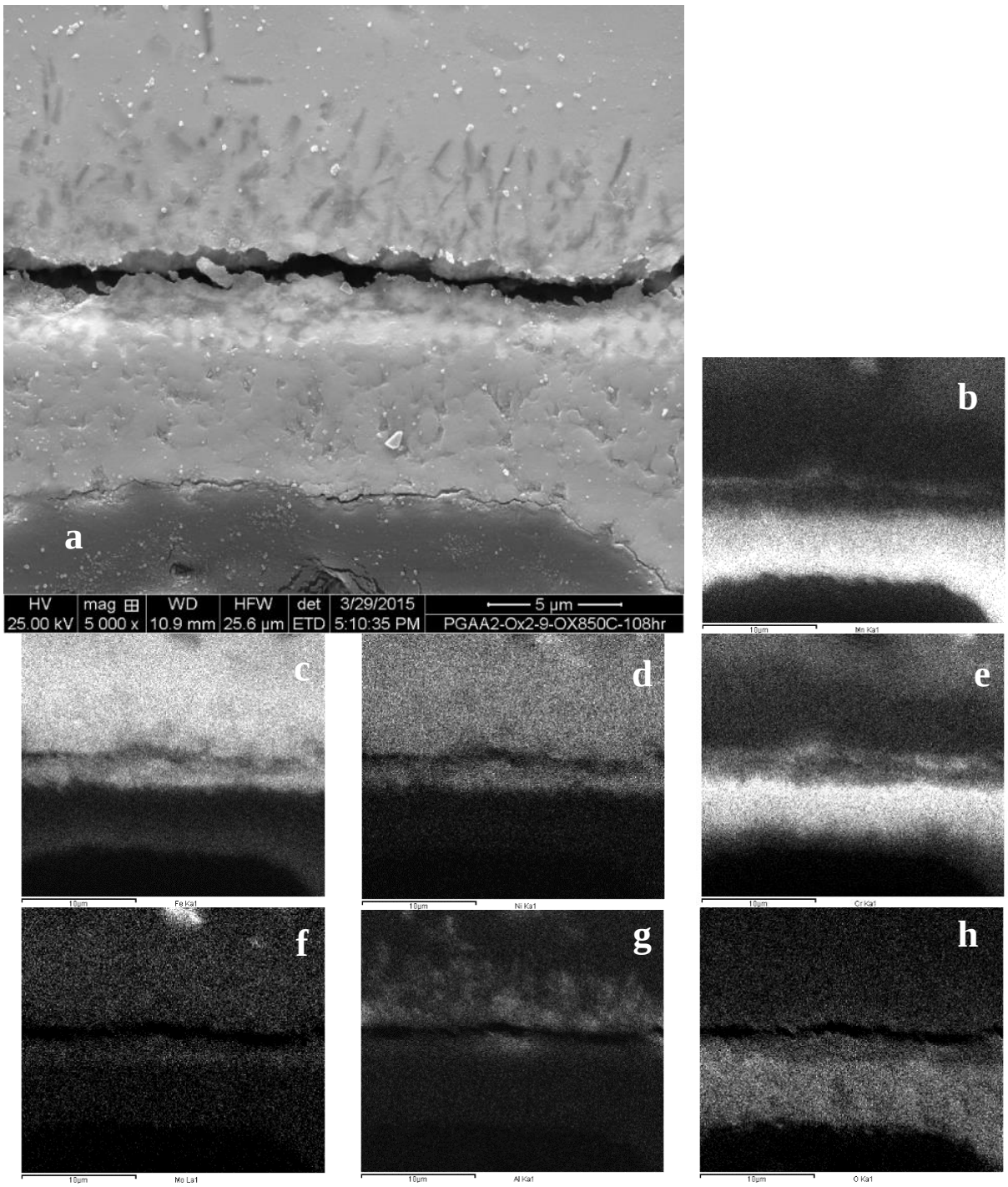

Figure 129- PGAA2 after oxidation at 850°C for 108 hours. a) SE image, EDS maps of b) Mn, c) Fe, d) Ni, e) Cr, f) Mo, g) Al, h) O

Continuing the oxidation test to 156 hours, the Mn+Cr oxide layer starts to spall off and form a discontinuous layer, as observed in Figure 130. The thickness of all the aforementioned layers have increased. Also, as the distance from the surface increases, the Al-rich features grow coarser,

with their growth orientation toward the surface, which suggests diffusion of Al toward the surface. Further oxidation up to 204 hours, Figure 7 shows a region where the Mn+Cr oxide scale has either remained or reformed, and the thickness has increased to ~10 microns. What is noticeable in this stage, beside the size of Al-rich features at a distance of ~30 microns from the surface, is formation of a very thin but continuous layer of the Al-rich phase right underneath the Mn+Cr oxide layer. This phenomenon is desirable when the outer-most layer is disintegrated after a few hundred hours. The results of these oxidation tests indicated the inability of this alloy to form an alumina scale satisfactorily. It must be noted that PGAA2 was designed by the model to form alumina at 800°C. Also the alloy received from the producer had significant deviations from the proposed alloy in terms of chemical composition and impurities. These facts have affected the alumina-forming ability of the alloy. As a result, a new batch of alloy has been ordered from another producer, with a higher requested chemical precision and purity. Next, samples from the new batch will be prepared as well as the current batch along with samples from Alloy1, and a set of oxidation tests will be carried out on these samples at different temperatures for 72 hours.

Finally, for a more detailed insight to the oxidation behavior formation of this alloy, samples were prepared out of: Alloy 1 (ORNL alumina-forming alloy) as the control sample, PGAA2 with additions of as impurity, and PGAA2. Samples were used for oxidation test at 700°C for 72 hours, following a solutionizing heat treatment at 1200°C for 50 hours. Figure 132 shows BSE image and EDS maps of Al and O of Al4, PGAA2 with and without N impurity, respectively, after oxidation test at 700°C for 72 hours, and formation of an Al-rich scale can be seen on each alloy. In Figure 133, the EDS linescans of the formed scale show the profile of oxygen and aluminum versus distance. Based on these figures, and since alumina-formation has already been confirmed and published by ORNL for Al4, and by observing the elemental profiles for Al4 and PGAA2 versus PGAA2+N (which we know forms an Al-N rich scale), it can be concluded that PGAA2 without N impurity can form alumina scale.

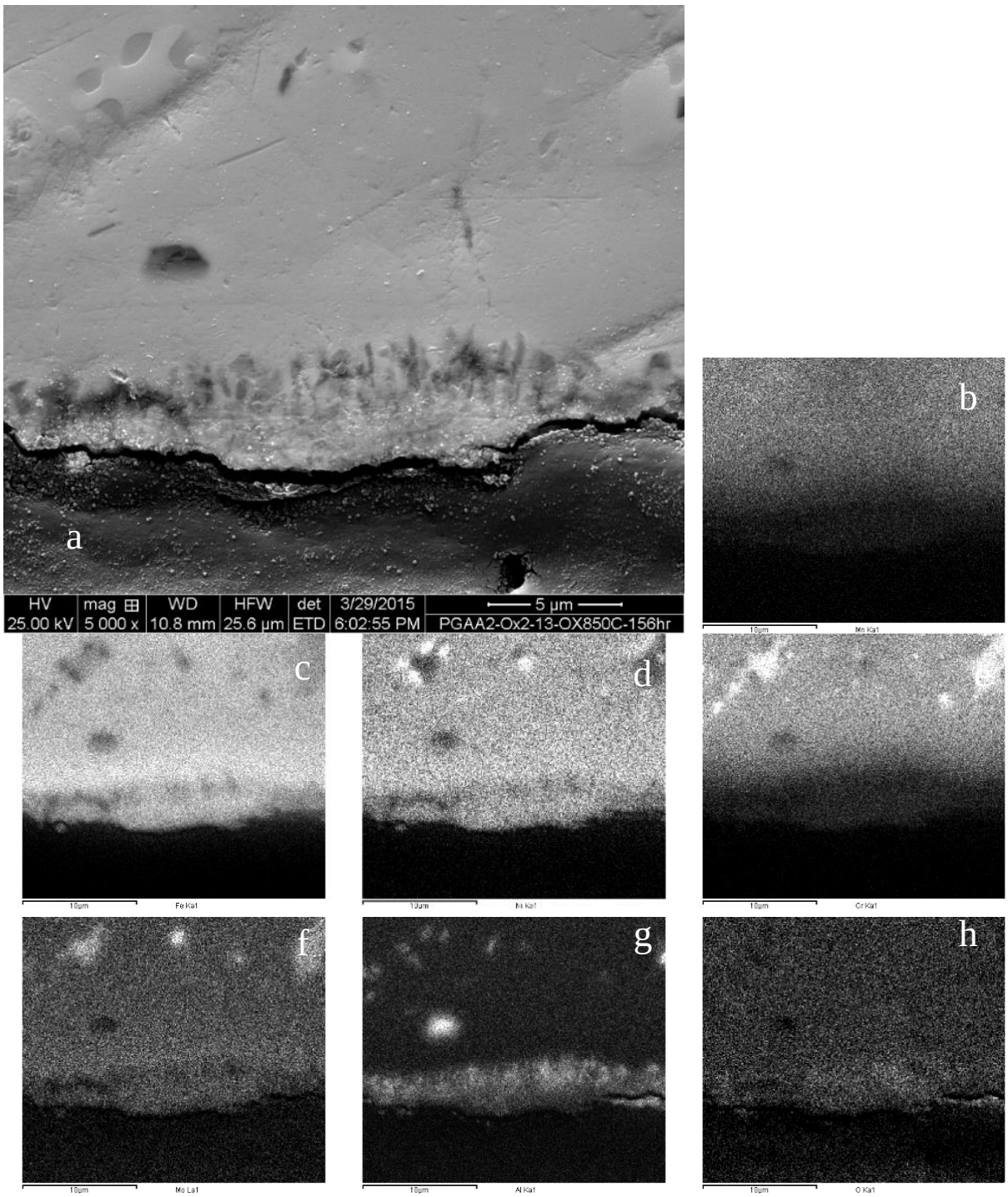

Figure 130- PGAA2 after oxidation at 850°C for 156 hours. a) SE image, EDS maps of b) Mn, c) Fe, d) Ni, e) Cr, f) Mo, g) Al, h) O

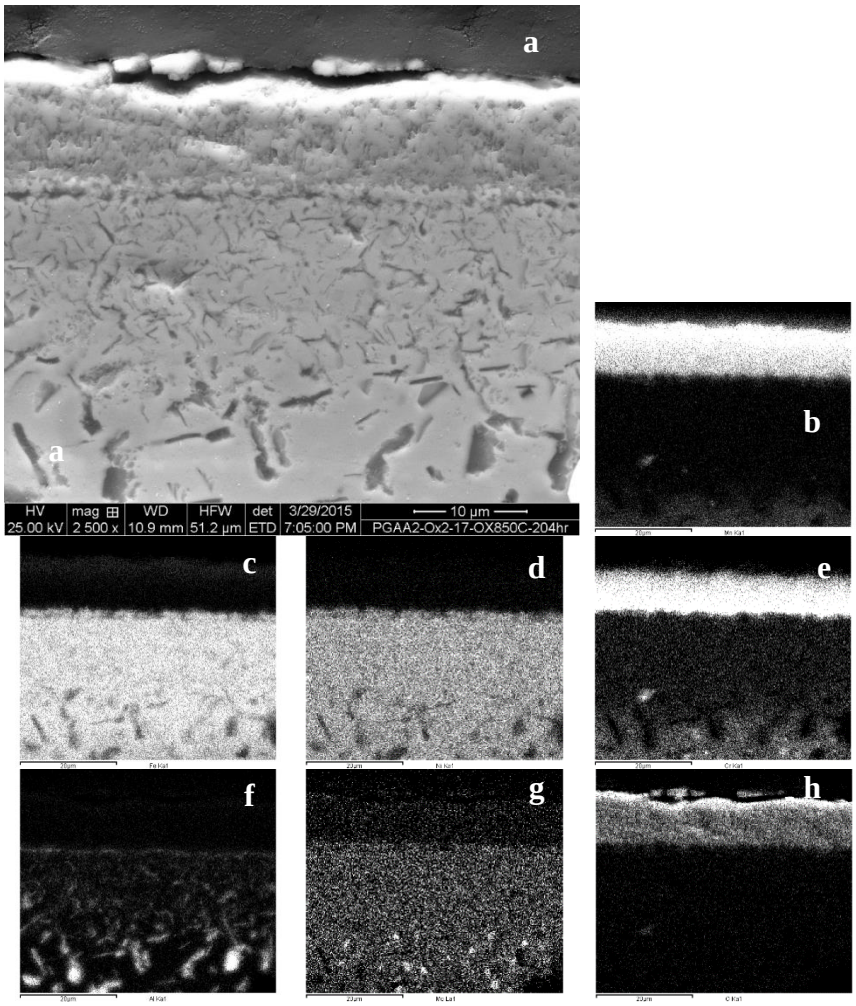

Figure 131- PGAA2 after oxidation at 850°C for 204 hours. a) SE image, EDS maps of b) Mn, c) Fe, d) Ni, e) Cr, f) Mo, g) Al, h) O

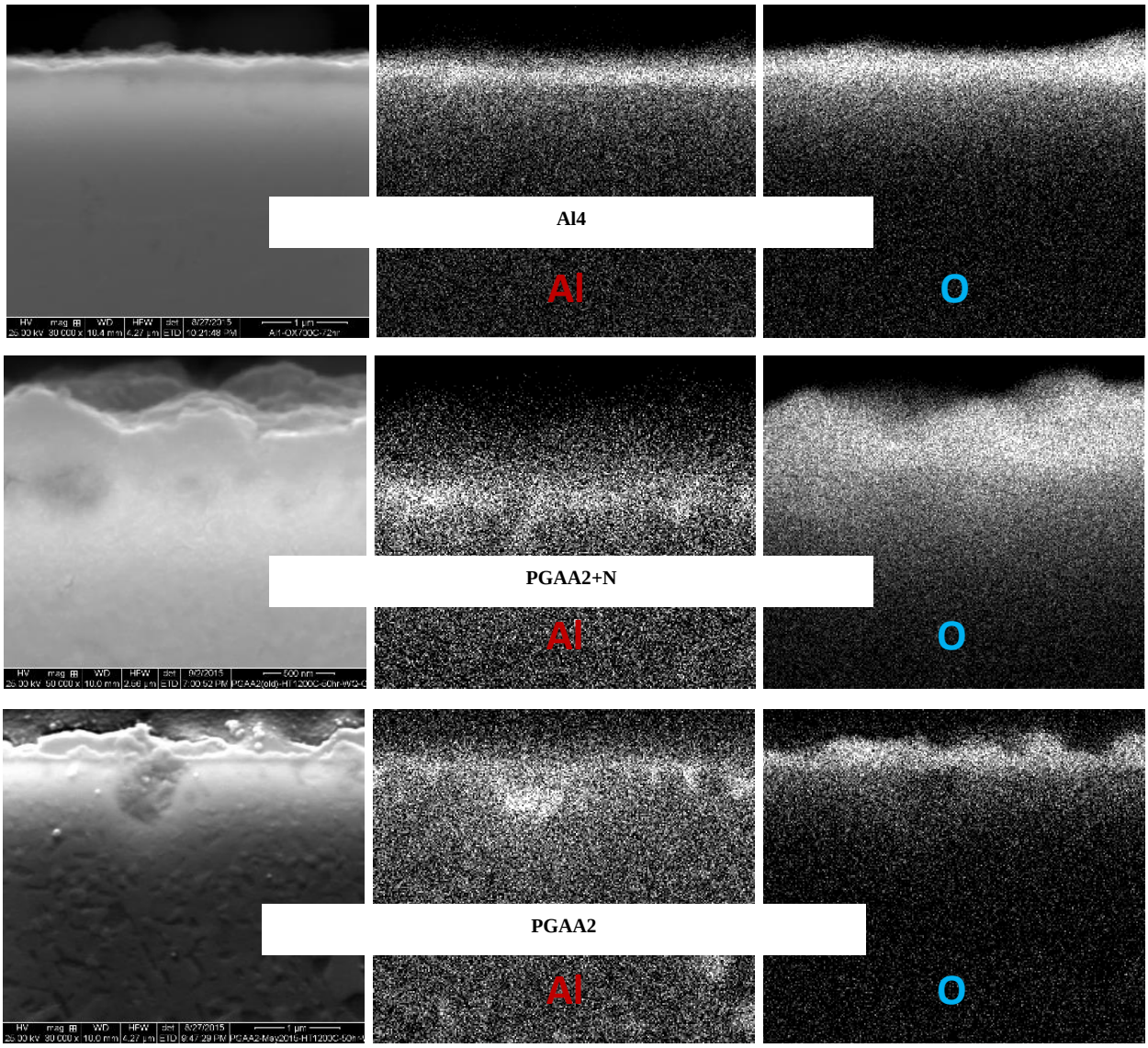

Figure 132- BSE image and EDS maps of Al and O of Al4, PGAA2 with and without N impurity, respectively, after oxidation test at 700°C for 72 hours

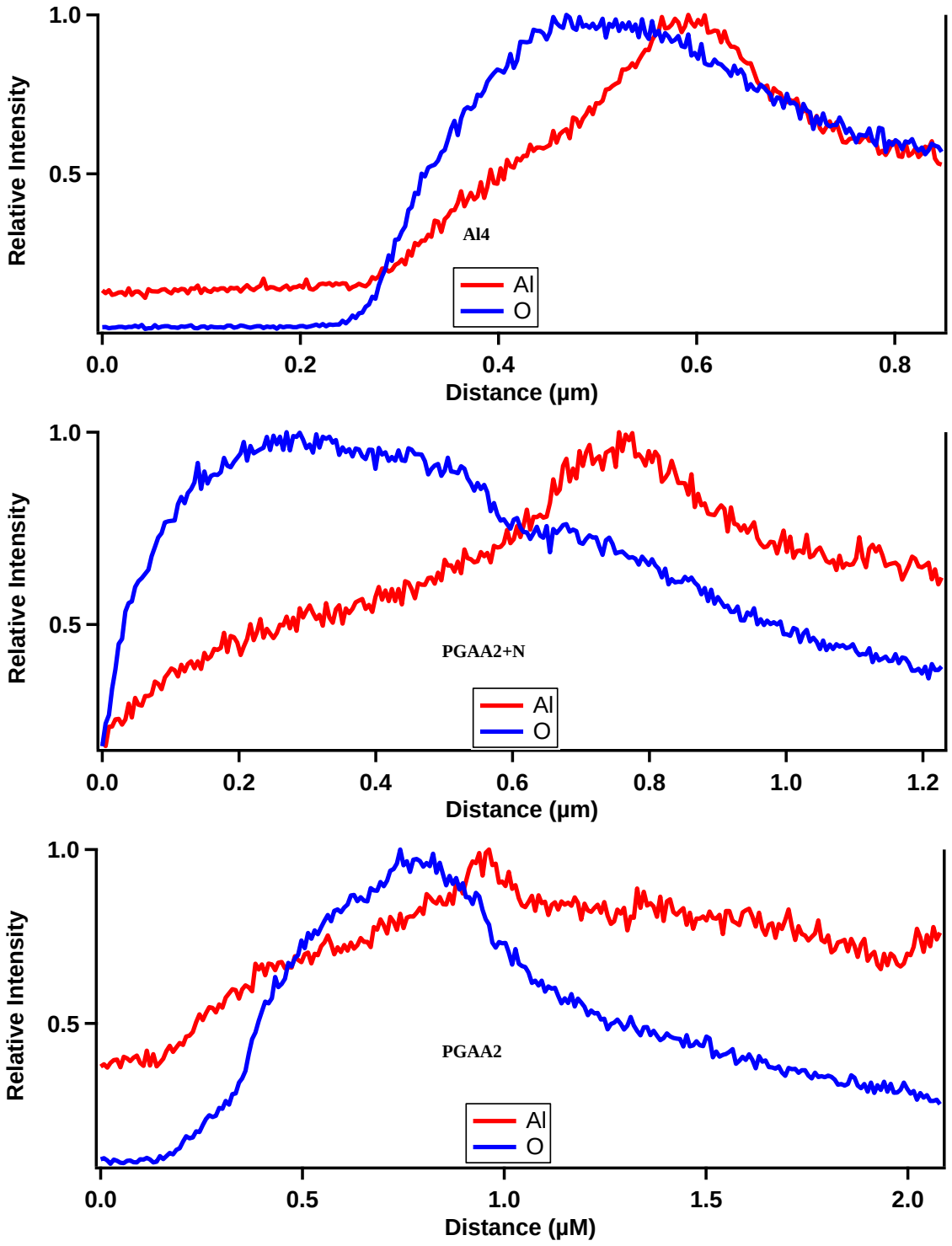

Figure 133- EDS linescans of Al4 and PGAA2 with and without N impurity, respectively

e) Alloy 4

Figure 134 shows the OM image of this alloy which demonstrates the existence of two different phases, and further WDS investigations (Figure 134) show that dark precipitates with sharp edges is rich in Al. Region 1 is richer in Al, Mo, and Cr, than region 2, but has less Ni, and therefore, could possibly be a different phase. Another precipitate exists in the image (region 3), which is bright and very small. This precipitate is richer in Mo and Cr, but less Ni. Region 4, which is precipitate with sharp edges, is rich in Al (alumina nitride maybe). Figure 135 shows EDS mapping of the sample, and that the two existing phases differ significantly in chemical composition.

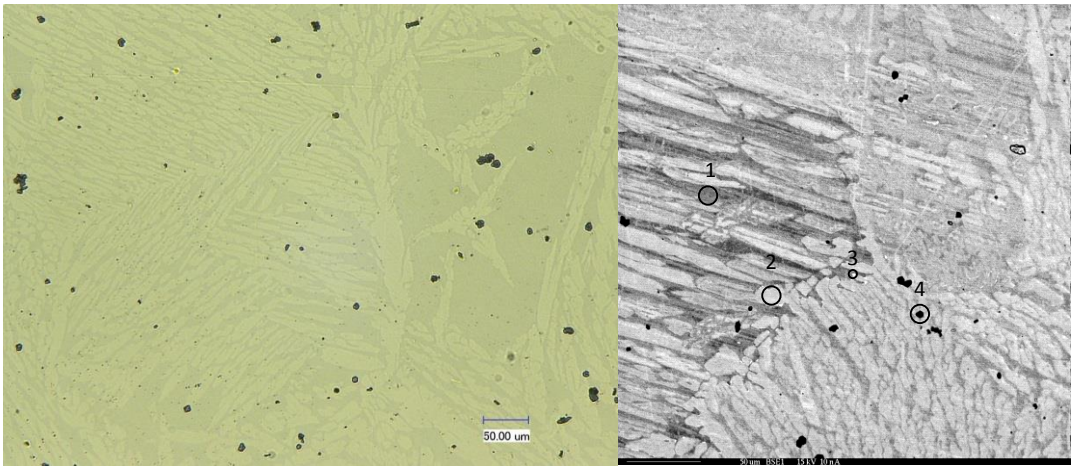

Figure 134- (left) OM image of the as-cast Alloy 4. (right) BSE image of the same sample, showing regions that have been studied with EDS.

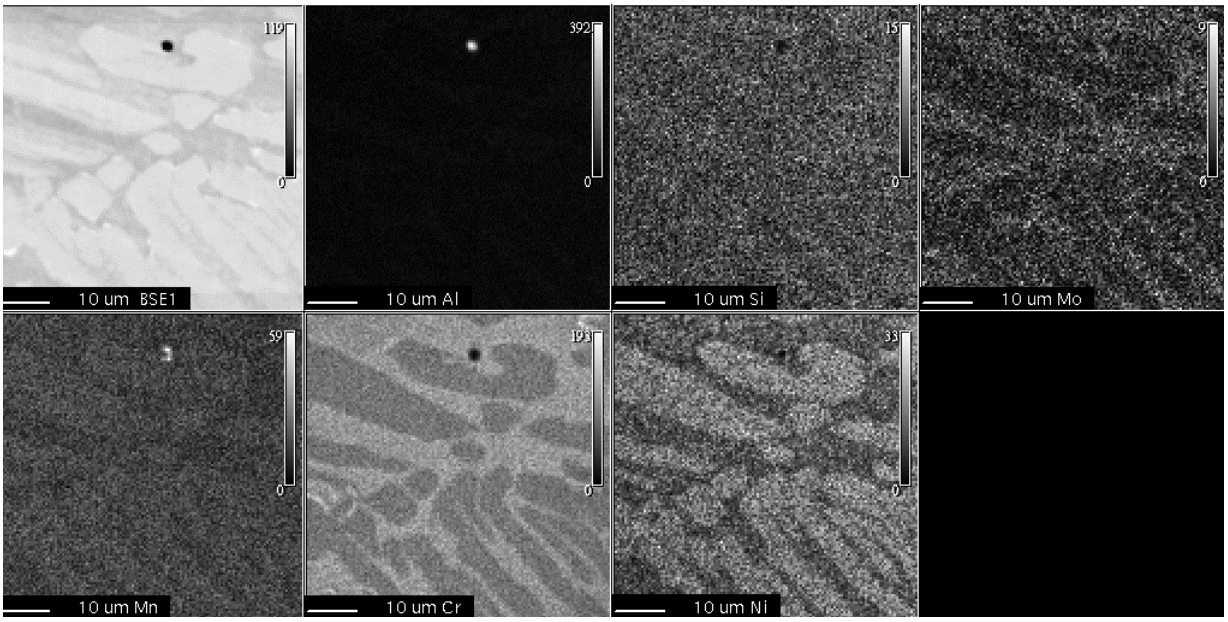

Figure 135- EDS mapping of as-cast Alloy 4.

This alloy was already shown to have a two-phase structure that will persist even after at heat treatment at 1200°C for 1 hour, as it can be predicted from the theoretical phase diagram (Figure

136). The heat treated bar was also subjected to ECAP at 950°C and 0.5 in/sec, the result of which was a failure, but to a significantly less extent as compared to the other two proposed alloys. As a result, despite the fact that neither the theoretical phase diagram nor the alumina-formation calculations indicate this alloy as a promising candidate, the samples were prepared from the severely deformed bar to be studied for microstructure. The proposed course of treatment is the heat treatment around 970°C, because based on the theoretical phase fraction calculations (Figure 137), this temperature has the highest weight fraction of austenite.

Figure 138 shows the microstructure of this alloy after ECAE. As expected, the microstructure consists of two major phases and precipitates that were visible before the extrusion, and another heavily deformed phase with sharp edges. By increasing the extent of etching, (sub)grain boundaries of the major main phase (austenite) grains, with a grain size of around 10μm can be seen. Figure 139 depicts the optical image of the extruded bar after the proposed heat treatment at 970°C for 30 minutes. These images show that the two major phases still persist, while the formerly deformed phase with sharp corners now has a dendritic structure with rounded edges and appears to be the same as the minor main phase (ferrite). Moreover, the big islands of the minor main phase have formed fine precipitates along their grain boundaries.

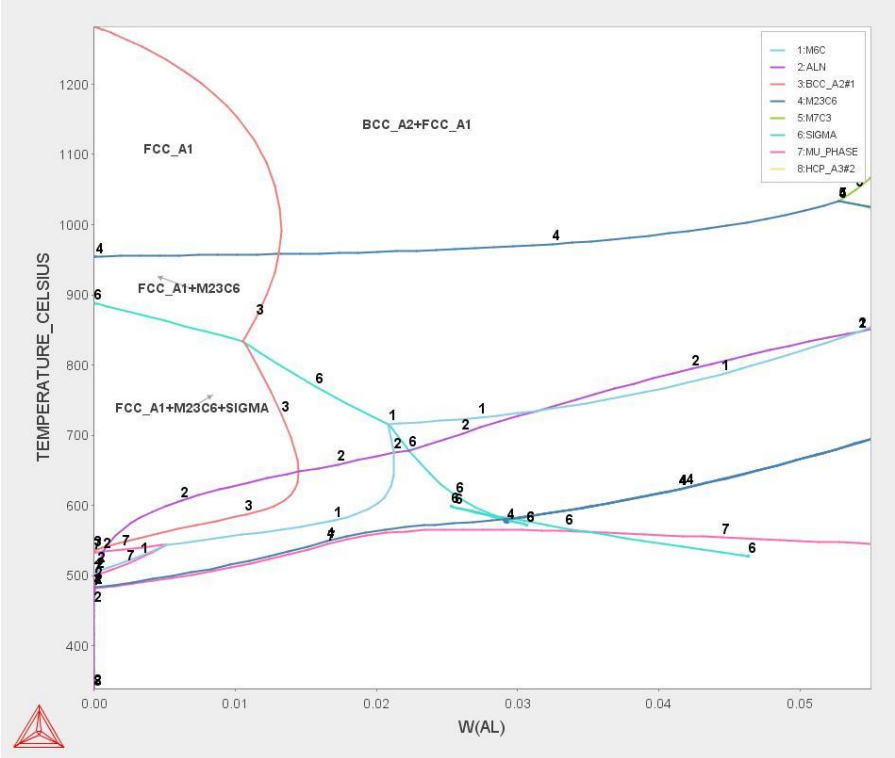

Figure 136- Theoretical phase diagram of Alloy 4, temperature vs. weight fraction of Al

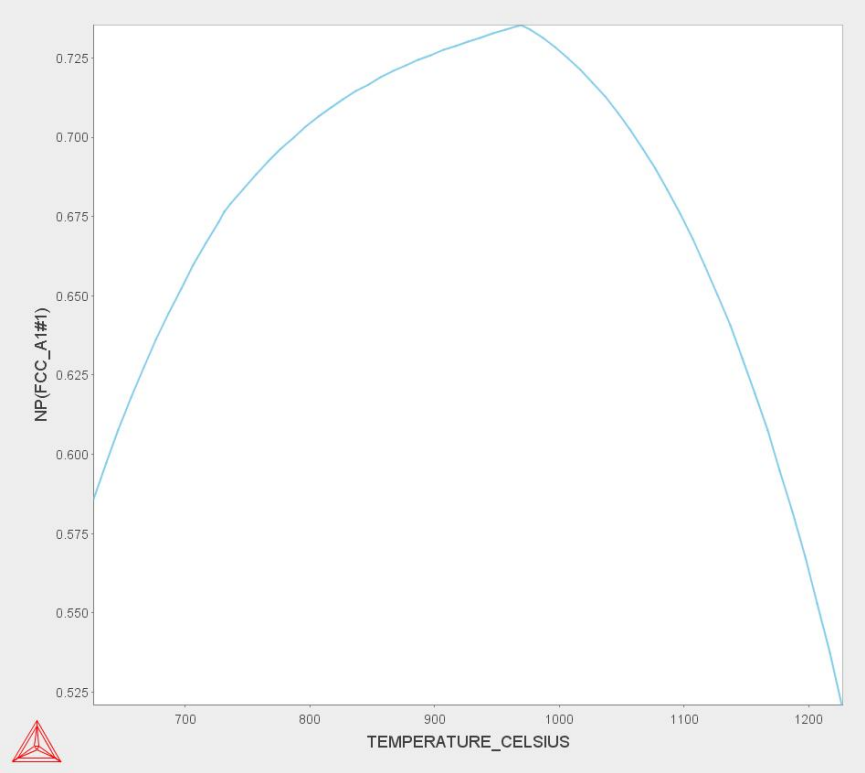

Figure 137- Theoretical phase fraction calculations showing weight fraction of fcc austenite vs. temperature for Alloy 4.

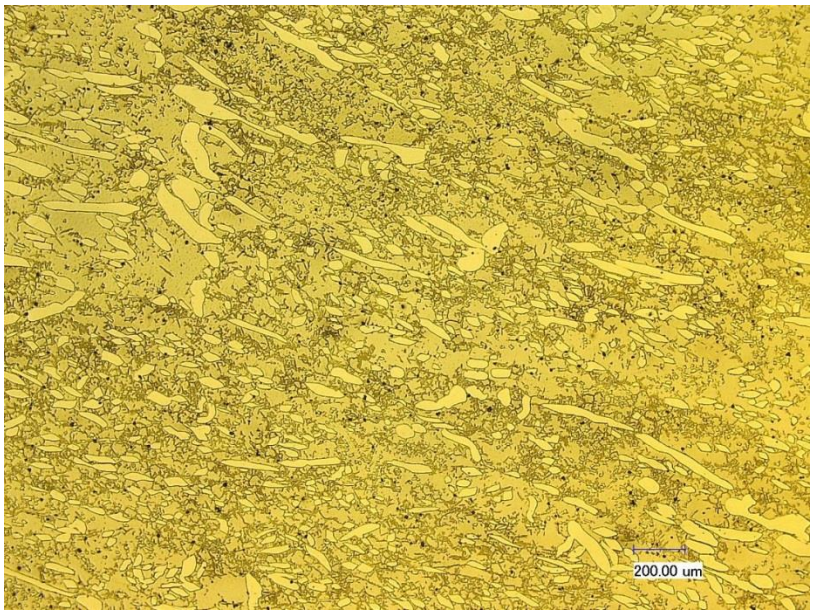

Figure 138- OM of Alloy 4 after ECAE at 900°C with 0.5 inch/sec rate

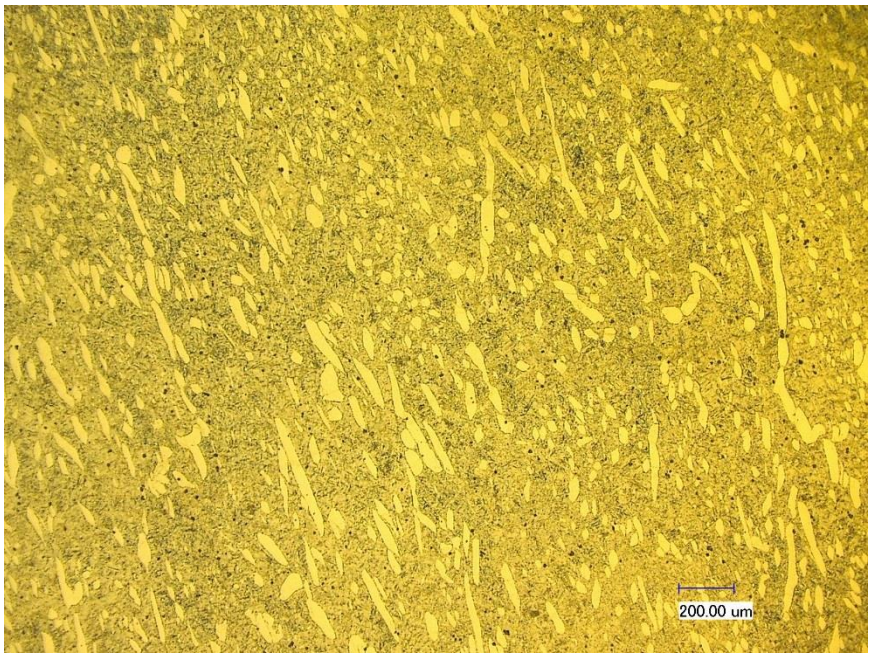

Figure 139- OM of Alloy 4, extruded at 900°C with 0.5 inch/sec rate, heat treated at 970°C for 30 minutes and water quenched

In an attempt to solutionize this alloy, an ingot was heat treated at 1200˚C for 50 hours under controlled atmosphere, then water quenched. Figure 15 shows the OM image of the heat treated sample. The two phase structure, as it can be seen, still persists, but the sizes of the precipitates have decreased. Attempt to solutionize this alloy is continuing. These results, indicating the inability to achieve a fully austenitic structure, proves this alloy a poor candidate for the proposed designed criteria, and investigations on this alloy was stopped.

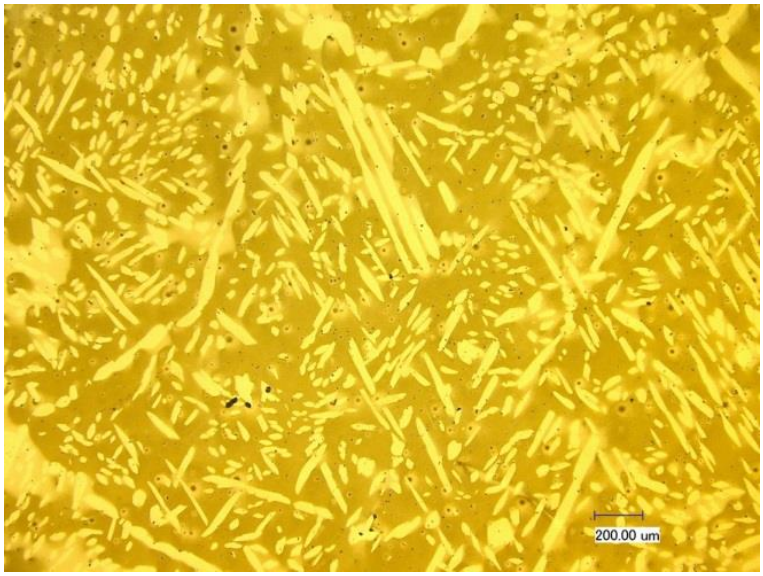

Figure 140- OM image of Alloy 4 samples after heat treatment at 1200˚C for 50 hours under controlled atmosphere, then water quenched

Conclusions:

The results of study on the mechanical response of the alloys can be used to conclude the following points:

1. The twin density increases with the increasing amount of strain.
2. The twin width is still at nano-scale despite different strain levels.
3. From in-situ and in-furnace heat treatments, it can be said that deformation twins are stable up to 900˚C, under zero stress, for one hour.
4. Observed thermal stability of these nano-twins constitutes a promising strategy for strengthening stainless steels at elevated temperatures.
5. Thermally stable nano twins may also act as resourceful nucleation points for precipitates that form at higher temperatures and contribute to high-temperature mechanical strength of the material.

The results of the computational study are as follows:

1. A robust model for prediction of alumina formation in stainless steels was constructed based off of two criteria – effective valence method and third element effect. This model can efficiently separate alumina forming vs. non-alumina forming steels.

2. A machine learning based informatics approach was developed to build a model for prediction of deformation mechanisms (based on Stacking Fault energy regimes) in stainless steels for unknown compositions.

3. A genetic algorithm optimization framework was used to come up with new alloy compositions which would satisfy the design criteria established for new generation of stainless steels for high temperature power plant applications.

The above framework can be successfully implemented for accelerated materials discovery, here in the context of alloy design to significantly reduce the resources spent in experimental exploration for a similar alloy design task.